博士学位论文

曲面的几何、拓扑与组合结构研究

ON THE GEOMETRIC, TOPOLOGICAL AND COMBINATORIAL STRUCTURES OF SURFACES

研　　究　　生：曲庆睿

指　导　教　师：朱一飞助理教授

南方科技大学

二〇二六年五月

国内图书分类号：O189　　学校代码：14325
国际图书分类号：515.1　　密级：公开

理学博士学位论文

曲面的几何、拓扑与组合结构研究

学 位 申 请 人：曲庆睿
指 导 教 师：朱一飞助理教授
学 科 名 称：数学
答 辩 日 期：2026 年 5 月
培 养 单 位：数学系
学位授予单位：南方科技大学

ON THE GEOMETRIC, TOPOLOGICAL AND COMBINATORIAL STRUCTURES OF SURFACES

A dissertation submitted to
Southern University of Science and Technology
in partial fulfillment of the requirement
for the degree of
Doctor of Science
in
Mathematicas

by
Qu Qingrui

Supervisor: Assistant Prof. Zhu Yifei

May, 2026

摘 要

本文系统性地从几何、拓扑和组合的角度研究了一类由多面体乘积构造的实矩角复形曲面及其对偶曲面。对偶曲面的边集自然形成一组最短的闭测地线，为研究曲面上的闭测地线系统、同调群与双曲结构之间的关系提供了理想模型。此外，这些曲面具有高度对称性。基于这些思想与方法，我们可以自然地将研究拓展到正则地图理论，从而得到更多具体的对称曲面族。

我们首先考察了该系统中基本群与一维同调群之间的映射性质。通过将 Hurewicz 映射限制在由闭测地线生成的自由 Abel 群上，我们给出了该映射核的一组标准基，并证明了该基中的每个向量与圈图 C_n 的非空独立集一一对应。利用组合计数方法，我们确定了核与像的秩，得到了用 Lucas 数 $L(n)$ 表达的显式公式。这一结果揭示了曲面几何与图论之间的联系。

随后，我们研究了超立方体图 Q_n 正则嵌入的同调性质。通过由图的边构成的闭测地线系统，我们计算了当偶数 $n \leq 18$ 时 Hurewicz 映射的核维数与像的秩，并基于观察到的数值规律提出了核维数的闭式猜想。

从双曲几何的角度，我们为曲面赋予标准双曲度量，并计算了 $5 \leq n \leq 12$ 时最短测地线长度函数在 Teichmüller 空间的 Morse 指标。该指标通过其梯度向量张成的空间的维数计算得出。我们部分验证了所猜想的指标公式，将曲面的几何与其组合结构联系起来。

在论文的最后部分，我们研究具有平坦度量的代数曲面与直纹面，分析了直纹面上的直线与圆锥曲线的性质，特别关注在非 Hermit 量子力学中临界曲面的几何结构。

关键词：多面体乘积; 实矩角复形; 闭测地线; Lucas 数; 正则嵌入; 双曲几何; Morse 指标; Teichmüller 空间; 直纹面

ABSTRACT

In this thesis, we systematically investigate, from geometric, topological, and combinatorial perspectives, a class of real moment-angle complex surfaces constructed via polyhedral products, together with their dual surfaces. The edge set of the dual surface naturally forms a collection of shortest closed geodesics, providing an ideal model for studying the relationship among closed geodesic systems, homology groups and hyperbolic structures on surfaces. These surfaces exhibit a large amount of symmetry. Building on these ideas and methods, we can naturally extend the investigation to the theory of regular maps, which provides more explicit families of symmetric surfaces.

We first examine the mapping properties of this system between the fundamental group and the first homology group. By restricting the Hurewicz map to the free abelian group generated by the closed geodesics, we provide a standard basis for the kernel of this map and prove that each vector in this basis corresponds bijectively to a nonempty independent set of the cycle graph C_n. Using combinatorial enumeration methods, we determine the ranks of the kernel and the image, obtaining explicit formulas expressed in terms of the Lucas numbers $L(n)$. This result reveals a connection between surface geometry and graph theory.

We then investigate the homological properties of regular embeddings of hypercube graphs Q_n. Through the system of closed geodesics formed by the edges of the graph, we compute the kernel dimensions and image ranks of the Hurewicz map for even $n \leq 18$, and based on the observed numerical patterns, we propose a closed-form conjecture for the kernel dimension.

From the perspective of hyperbolic geometry, we endow the surface with the standard hyperbolic metric and compute the Morse index of the systole function on Teichmüller space for $5 \leq n \leq 12$. This index is computed via the dimension of the space spanned by its gradient vectors. We obtain partial verification of the conjectured index formula, linking the geometry of the surface to its combinatorial structure.

In the final part of the thesis, we turn to the study of algebraic surfaces and ruled surfaces equipped with flat metrics. We analyze the properties of lines and conics on ruled surfaces, with particular attention to geometric structures arising as critical surfaces in non-Hermitian quantum mechanics.

Keywords: polyhedral products; real moment-angle complexes; closed geodesics; Lucas numbers; regular embeddings; hyperbolic geometry; Morse index; Teichmüller space; ruled surfaces

TABLE OF CONTENTS

CHAPTER 1 INTRODUCTION

1.1 Research Background

A Riemann surface is a remarkably rich object that reveals different facets of mathematics depending on the perspective from which it is viewed. From the standpoint of geometry, a compact Riemann surface of genus at least two carries a canonical hyperbolic structure by the Uniformization Theorem. In this way, it appears as a closed hyperbolic manifold whose geometry is governed by Fuchsian groups, with its moduli controlled by Teichmüller space and mapping class groups. Hyperbolic geometry thus provides a natural language for understanding its global structure, deformations, and symmetries.

From a topological and combinatorial perspective, the same surface may be regarded simply as a smooth two-dimensional real manifold. Graph embeddings on the surface decompose it into vertices, edges, and faces, often producing highly symmetric tessellations. These embedded graphs encode the surface's combinatorial structure and link it to permutation representations and group actions. In particular, regular and highly symmetric maps highlight deep connections between graph theory, combinatorics, and group theory, allowing geometric symmetry to be studied through algebraic data.

Finally, a Riemann surface can be viewed as a complex algebraic curve defined over $\mathbb{C}$. In this algebro-geometric incarnation, it becomes an object of algebraic geometry and arithmetic: its function field, divisors, and morphisms connect to the theory of algebraic curves, while additional arithmetic structure relates it to number theory. These three viewpoints: hyperbolic-geometric, combinatorial-topological, and algebraic-arithmetic are not separate descriptions but complementary lenses through which the same profound object can be understood.

1.2 Statement of Main Results

First, we study the geometry and topology of a class of real moment-angle complexes $X = Z(C_n, (D^1, S^0))$ given by polyhedral products, which is a surface, and its dual surface $Z(C_n, (D^1, S^0))^*$. The edges of the dual surface exactly form a set of shortest closed geodesics, and we investigate the homological properties of this set.

Consider the Hurewicz map of the real moment-angle complex

$$h : \pi_k(X) \to H_k(X).$$

Let S denote the systoles (the set of shortest non-contractible closed geodesics) of X. There exists a natural inclusion $\iota : S \hookrightarrow \mathrm{Conj}(\pi_1(X))$, which maps each systole to its corresponding conjugacy class. Composing ι with the Hurewicz homomorphism $h : \mathrm{Conj}(\pi_1(X)) \to H_1(X)$ yields a morphism embedding the systoles set into the first homology group. Since $H_1(X)$ being abelian, this morphism extends uniquely to a homomorphism from the free abelian group $\tilde{S} := \mathbb{Z}^S$ generated by S. This relationship is captured in the following commutative diagram:

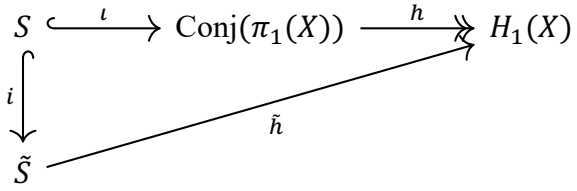

Theorem 1.1: A standard basis for the kernel of the map $\tilde{h}$ can be given, where each vector in this basis corresponds to an element of the set of nonempty independent sets of the cycle graph C_n.

Since the number of independent sets of a cycle graph can be obtained by standard combinatorial methods, we know this number is $L(n)$, i.e., the Lucas numbers, which follow the same recurrence $L(n) = L(n-1) + L(n-2)$ as the Fibonacci type numbers but with initial conditions $L(1) = 1$, $L(2) = 3$. Thus we can immediately determine the dimension of this space; similarly, we can determine the dimension of the subspace spanned by the image of this map in the homology group.

Corollary 1.1: By the enumeration formula, we can determine the ranks of the free abelian groups:

$$\text{rank } \mathrm{Ker}\, \tilde{h} = L(n) - 1,$$

$$\text{rank } \mathrm{Im}\, \tilde{h} = n \cdot 2^{n-3} - L(n) + 1.$$

Using techniques of polyhedral decomposition, Al-Raisi studied the action of the cyclic group $\mathbb{Z}/n$ on the cohomology groups of surfaces and obtained the following identity.

Theorem 1.2: [65]Proposition 3.5.10 For $n \geq 4$, we have

$$\frac{1}{n}\left(\sum_{d|n}\mu(d)2^{\frac{n}{d}}\right)-(n-1)+\sum_{\substack{d|n\\1<d<n}}\left(\frac{1}{d}\sum_{d_1|d}\mu(d_1)2^{\frac{d}{d_1}}\right)=\frac{1}{n}\left(\sum_{d|n}\varphi(d)2^{\frac{n}{d}}\right)-(n+1),$$

which relates the Möbius function and the Euler totient function by equating two different methods of orbit counting.

In a similar spirit, by counting orbits of a set under the action of a cyclic group in two different ways, we obtain another identity involving the Möbius function and the Euler totient function.

Theorem 1.3: For $n \geq 4$, we have

$$\frac{1}{n}\left(\sum_{d|n}\mu(d)L\left(\frac{n}{d}\right)\right)+\sum_{\substack{d|n\\1<d<n}}\left(\frac{1}{d}\sum_{d_1|d}\mu(d_1)L\left(\frac{d}{d_1}\right)\right)=\frac{1}{n}\left(\sum_{d|n}\phi(d)L\left(\frac{n}{d}\right)\right)-1$$

relating the Möbius inversion function, the Euler totient function and the Lucas numbers by equating the two different orbit counting methods of the systoles.

We next investigate the embedding properties of this surface, considering both higher-dimensional sphere and the three-dimensional Euclidean spaces.

Theorem 1.4: One can embed $X^* = Z(C_n, (D^1, S^0))^*$ into the $(n-1)$-dimensional sphere $S^{n-1} \subset \mathbb{R}^n$ with the standard round metric, such that every edge is a geodesic arc, and also require that all edges have the same length $\arccos\left(\frac{n-3}{n-2}\right)$.

Theorem 1.5: For $n \geq 5$, the surface $Z(C_n, (D^1, S^0))^*$ can be smoothly embedded into the 3-dimensional Euclidean space $\mathbb{R}^3$. The isometry group of this embedded surface in $\mathbb{R}^3$ is isomorphic to the Klein four-group V_4.

As shown in Figure 1-1, the left figure shows the genus 5 surface (corresponding to $n = 5$), and the right figure shows the genus 17 surface (corresponding to $n = 6$). Both surfaces are embedded in $\mathbb{R}^3$ together with their systoles. Vertices are represented by small blue circles, and edges connect pairs of vertices. In the top view, vertices that coincide are represented by larger circles, coincident edges are represented by black line segments, and non-coincident edges are represented by red line segments.

The homological properties of the closed geodesics formed by the edges of the dual surface X^* have been clarified by the preceding theorems. Next, we investigate the closed geodesics arising from the cellular structure of the surface X itself. Although no definitive theorem has been established yet, a conjecture can be formulated based on our numerical results.

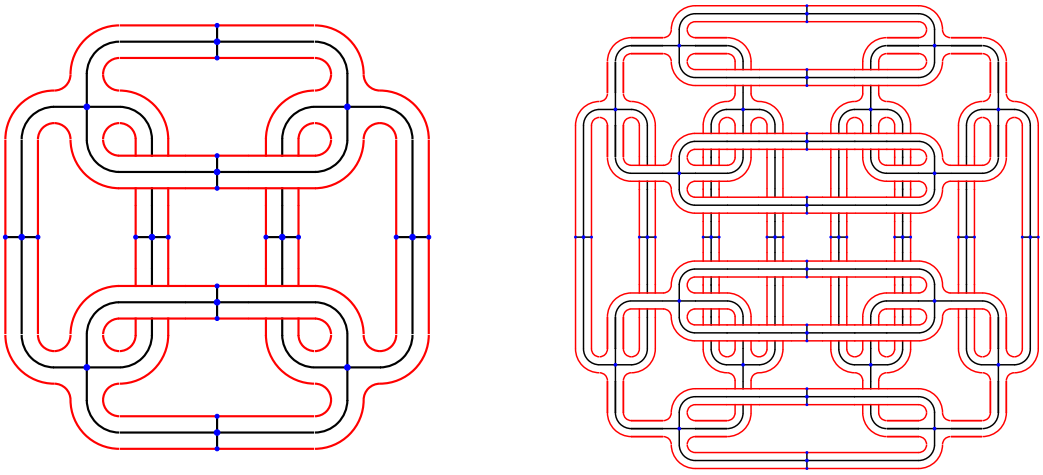

(a) (b)

Figure 1-1 (a) The genus $g = 5$ surface corresponding to $n = 5$; (b) the genus $g = 17$ surface corresponding to $n = 6$. Both surfaces are embedded in $\mathbb{R}^3$ together with their systoles.

Theorem 1.6: Table 1-1 presents the computed results of the homological rank and kernel dimension of the regular embeddings of hypercube graphs Q_n for even values of n.

Table 1-1 Homological ranks of edge geodesics in the regular embedding $M(n, -1)$ for $n = 2k$ (even).

k	$n = 2k$	face dim	dim H_1	Geo num	Ker dim	rank in H_1
2	4	15	2	8	6	2
3	6	95	34	48	24	24
4	8	511	258	256	96	160
5	10	2559	1538	1280	400	880
6	12	12287	8194	6144	1732	4412
7	14	57343	40962	28672	7644	21028
8	16	262143	196610	131072	33920	97152
9	18	1179647	917506	589824	150240	439584

Abbreviations: “face dim” denotes the dimension of two dimensional cellular chain. “Geo num” denotes the number of closed geodesics formed by edges; “Ker dim” denotes the dimension of the kernel of the Hurewicz map.

$$\dim \mathrm{Ker}_n = n \cdot 2^{n-3} \cdot \left(\frac{1}{4} + \frac{1}{2^{\frac{n}{2}-1}} \cdot \left(1 + \frac{\theta_n}{48} \right) \right)$$

where

$$\theta_n = \begin{cases} 0, & 4 \le n < 8 \\ \frac{1}{2}\left(\frac{n}{2}-4\right)\left(\frac{n}{2}-5\right), & 8 \le n \le 18 \end{cases}$$

Table 1-2 The ratio pattern result of edge geodesics in the regular embedding $M(n,-1)$, for $n = 2k$ even

k	$n = 2k$	dim H_1	Geo num	Ker dim	$\frac{\text{Ker dim}}{\text{Geo num}}$	ratio pattern
2	4	2	8	6	0.75	$\frac{3}{4} = \frac{1}{4} + \frac{1}{2}$
3	6	34	48	24	0.5	$\frac{1}{2} = \frac{1}{4} + \frac{1}{4}$
4	8	258	256	96	0.375	$\frac{3}{8} = \frac{1}{4} + \frac{1}{8}$
5	10	1538	1280	400	0.3125	$\frac{5}{16} = \frac{1}{4} + \frac{1}{16}$
6	12	8194	6144	1732	0.281901042	$\frac{433}{1536} = \frac{1}{4} + \frac{1}{32} \cdot \frac{49}{48}$
7	14	40962	28672	7644	0.266601563	$\frac{273}{1024} = \frac{1}{4} + \frac{1}{64} \cdot \frac{17}{16}$
8	16	196610	131072	33920	0.258789063	$\frac{265}{1024} = \frac{1}{4} + \frac{1}{128} \cdot \frac{9}{8}$
9	18	917506	589824	150240	0.254720052	$\frac{1565}{6144} = \frac{1}{4} + \frac{1}{256} \cdot \frac{29}{24}$

Conjecture 1.1: Based on this empirical evidence in Table 1-2, we propose the following closed-form expression for the kernel dimension for all even n:

$$\dim \mathrm{Ker}_n = n \cdot 2^{n-3}\left(\frac{1}{4} + \frac{1}{2^{\frac{n}{2}-1}}\left(1 + \frac{\theta_n}{48}\right)\right),$$

where

$$\theta_n = \begin{cases} 0, & n < 8 \\ \frac{1}{2}\left(\frac{n}{2}-4\right)\left(\frac{n}{2}-5\right), & n \ge 8. \end{cases}$$

We endow the surface with the standard hyperbolic metric and compute the Morse index of the systole function on Teichmüller space. In topological Morse theory, the *index* of a critical point is the dimension of the space of descending directions. For the systole function on surface X, one has the important formula

$$\mathrm{index}(X) = \dim \mathrm{span}\{\nabla \ell_\gamma(X) : \gamma \in S(X)\}.$$

Theorem 1.7: Endowing each right-angled regular polygon of the surface $X = Z(C_n, (D^1, S^0))^*$ with the standard hyperbolic metric, we computed $\mathrm{index}(X)$ for n in the range from 5 to 12. The results are shown in Table 1-3.

Table 1-3 Calculation result of nullity and rank

n	row(V)	row(S)	shape(A)	rank(A)	nullity	nullity$-n$
5	96	20	[116, 120]	108	8	3
6	192	48	[240, 288]	231	9	3
7	384	112	[496, 672]	486	10	3
8	768	256	[1024, 1536]	1013	11	3
9	1536	576	[2112, 3456]	2100	12	3
10	3072	1280	[4352, 7680]	4339	13	3
11	6144	2816	[8960, 16896]	8946	14	3
12	12288	6144	[18432, 36864]	18417	15	3

Conjecture 1.2: There is a close form index formula:

$$\begin{aligned}\text{index}(X) &= \dim\ \text{span}\left\{\nabla \ell_\gamma(X) : \gamma \in S(X)\right\} \\ &= \#systoles - (n+3) = (n-4)2^{n-3} - n - 3.\end{aligned}$$

We investigate discriminant surfaces arising from the characteristic polynomials of 3×3 matrices possessing special symmetries, a study motivated by models in condensed matter physics involving Parity-Time and Minkowski-like pseudo-Hermitian Hamiltonians. In this part, we will demonstrate how these discriminant varieties naturally give rise to ruled and developable surfaces. Through explicit examples, we will explore their geometric properties and discuss some generalizations.

Theorem 1.8 (Ruledness): The generic part of discriminant surface of characteristic polynomial of matrix

$$H = \begin{bmatrix} g_1(f_1, f_2, f_3) & f_1 & f_2 \\ -f_1 & g_2(f_1, f_2, f_3) & f_3 \\ -f_2 & f_3 & g_3(f_1, f_2, f_3) \end{bmatrix}$$

is ruled, where g_1, g_2, g_3 are linear functions of parameters f_1, f_2, f_3, i.e. $g_i = a_{i,1}f_1 + a_{i,2}f_2 + a_{i,3}f_3 + b_i$. Furthermore, the discriminant surface of H is tangent developable and the associated directing curve is the curve of three multiplicity.

1.3 Outline of the Thesis

Chapter 1 of this thesis briefly introduces the research background and the main results of the dissertation.

Chapter 2 focuses on the theory of polyhedral products and its applications to the

topology of surfaces. We investigate the topological properties of a special class of real moment-angle complexes, which are examples of polyhedral products in homotopy theory. The core result is a counting formula for geodesics in homology groups, proved using combinatorial methods. Finally, this result leads to a combinatorial identity. We also study the embedding properties of these real moment-angle complex surfaces.

Chapter 3 extends this problem to the realm of graph-theoretic regular embeddings. The surfaces and maps discussed in Chapter 1 arise as embeddings of hypercube graphs, which can be constructed via polyhedral products. For the remaining embeddings, we study analogous counting problems for closed geodesics, leading to intricate formulas and corresponding structures. In particular, these different embeddings themselves possess internal structures; we perform some calculations and propose conjectures.

Chapter 4 adopts the perspective of hyperbolic geometry on surfaces. The surfaces studied in Chapters 2 and 3 can each be endowed with a natural, highly symmetric hyperbolic structure. We investigate local features of the Teichmüller space near this point, its deformations, and the critical point indices of geodesic functions. Some computations are carried out using computer assistance.

Chapter 5 focuses on algebraic surfaces and ruled surfaces that admit a flat metric. The rulings of these ruled surfaces are also geodesics; notably, they remain geodesics in the ambient space. These are geometric properties of ruled surfaces arising as critical surfaces in non-Hermitian quantum mechanics. We first analyze a special case and then prove a theorem for more general forms.

Appendix A provides an introduction to hyperbolic trigonometry, which is used in computations throughout Chapter 4. Appendix B contains the source code.

CHAPTER 2 POLYHEDRAL PRODUCT HOMOTOPY THEORY

Polyhedral products form an important class of topological spaces constructed under the control of simplicial complexes. Originally conceived as a unification and generalization of several classical constructions, they have since evolved into a fundamental framework connecting combinatorial topology, homotopy theory, commutative algebra, and toric topology[7,9,17,63-64].

Historically, although the terms ”polyhedral product” and ”moment-angle complex” appeared relatively late, their conceptual origins can be traced back to Porter’s work on higher products. Subsequently, with the rise of toric topology, the importance of moment-angle complexes became increasingly prominent. The work of Buchstaber and Panov showed that these spaces are not only natural objects for studying torus actions and simple polytopes but also have deep connections with Davis-Januszkiewicz spaces, Stanley-Reisner face rings, toric manifolds, and quasitoric manifolds, thereby serving as a crucial bridge between toric topology and toric geometry[17,28-30,62].

On the other hand, moment-angle manifolds are also closely related to the theory of intersection quadrics. Studies by López de Medrano, López de Medrano-Verjovsky, and Bosio-Meersseman, among others, have shown that these spaces can also be understood from the perspectives of complex geometry and manifold topology, thus endowing moment-angle theory with a richer geometric background[16,24].

At the algebraic and homological level, moment-angle complexes are intimately connected to Stanley-Reisner rings, Tor algebras, and the Hochster decomposition, allowing combinatorial properties of simplicial complexes to be directly reflected in topological and homological structures. The work of Baskakov, Buchstaber-Panov, Franz, and others has further advanced this direction, establishing moment-angle complexes as an important link between combinatorial commutative algebra and algebraic topology[10,17,28-30,37,62].

The systematic development of polyhedral product theory owes much to the work of Bahri, Bendersky, Cohen, and Gitler. They established a unified framework for the polyhedral product functor and proved the famous stable decomposition theorem, providing a systematic method for studying the homotopy types and homological properties of moment-angle complexes and their real analogues[7-9].

This paper focuses on real moment-angle complexes. Compared to their complex counterparts, real moment-angle complexes often exhibit more intuitive geometric realizations and are more suitable for studying group actions, homological structures, and stable decompositions. In recent years, a series of significant results concerning the surface structures, homological properties, and equivariant decompositions of real moment-angle complexes have emerged, indicating their increasingly important role within polyhedral product theory[23,25,65].

Overall, polyhedral product theory has developed from a specific construction into a unifying perspective spanning combinatorics, topology, and algebra. The real moment-angle complex stands out as a central object possessing both geometric intuitiveness and algebraic richness. Within this context, this paper further discusses the homological properties, stable decompositions, and related issues of real moment-angle complexes[7,9,17,23,65].

2.1 Introduction: Polyhedral Product Functors

Let $[m] = \{1, 2, \dots, m\}$. We first define a category $\mathcal{C}([m])$ whose objects are pairs $(\underline{X}, \underline{A})$, where

$$(\underline{X}, \underline{A}) = \{(X_1, A_1), (X_2, A_2), \dots, (X_m, A_m)\}$$

is a family of based CW-pairs. A morphism in $\mathcal{C}([m])$

$$\underline{f} : (\underline{X}, \underline{A}) \longrightarrow (\underline{Y}, \underline{B})$$

consists of a collection of continuous maps $f_i : X_i \to Y_i$ for $1 \leq i \leq m$, such that $f_i(A_i) \subseteq B_i$ for each i.

Now let K be a simplicial complex with vertex set $[m]$. We regard K as a category whose objects are the simplices of K and whose morphisms are given by inclusions; that is, there is a morphism $\sigma \to \tau$ if and only if $\sigma \subseteq \tau$.

Definition 2.1: The *polyhedral product* is the functor

$$Z(K; -) : \mathcal{C}([m]) \to \mathbf{Top}$$

defined by

$$Z(K; (\underline{X}, \underline{A})) := \mathrm{colim} D \subseteq \prod_{i=1}^{m} X_i,$$

where $D : K \to CW_*$ is the diagram given by

$$D(\sigma) := \prod_{i=1}^{m} W_i, \qquad \text{with} \qquad W_i = \begin{cases} X_i, & \text{if } i \in \sigma, \\ A_i, & \text{if } i \in [m] \setminus \sigma, \end{cases}$$

for each simplex $\sigma \in K$.

Equivalently, the colimit may be described as the union

$$Z(K; (\underline{X}, \underline{A})) = \bigcup_{\sigma \in K} D(\sigma).$$

Similarly, one defines the *smash polyhedral product*

$$\widehat{Z}(K; (\underline{X}, \underline{A}))$$

by replacing Cartesian products with smash products throughout. Namely,

$$\widehat{D}(\sigma) := \bigwedge_{i=1}^{m} W_i, \qquad \text{and} \qquad \widehat{Z}(K; (\underline{X}, \underline{A})) = \bigcup_{\sigma \in K} \widehat{D}(\sigma).$$

Remark 2.1: If all pairs (X_i, A_i) are equal to a single pair (X, A), then the family $(\underline{X}, \underline{A})$ is denoted simply by (X, A). In this case, the automorphism group $\mathrm{Aut}(K)$ acts naturally on $Z(K; (X, A))$.

Remark 2.2: Polyhedral products arise in a remarkably wide range of mathematical settings. For instance, the choice (D^2, S^1) leads to spaces central in toric geometry and topology, while (D^1, S^0) gives real moment-angle complexes, which are closely related to surfaces, number theory, representation theory, and linear programming. Other choices recover spaces connected with right-angled Artin groups and robotics through $(S^1, *)$, right-angled Coxeter groups through $(\mathbb{RP}^\infty, *)$, and complements of coordinate or more general subspace arrangements through $(\mathbb{C}, \mathbb{C}^*)$ and $(\mathbb{R}^n, (\mathbb{R}^n)^*)$. Polyhedral products also appear in the study of monomial ideal rings, free groups and monodromy, combinatorics and aspherical spaces, Whitehead products in homotopy theory, and graph products and quadratic algebras, depending on the choice of the pair (X, A)[7]. This breadth of applications is one of the main reasons why polyhedral products have become a useful organizing framework across several areas of topology, algebra, and geometry.

2.2 Stable Decompositions of a Polyhedral Product

It is well known that the product space X^m of a connected CW-complex with base point admits a stable decomposition as a wedge of smash products. More precisely, there

is a homotopy equivalence[40,54]

$$H : \Sigma(X^m) \longrightarrow \Sigma\left(\bigvee_{I\subset[m]} \widehat{X}^I\right),$$

where the index set I ranges over all non-empty subsequences of $[m] := \{1, 2, \cdots, m\}$.

This may be viewed as a special case of the polyhedral product construction, namely when all pairs (X_i, A_i) are equal to $(X, *)$ and $K = \Delta^m$, the m-simplex. A natural question is whether an analogous decomposition holds for the polyhedral product

$$Z(K; (\underline{X}, \underline{A})) \subset X_1 \times \cdots \times X_m$$

when $K \neq \Delta^m$. In other words, does there exist a stable splitting for polyhedral products associated to an arbitrary simplicial complex K? For general pairs (X, A) and simplicial complexes K, such splittings were established in[8] and[9]Theorem 2.10.

Theorem 2.1: Let K be an abstract simplicial complex on the vertex set $[m]$. Let

$$(\underline{X}, \underline{A}) = \{(X_i, A_i)\}_{i=1}^m$$

be a family of pointed CW-pairs (X_i, A_i, p_i). Then there is a natural pointed homotopy equivalence

$$H : \Sigma\big(Z(K; (\underline{X}, \underline{A}))\big) \longrightarrow \Sigma\left(\bigvee_{I\subset[m]} \widehat{Z}(K_I; (\underline{X}, \underline{A})_I)\right).$$

Here $(\underline{X}, \underline{A})_I$ denotes the restricted family of pointed CW-pairs $\{(X_i, A_i)\}_{i\in I}$, and K_I denotes the full subcomplex (subcategory) of K on the vertex set I.

The James Construction

Let $J(X)$ denote the *James construction* or *James reduced product* on a based space (X, e). Introduced by James[40], $J(X)$ is defined as the free topological monoid generated by X, with the basepoint e serving as the identity element. This construction proceeds explicitly as follows:

Consider the disjoint union $\coprod_{k\geq 1} X^k$, where X^k is the k-fold Cartesian product of X. The space $J(X)$ is obtained by taking the quotient of this disjoint union under the identifications $(x_1, \ldots, x_i, \ldots, x_k) \sim (x_1, \ldots, \hat{x}_i, \ldots, x_k)$ whenever $x_i = e$. Consequently, points of $J(X)$ correspond to equivalence classes of k-tuples $(x_1, \ldots, x_k)$ for $k \geq 0$ with no entry equal to the basepoint e.

$J(X)$ admits a natural filtration $\{J_n(X)\}_{n\geq 0}$ by word length, where $J_n(X)$ is the sub-

space consisting of points represented by tuples of length at most n. This subspace $J_n(X)$ can be identified with the quotient of X^n under the identifications

$$(x_1, \dots, x_{i-1}, e, x_{i+1}, \dots, x_n) \sim (x_1, \dots, x_{j-1}, e, x_{j+1}, \dots, x_n)$$

for any positions i, j containing e. For instance:

- $J_0(X) = e$
- $J_1(X) = X$.
- $J_2(X) = (X \times X)/\{(x, e) \sim (e, x) \mid \forall x \in X\}$.

If X is a CW complex with e a 0-cell, the quotient map $q_n : X^n \to J_n(X)$ identifies the n subcomplexes of X^n where one coordinate is fixed at e. These identifications are performed via homeomorphisms that map cells onto cells. Consequently, $J_n(X)$ inherits a CW complex structure from X^n. The natural inclusions $J_n(X) \subset J_{n+1}(X)$ are cellular, making $J(X) = \bigcup_{n \geq 0} J_n(X)$ a CW complex.

The successive quotients in the filtration are homeomorphic to smash products:

$$J_n(X)/J_{n-1}(X) \cong X^{\wedge n},$$

where $X^{\wedge n}$ denotes the n-fold self-smash product of X.

James proved[40] that $J(X)$ is weak homotopy equivalent to $\Omega\Sigma X$, the based loop space of the reduced suspension of X, whenever X is a connected CW complex. The equivalence arises as follows:

A natural map $\lambda : X \to \Omega\Sigma X$ is defined by the adjunction between suspension and loop spaces, for $x \in X, t \in I$:

$$\begin{array}{rccc} \lambda : & X & \longrightarrow & \Omega\Sigma X \\ & x & \longmapsto & (t \mapsto (t, x)) \end{array}$$

Since $J(X)$ is the free topological monoid on X (with e as identity), the universal property of free monoids allows us to extend λ multiplicatively to a map $\bar{\lambda} : J(X) \to \Omega\Sigma X$. Explicitly, for a point with word length n in $J(X)$ can be represented by a formal product $x_1 x_2 \cdots x_n$:

$$\begin{array}{rccc} \bar{\lambda} : & J(X) & \longrightarrow & \Omega\Sigma X \\ & x_1 x_2 \cdots x_n & \longmapsto & \lambda(x_1) \circ \lambda(x_2) \circ \cdots \circ \lambda(x_n) \end{array}$$

where the product on the right is the loop composition in $\Omega\Sigma X$. This map $\bar{\lambda}$ induces the weak homotopy equivalence.

Equivariant Properties of Stable Splitting Maps

Now suppose that all pairs (X_i, A_i) are equal. In this case, the automorphism group $\mathrm{Aut}(K)$ may be identified with a subgroup of the symmetric group Σ_m, and it acts naturally on both the domain and codomain of the stable splitting map H. Using James–Hopf invariants, A. Al-Raisi[65] showed that the stable splitting map H is in fact equivariant with respect to the $\mathrm{Aut}(K)$-action.

Theorem 2.2: [65]Section 2.2 The adjoint of the stable decomposition,

$$\theta_H : Z(K;(X,A)) \longrightarrow J\Big(\bigvee_{I\subseteq[m]} \widehat{Z}(K_I;(X,A)_I)\Big) \longrightarrow \Omega\Sigma\Big(\bigvee_{I\subseteq[m]} \widehat{Z}(K_I;(X,A)_I)\Big),$$

is $\mathrm{Aut}(K)$-equivariant.

2.3 Real Moment-angle Complexes and Relation to Surface Topology

Let $K = C_n$ denote the cycle graph, i.e. the one-dimensional simplicial complex given by the boundary of an n-gon or a ring with n vertices and n edges. We also use C_n to denote the cyclic group of order n; there will be no ambiguity, as the meaning is determined by whether C_n appears in a topological-theoretic or group-theoretic context.

The real moment-angle manifold $Z(C_n;(D^1,S^0))$ was studied very early on; as a closed surface tiled by quadrilaterals, the first to give its genus formula was perhaps Coxeter[22].

Theorem 2.3: The real moment-angle manifold $Z(C_n;(D^1,S^0))$ corresponding to a cycle graph C_n, for $n \geq 3$, is an oriented surface of genus $g = 1 + (n-4)\cdot 2^{n-3}$.

Remark 2.3: Das[23] directly computed the genus of the *hypercube graph*, i.e., the 1-skeleton of the n-cube, which can be identified with the real moment-angle complex $Z(N_n;(D^1,S^0))$, and obtained the formula $1 + (n-4)2^{n-3}$. The computation proceeds by equivariantly embedding the hypercube graph into the real moment-angle complex $Z(C_n;(D^1,S^0))$. The polyhedral product $Z(N_n;(D^1,S^0))$ corresponding to the edgeless null graph N_n on n vertices is isomorphic to the hypercube graph Q_n. By functoriality of the inclusion $N_n \hookrightarrow C_n$, we obtain a regular embedding $Q_n \hookrightarrow X_n := Z(C_n;(D^1,S^0))$. This genus fact was originally established by Ringel[67] and independently by Beineke and Harary[11]. Subsequently, Catalano et al.[19] classified all regular embeddings of Q_n into surfaces and showed that the smallest possible genus equals $1 + (n-4)2^{n-3}$, while the

largest genus equals $1 + (n-3)2^{n-2}$. The real moment-angle complex $Z(C_n; (D^1, S^0))$ itself provides the unique regular embedding of Q_n into a surface of this smallest genus.

An invitation to the basic research objects

In the special case of the pair solid spheres and their sphere boundary $(D^{m+1}, S^m, *)$ the stable decomposition of $\Sigma(Z(K; (D^{m+1}, S^m)))$ can be simplified as the following form:

Corollary 2.1 (Bahri et al.[9] Corollary 2.24): The stable decomposition theorem states that for all $i, m \geq 0$ and any simplicial complex K, there exists homotopy equivalence maps for the suspension of polyhedral product $Z(K; (D^{m+1}, S^m))$:

$$\Sigma(Z(K; (D^{m+1}, S^m))) \longrightarrow \Sigma\left(\bigvee_{I \notin K} |K_I| * S^{m|I|}\right) \longrightarrow \bigvee_{I \notin K} \Sigma^{2+m|I|}|K_I|,$$

where $|I|$ stands for the size of I , K_I stands for the full subcomplexes of K which have all of their vertices in I, so $K_I = K \cap \Delta^I$ and $|K_I|$ stands for the geometric realization of K_I.

In the more special case where $K = K_n$ (the boundary of the n-gon), and $m = 0$, there is a homotopy equivalence:

$$\Sigma(Z(C_n; (D^1, S^0))) \longrightarrow \bigvee_{I \notin K_n} \Sigma^2|K_I|.$$

Example 2.1: When $n = 4$, K_4 represents a square. The simplices of K_4 consist of the vertices $\{1\}$, $\{2\}$, $\{3\}$, $\{4\}$, and the edges $\{1, 2\}$, $\{2, 3\}$, $\{3, 4\}$, $\{4, 1\}$.

The simplices represented by the sets $\{1, 3\}$, $\{2, 4\}$, all 3-element subsets $\{1, 2, 3\}$, $\{1, 2, 4\}$, $\{1, 3, 4\}$, $\{2, 3, 4\}$, and the full set $\{1, 2, 3, 4\}$ are *not* included in K_4.

For the 2-element subsets, by the definition of K_I, we have $|K_{\{1,3\}}| \cong |K_{\{2,4\}}|$, and both are two discrete points, which have the homotopy type of S^0. For each of the three 3-element subsets, $|K_I|$ forms a "V"-shaped complex, which is contractible. Moreover, $|K_{\{1,2,3,4\}}|$ is equal to K_4 itself and has the homotopy type of a circle.

Therefore, by the preceding corollary, we obtain:

$$\Sigma(Z(C_4; (D^1, S^0))) \simeq \bigvee_{i=1}^{2} \Sigma^2(S^0) \bigvee \Sigma^2(S^1) = \bigvee_{i=1}^{2} S^2 \bigvee S^3.$$

Hence, $H_1(Z(C_4; (D^1, S^0))) = \mathbb{Z}^2$, and the rank of this group agrees with the genus formula $g = 1$.

Example 2.2: When $n = 5$, K_5 represents a pentagon. Its simplices are the five vertices $\{1\}$, $\{2\}$, $\{3\}$, $\{4\}$, $\{5\}$ and the five edges $\{1, 2\}$, $\{2, 3\}$, $\{3, 4\}$, $\{4, 5\}$, $\{5, 1\}$.

The simplices represented by the 2-element sets $\{1,3\}$, $\{2,4\}$, $\{3,5\}$, $\{1,4\}$, $\{2,5\}$; all 3-element subsets $\{1,2,4\}$, $\{2,3,5\}$, $\{1,3,4\}$, $\{2,4,5\}$, $\{1,3,5\}$; all 4-element subsets $\{1,2,3,4\}$ $\{1,2,3,5\}$, $\{1,3,4,5\}$, $\{2,3,4,5\}$; and the full set $\{1,2,3,4,5\}$ are *not* included in K_5.

By the definition of K_I, for each of the listed 2-element and 3-element subsets I, the complex $|K_I|$ has the homotopy type of two discrete points, S^0. For a 3-element subset, such as $\{1,2,4\}$, this corresponds to two vertices connected by an edge and one isolated vertex. For any 4-element subset I, $|K_I|$ is a path of 3 edges, hence contractible, and contributes no wedge summand. Finally, $|K_{\{1,2,3,4,5\}}|$ is the pentagon itself and has the homotopy type of a circle, S^1.

Therefore, by the preceding corollary, we obtain:

$$\Sigma(Z(C_5;(D^1,S^0))) \simeq \bigvee_{i=1}^{10} \Sigma^2(S^0) \bigvee \Sigma^2(S^1) = \bigvee_{i=1}^{10} S^2 \bigvee S^3.$$

Hence, $H_1(Z(C_5;(D^1,S^0))) = \mathbb{Z}^{10}$, and the rank of this group agrees with the genus formula $g = 5$.

Example 2.3: When $n = 6$, K_6 is the hexagon. Its simplices are the six vertices $\{1\}, \{2\}$, $\{3\}, \{4\}, \{5\}, \{6\}$ and the six edges $\{1,2\}$, $\{2,3\}$, $\{3,4\}$, $\{4,5\}$, $\{5,6\}$, $\{6,1\}$.

The following simplices, represented by their vertex subsets, are *not* included in K_6. According to the definition of K_I, we analyze the homotopy types they contribute to the final wedge sum. Note that although all simplices of Δ^6 with more than two vertices are absent from K_6, we focus only on those that contribute non-contractible homotopy types.

Some 2-element subsets (diagonals): $\{1,3\}$, $\{1,4\}$, $\{1,5\}$, $\{2,4\}$, $\{2,5\}$, $\{2,6\}$, $\{3,5\}$, $\{3,6\}$, $\{4,6\}$. For each of them, $|K_I|$ consists of two discrete points, so $\Sigma^2|K_I|$ contributes a copy of S^2. These give 9 copies of S^2.

All 3-element subsets: Among these, two types contribute non-contractible spaces.

• The first type, the configuration such as $\{1,2,4\}$ and $\{1,2,5\}$ and their images under the C_6 rotation action, yield $|K_I|$ with the homotopy type of two discrete points. There are 12 such subsets, each contributing an S^2.

• The second type, only 2 subsets $\{1,3,5\}$ and $\{2,4,6\}$, have $|K_I|$ with three discrete points, which has the homotopy type of $\bigvee^2 S^1$ after once suspension. Each contributes a homotopy type $\bigvee^2 S^2$ after twice suspension.

All 4-element subsets: Non-contractible contributions come from the C_6-orbits of two types of 4-element subsets. The first type is represented by $\{1,2,4,5\}$, whose orbit

consists of the three subsets: $\{1,2,4,5\}$, $\{2,3,5,6\}$, and $\{1,3,4,6\}$. The second type is represented by $\{1,2,3,5\}$, whose orbit under the cyclic group action contains six distinct subsets. In all these nine cases, $|K_I|$ has the homotopy type of S^0, so $\Sigma^2|K_I| \simeq S^2$, with each subset contributing one copy of S^2.

All 5-element subsets: All such subsets yield contractible spaces (K_I is always a path of 4 edges), and thus contribute no wedge summands.

The full set $[6]$**:** Here, $|K_{[6]}|$ is the boundary of the hexagon, which has the homotopy type of S^1. Therefore, it contributes $\Sigma^2 S^1 \simeq S^3$.

Therefore, by the preceding corollary, we obtain:

$$\Sigma(Z(C_6;(D^1,S^0))) \simeq \bigvee_{i=1}^{30} \Sigma^2(S^0) \bigvee_{i=1}^{2} \Sigma^2(\bigsqcup^{3} *) \bigvee \Sigma^2(S^1) = \bigvee_{i=1}^{34} S^2 \bigvee S^3.$$

Hence, $H_1(Z(C_6;(D^1,S^0))) = \mathbb{Z}^{34}$, and the rank of this group agrees with the genus formula $g = 17$.

Application of equivalent stable splitting theorem

In the case $K = C_n$, $Aut(C_n) = D_{2n}$, the dihedral group with subgroup cyclic group C_n, the equivalent stable splitting theorem has interesting consequences. The real moment-angle manifold is the conduit through which Al-Raisi[65] uses Theorem 2.2 to link combinatorics of C_n and the rotation action of C_n on a choice of basis for the cohomology of a surface of genus $g = 1 + (n-4)\cdot 2^{n-3}$.

In this setting, one may choose generators indexed, up to sign, by subsequences

$$I = (i_1, \dots, i_r) \subset \{1, \dots, n\},$$

where I is required to have gap number greater than 1. Here the gap number refers to the number of connected components of I when regarded as a subset of the cyclically ordered set $\{1, \dots, n\}$. In other words, we view $\{1, \dots, n\}$ as arranged on a circle, and I decomposes into maximal consecutive blocks; the gap number counts how many such blocks occur. The condition that the gap number is greater than 1 means that I does not form a single contiguous block around the circle.

Equivalently, these generators may be encoded by binary colorings of an n-bead necklace: a black bead records membership in I, while a white bead records its complement. Under this correspondence, the action of C_n becomes the usual rotation action on

necklaces. Thus, the problem of understanding the C_n-orbits in

$$H^2\big(\Sigma Z(K_n;(D^1,S^0))\big)$$

reduces to a combinatorial orbit-counting problem.

There are two natural ways to count these orbits.

Method 1: Global orbit counting via Burnside's lemma

The first counts all admissible orbits at once. By Burnside's lemma, the number of rotational equivalence classes of binary colorings of an n-bead necklace is

$$\frac{1}{n}\sum_{d|n}\phi(d)\,2^{n/d},$$

where $\phi(d)$ is the Euler totient function which counts the number of integers up to n that are relatively prime to n. However, not every binary coloring contributes to the cohomology basis considered above: the excluded cases are exactly those colorings in which all beads of the same color occur consecutively around the necklace. There are precisely $n+1$ such colorings, namely the two constant colorings together with the $n-1$ colorings having one contiguous black block of length i, for $1 \le i \le n-1$. Hence the total number of relevant C_n-orbits is

$$\frac{1}{n}\sum_{d|n}\phi(d)\,2^{n/d} - (n+1).$$

Method 2: Stratified orbit counting via primitive necklaces decomposition

The second method counts the same orbits by their exact size. A word of length n is called an *aperiodic word* if it has n distinct rotations or equivalently the stabilizer group of this coloring is trivial group under the action of cyclic group C_n. An equivalence class of an aperiodic word under rotation is called a *primitive necklace* (also called *Lyndon word* or *primitive strings*). If $d \mid n$ with $1 < d < n$, then an orbit of size d corresponds to a coloring obtained by repeating an aperiodic word of length d, or equivalently to a primitive d-necklace on a two-letter alphabet. By Moreau's formula, the number of primitive d-necklaces is

$$M(2,d) = \frac{1}{d}\sum_{d_1|d}\mu(d_1)\,2^{d/d_1},$$

where μ is the Möbius inversion function:

$$\mu(n) = \begin{cases} 1 & \text{if } n = 1, \\ (-1)^k & \text{if } n \text{ is square-free with } k \text{ distinct prime factors,} \\ 0 & \text{if } n \text{ has a squared prime factor.} \end{cases}$$

This number is the number of C_n-orbits of size d arising from basis elements up to sign. Therefore, for every proper divisor d of n with $1 < d < n$, the number of such size-d orbits is

$$\frac{1}{d}\sum_{d_1|d} \mu(d_1)\, 2^{d/d_1}.$$

For orbits of full size n, one again starts from primitive necklaces, now of length n. In this case one must remove the $n-1$ primitive necklaces in which all black beads occur consecutively, since these correspond to excluded colorings and do not contribute to the cohomology basis. Thus the number of orbits of size n is

$$M(2,n) - (n-1) = \frac{1}{n}\sum_{d|n} \mu(d)\, 2^{n/d} - (n-1).$$

Since every relevant orbit has size d for some divisor d of n, the total number of orbits is the sum of the numbers of orbits of each possible size. Equating this decomposition by orbit size with the Burnside count above yields the following identity.

Theorem 2.4: [65]Proposition 3.5.10 For $n \geq 4$, there is an identity

$$\frac{1}{n}\left(\sum_{d|n} \mu(d) 2^{\frac{n}{d}}\right) - (n-1) + \sum_{\substack{d|n \\ 1<d<n}} \left(\frac{1}{d}\sum_{d_1|d} \mu(d_1) 2^{\frac{d}{d_1}}\right) = \frac{1}{n}\left(\sum_{d|n} \phi(d) 2^{\frac{n}{d}}\right) - (n+1)$$

relating the Möbius inversion function and the Euler totient function by equating the two different orbit counting methods.

2.4 Enumeration Formulas for Homological Ranks of Closed Geodesics on Hyperbolic Surfaces and Combinatorial Identities

We have constructed an embedding of the hypercube graph in the real moment-angle complex and computed its genus. This reveals an interesting geometric relationship between the hypercube graph and real moment-angle complexes. We now turn our attention to the dual complex of the real moment-angle complex $Z(C_n, (D^1, S^0))$.

Dual complex and hyperbolic geometric structure

The definition of tessellation is adopt from[66]Sec 6.8.

Here is a more accessible, plain-English rewrite of those definitions:

Definition 2.2: A *tessellation* (or tiling) of an n-dimensional topological manifold X is a way of covering X with a collection $\mathcal{P}$ of n-dimensional convex pieces (like polyhedra) such that:

（1）the pieces do not overlap (their interiors are disjoint);

（2）together, they cover all of X;

（3）every point in X has a neighborhood that meets only finitely many pieces.

Definition 2.3: A tessellation $\mathcal{P}$ of X is called *exact* if every face (or side) of every piece is shared by exactly two pieces. In other words, there are no gaps or hanging edges.

Definition 2.4: A *regular tessellation* of X is an exact tessellation where all the pieces are identical regular polytopes (like perfect squares, cubes, or their higher-dimensional analogues).

Definition 2.5: A tessellation of a Riemann surface is called platonic if its symmetry group can move any flag (a triple consisting of a vertex, an edge, and a face, all incident to each other) to any other flag. Such a tessellation is also known as a regular map. A Riemann surface is called platonic if it admits at least one platonic tessellation.

A map M on a surface S can be understood as a graph G embedded in S such that each connected component of the complement $S \setminus G$ is a 2-cell (a face), i.e., homeomorphic to an open disk.

Definition 2.6 (Dual Map): Let M be a map on a surface S. Its **dual map** M^* (or dual embedding G^*) is defined as follows:

• **Vertices (dual vertices):** For each face f of M (i.e., a connected component of $S \setminus G$), choose a point v_f in the interior of f. These points serve as the vertices of M^*. Consequently, $V(M^*) \leftrightarrow F(M)$.

• **Edges (dual edges):** For each edge e of M, it is adjacent to two faces f_1, f_2 in the embedding (allowing the case $f_1 = f_2$, where both sides of the edge belong to the same face). Draw an arc e^* on the surface connecting v_{f_1} and v_{f_2}, satisfying that it intersects the original edge e transversely in exactly one point and e^* does not intersect any other edge of G (except at that single transverse intersection point with e). The homotopy classes of these arcs (with endpoints fixed within their faces) determine the dual edges. Therefore, $E(M^*) \leftrightarrow E(M)$.

• **Faces (dual faces):** After drawing all dual edges, we obtain an embedded graph $G^* \subset S$. Its faces correspond bijectively to the vertices of the original graph: around each primal vertex $u \in V(M)$, a dual face f_u^* is formed. Thus, $F(M^*) \leftrightarrow V(M)$.

Under the definition given above, the dual map satisfies the following properties: The double dual $(M^*)^*$ is naturally isomorphic to M (isomorphism in the topological sense, i.e., as graphs up to homeomorphism).

Our main object of study next is the dual map $Z(C_n, (D^1, S^0))^*$, which is composed of 2^n n-gons glued together, with four edges meeting at each vertex. A schematic of one-quarter of $Z(C_5, (D^1, S^0))$ unfolded onto the plane.

Structure of one piece of n=5

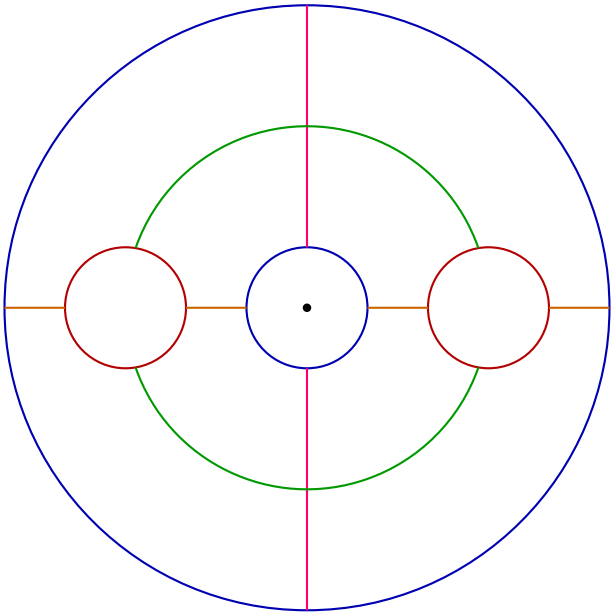

Symmetric embedding of surfaces

We study the embedding properties of closed surfaces and their 1-skeletons into higher-dimensional spaces. Although the ultimate goal is embedding into three-dimensional Euclidean space for its advantages in visualization, and because every orientable closed surface of any genus can be embedded there, it is natural to first consider embeddings into higher-dimensional Euclidean spaces and spheres, as this corresponds more directly with the intrinsic construction of the surfaces.

Specifically, by definition, the complex $Z(C_n, (D^1, S^0))$ is a subcomplex of the standard high-dimensional cube I^n. Therefore, it can be naturally embedded into Euclidean space $\mathbb{R}^n$ by taking the cube as $[-1, 1]^n$, so that its vertices lie exactly at the coordinates $(\epsilon_1, \dots, \epsilon_n)$, where each $\epsilon_i = \pm 1$.

Based on this embedding, we consider the geometric dual subdivision of the complex on the surface: each vertex of the dual is placed at the center of the corresponding face of the primal complex. Then, on the original surface, we connect these dual vertices sequentially with straight line segments to form the edges of the dual complex; the regions enclosed by these edges on the original surface constitute the faces of the dual complex. Finally, by projecting these regions as a whole onto the unit sphere S^{n-1}, we complete the geometric construction of the new surface.

Theorem 2.5: One can embed $Z(C_n, (D^1, S^0))^*$ into the $(n-1)$-dimensional sphere $S^{n-1} \subset \mathbb{R}^n$ with the standard round metric, such that every edge is a geodesic arc, and also require that all edges have the same length $\arccos\left(\frac{n-3}{n-2}\right)$.

Proof: In n-dimensional Euclidean space $\mathbb{R}^n$, the geodesics on the $(n-1)$-dimensional unit sphere S^{n-1} with the standard round metric are precisely the great circles obtained by intersecting the sphere with a two-dimensional plane passing through the center (origin). We can write the parametric equation as follows: given two linearly independent unit vectors $\mathbf{u}, \mathbf{v} \in S^{n-1}$ (satisfying $\langle \mathbf{u}, \mathbf{v} \rangle = 0$, i.e., orthogonal), the intersection of the plane spanned by them with S^{n-1} (i.e., the great circle) has the parametric equation:

$$\mathbf{r}(t) = \cos(t) \cdot \mathbf{u} + \sin(t) \cdot \mathbf{v}, \quad t \in [0, 2\pi)$$

Here, taking $t = 0$ corresponds to the point $\mathbf{u}$, and $t = \pi/2$ corresponds to the point $\mathbf{v}$. The parameter t is the arc-length parameter starting from $\mathbf{u}$, because $\|\mathbf{r}'(t)\| = 1$. Therefore, if we take the parameter range $t \in [0, \pi/2]$, the length of this arc connecting $\mathbf{u}$ and $\mathbf{v}$ is $\pi/2$.

Even if $\mathbf{u}$ and $\mathbf{v}$ are not orthogonal ($\langle \mathbf{u}, \mathbf{v} \rangle \neq 0$), the geodesic (great circular arc) connecting them still exists and is unique, but the basis in its parametric equation needs to be reconstructed from $\mathbf{u}$ and $\mathbf{v}$.

Project $\mathbf{v}$ onto $\mathbf{u}$ to obtain the component parallel to $\mathbf{u}$, and then find the component perpendicular to $\mathbf{u}$.

$$\mathbf{v}_{\parallel} = \langle \mathbf{v}, \mathbf{u} \rangle \mathbf{u}, \quad \mathbf{v}_{\perp} = \mathbf{v} - \mathbf{v}_{\parallel}$$

Normalize the perpendicular component to obtain a unit vector $\mathbf{w}$ orthogonal to $\mathbf{u}$.

$$\mathbf{w} = \frac{\mathbf{v}_{\perp}}{\|\mathbf{v}_{\perp}\|}$$

Here, $\|\mathbf{v}_{\perp}\| = \sqrt{1 - \langle \mathbf{u}, \mathbf{v} \rangle^2}$. The parametric equation of the geodesic (great circular arc)

connecting **u** and **v** is:

$$\mathbf{r}(t) = \cos(t) \cdot \mathbf{u} + \sin(t) \cdot \mathbf{w}, \quad t \in [0, \theta]$$

where $\theta = \arccos(\langle \mathbf{u}, \mathbf{v} \rangle)$ is the spherical angular distance (i.e., the great circular arc length) between **u** and **v**. When $t = 0$, $\mathbf{r}(0) = \mathbf{u}$. When $t = \theta$, because $\cos\theta = \langle \mathbf{u}, \mathbf{v} \rangle$ and $\sin\theta = \|\mathbf{v}_\perp\|$, substituting gives $\mathbf{r}(\theta) = \mathbf{v}$.

The parametric equation of the unique geodesic (shortest path) connecting two points **u** and **v** on the unit sphere ($\langle \mathbf{u}, \mathbf{v} \rangle \neq -1$) is:

$$\mathbf{r}(t) = \cos(t)\,\mathbf{u} + \sin(t)\,\frac{\mathbf{v} - \langle \mathbf{v}, \mathbf{u} \rangle \mathbf{u}}{\sqrt{1 - \langle \mathbf{u}, \mathbf{v} \rangle^2}}, \quad t \in [0,\ \arccos(\langle \mathbf{u}, \mathbf{v} \rangle)]$$

In $\mathbb{R}^n$, take the standard basis $\mathbf{e}_1, \ldots, \mathbf{e}_n$. For each vertex in the dual graph,

$$v^* = (a_1, \ldots, *, *, \ldots, a_n),$$

which corresponds to a face in the original graph, with coordinates where the i-th and $(i+1)$-th positions are $*$ and the remaining coordinates are arbitrarily chosen as 0 or 1, with indices taken modulo n. The coordinate vector is:

$$((-1)^{a_1}, \ldots, 0, 0, \ldots, (-1)^{a_n}),$$

where the i-th and $(i+1)$-th components are 0, and the j-th component in the remaining positions is $\epsilon_j := (-1)^{a_j} \in \{\pm 1\}$. Project this onto a point $\mathbf{u}_{i,i+1}$ on the sphere such that $\|\mathbf{u}_{i,i+1}\| = 1$, so its coordinates are

$$\frac{1}{\sqrt{n-2}}((-1)^{a_1}, \ldots, 0, 0, \ldots, (-1)^{a_n}).$$

After embedding all $n \cdot 2^{n-2}$ points in this way, we consider how to embed the edges. Each edge $e^* = (\ldots, a_{i-1}, *, a_{i+1}, \ldots)$ in the dual graph connects two vertices: $(\ldots, a_{i-2}, *, *, a_{i+1}, \ldots)$ and $(\ldots, a_{i-1}, *, *, a_{i+2}, \ldots)$. On the original surface complex, this edge consists of two straight line segments, i.e.

$$(\ldots, \epsilon_{i-2}, 0, 0, \epsilon_{i+1}, \epsilon_{i+2}, \ldots) -$$
$$-(\ldots, \epsilon_{i-2}, \epsilon_{i-1}, 0, \epsilon_{i+1}, \epsilon_{i+2}, \ldots) -$$
$$-(\ldots, \epsilon_{i-2}, \epsilon_{i-1}, 0, 0, \epsilon_{i+2}, \ldots)$$

These two line segments can be parameterized as

$$(\ldots, \epsilon_{i-2}, t_1\epsilon_{i-1}, 0, \epsilon_{i+1}, \epsilon_{i+2}, \ldots),\ t_1 \in [0, 1]$$

and

$$(\ldots, \epsilon_{i-2}, \epsilon_{i-1}, 0, \epsilon_{i+1}(1 - t_2), \epsilon_{i+2}, \ldots),\ t_2 \in [0, 1].$$

The intermediate point lies in the two-dimensional plane spanned by the endpoints, so its projection onto the unit sphere is a great circular arc. We only need to consider the endpoints of the great circular arc.

Assume the two vertices, embedded as defined above, are $\mathbf{u}_{i-1,i}$ and $\mathbf{u}_{i,i+1}$. The inner product of these two points is

$$\langle \mathbf{u}_{i-1,i}, \mathbf{u}_{i,i+1} \rangle = \frac{n-3}{n-2}.$$

Therefore, the spherical angle (i.e., the shortest geodesic arc length) between the two points is

$$\theta = \arccos\left(\frac{n-3}{n-2}\right).$$

Using the general parameterization formula given earlier, this edge can be embedded as the unit-speed geodesic arc connecting $\mathbf{u}_{i-1,i}$ and $\mathbf{u}_{i,i+1}$:

$$\mathbf{r}(t) = \cos(t) \cdot \mathbf{u}_{i-1,i} + \sin(t) \frac{\mathbf{u}_{i,i+1} - \langle \mathbf{u}_{i,i+1}, \mathbf{u}_{i-1,i} \rangle \mathbf{u}_{i-1,i}}{\sqrt{1 - \langle \mathbf{u}_{i-1,i}, \mathbf{u}_{i,i+1} \rangle^2}}, \quad t \in \left[0, \arccos\left(\frac{n-3}{n-2}\right)\right]$$

This parameterization is unit-speed, so the length of each edge is $\arccos\left(\frac{n-3}{n-2}\right)$. In this way, all $n \cdot 2^{n-1}$ edges can be embedded.

Next, we consider the embedding of faces. It suffices to prove that for a high-dimensional cube $[-1, 1]^n$, the projections of each two-dimensional face onto the unit sphere are disjoint except at their boundaries.

The interiors of the projections of different two-dimensional faces do not intersect because radial projection is injective. Since the cube is convex and the origin lies in its interior, each ray from the origin intersects the boundary of the cube at exactly one point. Therefore, radial projection establishes a bijection between the boundary of the cube and the unit sphere. Each two-dimensional face projects onto the unit sphere such that, except for possible overlaps at boundaries, the interior regions are mutually disjoint. ■

Remark 2.4: In Theorem 2.5, the embedded manifold is not smooth except in the case $n = 3$. Specifically, when $n = 3$, the embedded manifold is exactly the entire space S^2, and hence is smooth. For $n \geq 4$, the manifold is only piecewise smooth, with the dihedral angle between each pair of faces given by $\arccos\left(-\frac{1}{2n-5}\right)$. For detailed proof, see the Theorem 2.6 below.

Theorem 2.6 (Spherical angles after radial projection): Let $n \geq 4$ and work in the Euclidean space $\mathbb{R}^n$ with the standard inner product $\langle \cdot, \cdot \rangle$. Let $\epsilon_j \in \{-1, 1\}$ for all j. To investigate the local geometry around a point P and its four adjacent points, we define

points $P, A, B, C, D \in \mathbb{R}^n$ as follows:

For all coordinates $j \notin \{i-1, i, i+1, i+2\}$, set them to be equal to the given sign

$$P_j = A_j = B_j = C_j = D_j = \epsilon_j.$$

On the coordinates $(i-1, i, i+1, i+2)$, set

$$P = (\epsilon_{i-1}, 0, 0, \epsilon_{i+2}), \quad A = (0, 0, -1, \epsilon_{i+2}), \quad B = (0, 0, 1, \epsilon_{i+2}),$$
$$C = (\epsilon_{i-1}, 1, 0, 0), \quad D = (\epsilon_{i-1}, -1, 0, 0),$$

where the displayed 4-tuples occupy the index positions $(i-1, i, i+1, i+2)$. A schematic diagram of the geometry is depicted in Figure 2-1.

Let the radial projection onto the unit sphere S^{n-1} be

$$\widehat{X} := \frac{X}{\|X\|} \in S^{n-1}.$$

Then the spherical angles at $\widehat{P}$ satisfy

$$\angle \widehat{A}\,\widehat{P}\,\widehat{B} = \angle \widehat{A}\,\widehat{P}\,\widehat{C} = \arccos\left(-\frac{1}{2n-5}\right),$$

independent of the choices of $\{\epsilon_j\}$.

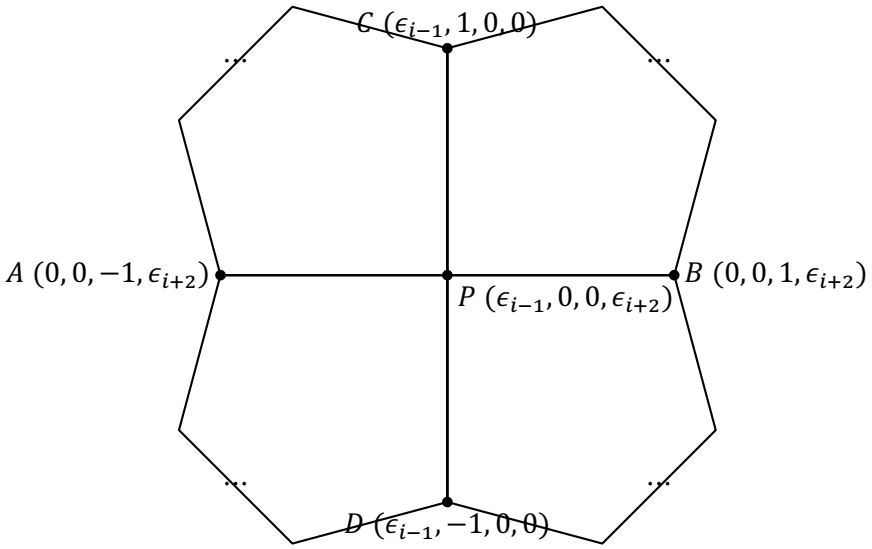

Figure 2-1 Local geometry around a point P and its four adjacent points A, B, C, D

Proof: First compute the relevant dot products. The common $(n-4)$ coordinates contribute $n-4$ to every dot product. Using the specified 4-tuples:

$$\langle P, A \rangle = (n-4) + (\epsilon_{i+2} \cdot \epsilon_{i+2}) = (n-4) + 1 = n-3,$$

$$\langle P, B \rangle = n-3, \qquad \langle P, C \rangle = (n-4) + (\epsilon_{i-1} \cdot \epsilon_{i-1}) = (n-4) + 1 = n-3,$$

$$\langle A, B \rangle = (n-4) + ((-1) \cdot 1) + (\epsilon_{i+2} \cdot \epsilon_{i+2}) = (n-4) - 1 + 1 = n-4,$$

$$\langle A, C\rangle = (n-4) + 0 = n-4.$$

Dividing by $n-2$ gives

$$\langle \widehat{P}, \widehat{A}\rangle = \langle \widehat{P}, \widehat{B}\rangle = \langle \widehat{P}, \widehat{C}\rangle = \frac{n-3}{n-2}, \qquad \langle \widehat{A}, \widehat{B}\rangle = \langle \widehat{A}, \widehat{C}\rangle = \frac{n-4}{n-2}.$$

Then we study the spherical angle formula at $\widehat{P}$. Let $p = \widehat{P}$ and $x = \widehat{A}$, $y = \widehat{B}$ (or $y = \widehat{C}$). The tangent space at p is $T_pS^{n-1} = \{v : \langle v, p\rangle = 0\}$. Project x, y to T_pS^{n-1} by

$$u := x - \langle x, p\rangle p, \qquad v := y - \langle y, p\rangle p.$$

Then $\angle xpy$ equals the Euclidean angle between u and v:

$$\cos\angle xpy = \frac{\langle u, v\rangle}{\|u\| \cdot \|v\|}.$$

A direct expansion using $\|p\| = 1$ yields

$$\langle u, v\rangle = \langle x, y\rangle - \langle x, p\rangle\langle y, p\rangle,$$

and

$$\|u\|^2 = 1 - \langle x, p\rangle^2, \qquad \|v\|^2 = 1 - \langle y, p\rangle^2.$$

In our case $\langle x, p\rangle = \langle y, p\rangle = \frac{n-3}{n-2}$, so

$$\cos\angle xpy = \frac{\langle x, y\rangle - \langle x, p\rangle^2}{1 - \langle x, p\rangle^2}.$$

Using $\langle x, y\rangle = \frac{n-4}{n-2}$ and $\langle x, p\rangle = \frac{n-3}{n-2}$,

$$\cos\angle xpy = \frac{\frac{n-4}{n-2} - \left(\frac{n-3}{n-2}\right)^2}{1 - \left(\frac{n-3}{n-2}\right)^2} = -\frac{1}{2n-5}.$$

Taking $y = \widehat{B}$ gives $\angle\widehat{A}\widehat{P}\widehat{B} = \arccos\left(-\frac{1}{2n-5}\right)$, and taking $y = \widehat{C}$ gives the same value because the dot products used above satisfy $\langle \widehat{A}, \widehat{C}\rangle = \langle \widehat{A}, \widehat{B}\rangle$ and $\langle \widehat{P}, \widehat{C}\rangle = \langle \widehat{P}, \widehat{B}\rangle$. Therefore

$$\angle \widehat{A}\,\widehat{P}\,\widehat{B} = \angle \widehat{A}\,\widehat{P}\,\widehat{C} = \arccos\left(-\frac{1}{2n-5}\right).$$

■

Theorem 2.7: For $n = 4$, there exists a smooth embedding $Z(C_4, (D^1, S^0))^* \hookrightarrow S^3$, which can be realized by the Clifford torus and a subcomplex on it.

Proof: The Clifford torus is a special, flat two-dimensional torus embedded in four-dimensional Euclidean space $\mathbb{R}^4$ (or in its submanifold, the three-dimensional sphere S^3).

It can be simply defined as the surface in $\mathbb{R}^4$ given by the equations

$$\left\{(x_1, x_2, x_3, x_4) \in \mathbb{R}^4 : x_1^2 + x_2^2 = \frac{1}{2},\ x_3^2 + x_4^2 = \frac{1}{2}\right\}.$$

Clearly, it lies on the unit sphere S^3, since $x_1^2 + x_2^2 + x_3^2 + x_4^2 = \frac{1}{2} + \frac{1}{2} = 1$.

It admits a parametrization given by

$$x_1 = \frac{1}{\sqrt{2}}\cos u, \quad x_2 = \frac{1}{\sqrt{2}}\sin u, \quad x_3 = \frac{1}{\sqrt{2}}\cos v, \quad x_4 = \frac{1}{\sqrt{2}}\sin v$$

with $u, v \in [0, 2\pi)$. One can see that it is essentially a two-dimensional torus $T^2 = S^1 \times S^1$, where both circles have radius $\frac{1}{\sqrt{2}}$, corresponding respectively to the two orthogonal planes (x_1, x_2) and (x_3, x_4) in $\mathbb{R}^4$.

Let $C = \{0, \frac{\pi}{2}, \pi, \frac{3\pi}{2}\}$. Taking the parameters u, v to be values in C, we obtain the coordinates of 16 points: $(0, 0, \pm 1, \pm 1)$, $(0, \pm 1, \pm 1, 0)$, $(\pm 1, \pm 1, 0, 0)$, $(\pm 1, 0, 0, \pm 1)$. These can serve as the embedding points of the surface for $n = 4$. The edges are obtained by varying only one of the parameters u or v by $\pi/2$. ■

In the following part, we will consider methods for embedding closed surfaces into three-dimensional Euclidean space.

To efficiently visualize the topological structure of large-scale closed surfaces, we adopt a standard simplification method: tubular regions of the form $S^1 \times D^1$ are reduced to line segments, and cross-shaped junctions are simplified into nodes where line segments intersect. Thus, the diagram becomes a one-dimensional CW complex that fully encodes the homeomorphism type of the surface. Consequently, the two-dimensional closed manifold is simplified into a one-dimensional CW complex without endpoints.

There is a canonical way to reconstruct the original surface from this diagram: treat the diagram D as the core of a three-dimensional solid handlebody H, thicken it into solid handles by taking a regular neighborhood of the embedding of this graph in three-dimensional Euclidean space, and finally take the boundary ∂H of this solid handlebody to obtain a closed surface homeomorphic to the original one.

In schematic diagrams, nodes at line intersections are typically represented as solid dots. To further express the specific embedding of the surface in three-dimensional space, when two lines representing the surface cross in projection, we follow the drawing convention of knot diagrams: the line being covered is indicated with a break to clarify the over-and-under relationship of the embedding.

Construction 2.7: Starting with the initial case $n = 4$, draw a square centered at the origin with side length 2 and sides parallel to the coordinate axes. For any $n \geq 5$, first

duplicate the diagram for size $n-1$ twice, shifting one copy left and the other right by a distance of 2^{n-4}; then multiply all y-coordinates of the resulting diagram by 2, effectively stretching its vertical segments to twice their original length. Next, rotate a copy of the current diagram by 90° about the origin (applying the coordinate transformation $(x, y) \mapsto (-y, x)$) and superimpose it onto the original to obtain the final pattern for size n. When handling all intersections except corner points, they are classified into two types: if an intersection lies at the midpoint of any segment, it is marked as a "node" with a solid dot in the same color as that segment; all other intersections receive a visual 3D layering treatment where horizontal lines always lie on top of vertical lines, i.e., a short portion of the vertical line is obscured near the intersection to achieve depth separation.

Schematic diagrams for $n = 5, 6, 7, 8$ are shown in Figure 2-3, Figure 2-4, Figure 2-5, and Figure 2-6, respectively.

We now discuss why the embedding construction described above suits our needs, along with some of its properties.

Theorem 2.8: Construction 2.7 above provides an embedding of surfaces into $\mathbb{R}^3$; the resulting surface is exactly the object of our study, i.e. $Z(C_n, (D^1, S^0))$.

Proof: We prove this by induction. First, for the base case $n = 4$, the line arrangement is a square, which represents a torus. We know that this corresponds to the polyhedral complex $Z(C_n, (D^1, S^0))$. Subsequently, the larger-scale surface for $n+1$ is obtained by taking two surfaces of scale n, removing two small disks (holes) from each, and then connecting these holes with a handle. The resulting surface is exactly the surface of scale $n+1$, which is consistent with the definition given by the polyhedral product. ■

Theorem 2.9: For $n \geq 5$, the isometry group of the surface embedded in $\mathbb{R}^3$ by Construction 2.7 is isomorphic to the Klein four-group V_4.

Proof: Since each surface embedding is obtained by thickening its corresponding line graph, it suffices to show that the line graph itself has the same symmetry. The line graph of order $n+1$ is constructed from that of order n by a doubling and superposition procedure; we therefore proceed by induction on n.

Base case $n = 5$. We denote the four points in the space as follows, corresponding to the four rectangles in the embedding:

$$A = (a, 0, -b), \quad B = (-a, 0, -b),$$
$$C = (0, a, \ \ b), \quad D = (0, -a, \ \ b),$$

with $a > 0$, $b > 0$, and $a \neq \sqrt{2}b$ (so that the tetrahedron is not regular). The orientation-

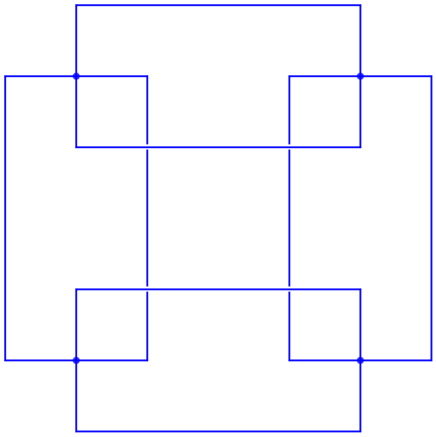

(a) $n = 5,\ g = 5$

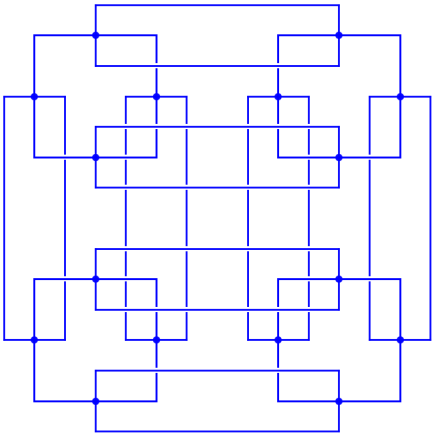

(b) $n = 6,\ g = 17$

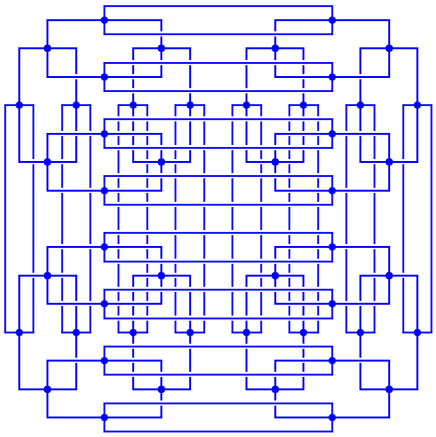

(c) $n = 7,\ g = 49$

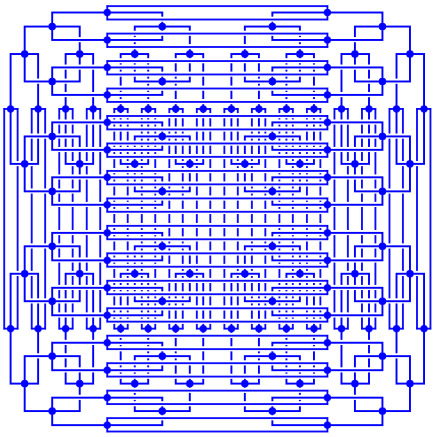

(d) $n = 8,\ g = 129$

Figure 2-2 The line graph corresponding to different values of $n = 5, 6, 7, 8$, and genus $g = (n-4) \cdot 2^{n-3} + 1$

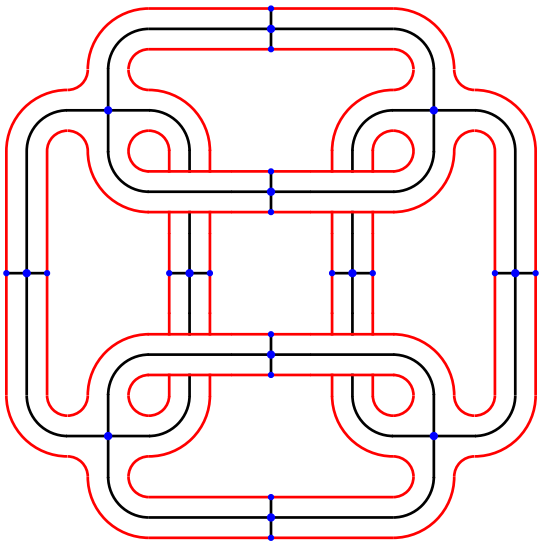

Figure 2-3 The genus $g = 5$ surface corresponding to $n = 5$, together with its systoles, embedded in $\mathbb{R}^3$

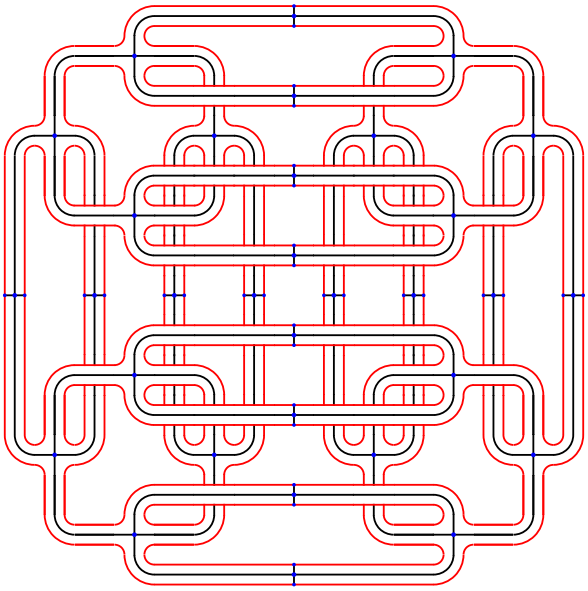

Figure 2-4 The genus $g = 17$ surface corresponding to $n = 6$, together with its systoles, embedded in $\mathbb{R}^3$

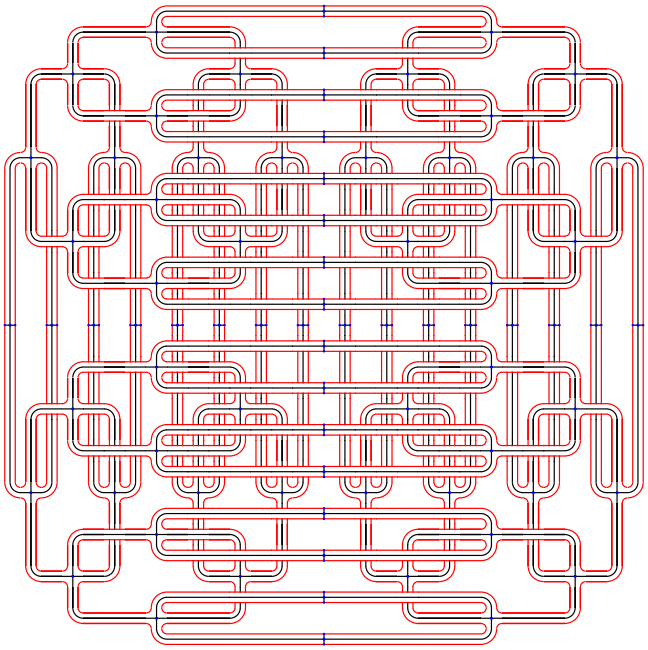

Figure 2-5 The genus $g = 49$ surface corresponding to $n = 7$, together with its systoles, embedded in $\mathbb{R}^3$

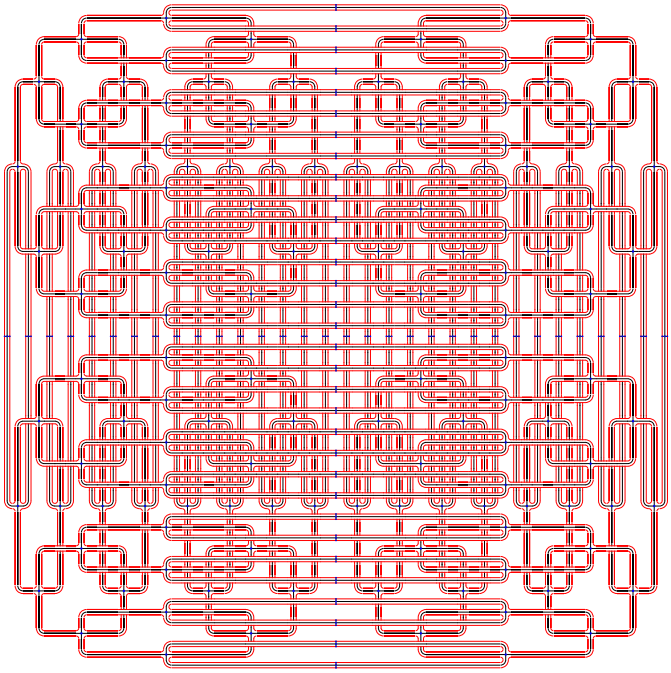

Figure 2-6 The genus $g = 129$ surface corresponding to $n = 8$, together with its systoles, embedded in $\mathbb{R}^3$

preserving rigid symmetry group of this configuration consists of four rotations:

(1)the identity;

(2)a $180°$ rotation about the z-axis, swapping $A \leftrightarrow B$ and $C \leftrightarrow D$;

(3)a $180°$ rotation about the axis $(1, -1, 0)$, swapping $A \leftrightarrow D$ and $B \leftrightarrow C$;

(4)and a $180°$ rotation about the axis $(1, 1, 0)$, swapping $A \leftrightarrow C$ and $B \leftrightarrow D$.

These three nontrivial rotations are pairwise perpendicular, each of order two, and the set is closed under composition, forming an abelian group of order four; hence it is isomorphic to V_4. (If $a = \sqrt{2}b$, the configuration becomes a regular tetrahedron and the symmetry group enlarges; in that degenerate case the symmetry group is isomorphic to A_4.)

Inductive step: Assume the claim holds for some $n \geq 5$. To construct the line graph of size $n + 1$, we first take two copies of the scale n graph, shifting one left and the other right; we can regard these two parts to be new points C' and D'. We then scale all y-coordinates by a factor of 2 and stretch every vertical segment to twice its original length, this operation does not affect the symmetry. Finally, we rotate a copy of the current configuration by $90°$ about the origin (i.e., apply the transformation $(x, y) \mapsto (-y, x)$) and superimpose it onto the original. This yields the configuration of size $n + 1$; the new copies of the stretched graph can be denote the new points A' and B'. Hence the resulting line graph still admits the same four isometries, completing the induction. ■

Remark 2.5: With suitable local fine-tuning of the shape, it is conjectured that this global configuration may yield a good embedding of the surface, possibly providing an example of a Willmore surface.

Let Σ be a smooth surface in $\mathbb{R}^3$. Its Willmore energy is defined as

$$\mathcal{W}(\Sigma) = \int_{\Sigma} H^2 \, dA,$$

where H denotes the mean curvature of the surface and dA is the area element. A surface Σ is called a *Willmore surface* if it is a critical point of the Willmore energy, the first variation of the energy vanishes for all infinitesimal variations preserving the conformal structure.

Equivalently, Willmore surfaces satisfy the corresponding Euler-Lagrange equation:

$$\Delta H + 2H(H^2 - K) = 0,$$

where Δ is the Laplace–Beltrami operator on the surface and K denotes the Gaussian curvature.

Remark 2.6: We note that in our constructed embedding, the edge lengths within each block are not uniform when measured with the standard Euclidean metric. Another idea is to adjust the metric on the three-dimensional space to make every edge length equal, which would also introduce some interesting geometry and metric considerations.

We observe that in regions higher along the z-axis, the horizontal edges become longer while the vertical edges become shorter. Conversely, in lower regions along the z-axis, the folding pattern behaves oppositely. Moreover, the magnitude of this variation grows exponentially with changes in the z-coordinate. Therefore, if we adjust the metric according to the z-coordinate, we can ensure that each edge within every block has roughly the same order of magnitude, that is, they become approximately uniform. Following this approach, we can equip the three-dimensional space with the following metric:

$$ds^2 = e^{2z}dx^2 + e^{-2z}dy^2 + dz^2$$

This metric appears in many other areas of mathematics.

Thurston geometries provide a unified framework for the classification of three-dimensional manifolds. Thurston conjectured, and Perelman later completed the proof using techniques from the Ricci flow in geometric analysis, that any closed 3-manifold can be decomposed into pieces, each admitting one of *eight model geometries*. One of these is **Sol** geometry. The metric $ds^2 = e^{2z}dx^2 + e^{-2z}dy^2 + dz^2$ is the standard model metric for Sol on $\mathbb{R}^3$. Unlike spherical or hyperbolic geometry, Sol is anisotropic: it expands exponentially in the x-direction and contracts exponentially in the y-direction. Consequently, its curvature is neither constant nor isotropic. A canonical example arises from the mapping torus of a two-dimensional torus T^2, where the gluing map is given by a hyperbolic matrix in $SL(2,\mathbb{Z})$; the resulting 3-manifold naturally admits a Sol geometric structure.

In dynamical systems, this metric is intimately related to Anosov systems. More specifically, a hyperbolic automorphism of the torus, given by a matrix $A \in SL(2,\mathbb{Z})$ with $|\mathrm{tr}(A)| > 2$, admits a splitting into stable and unstable directions: one direction contracts exponentially, while the other expands exponentially. When this discrete dynamical system is suspended to a continuous-time flow via its mapping torus, the corresponding geometric model is precisely Sol space. In this formulation, the factors e^z and e^{-z} in the metric encode the exponential growth and decay of the unstable and stable directions, respectively. In this sense, the metric can be interpreted as a geometric realization of Anosov dynamics: it encodes exponential stretching and contracting behavior directly

into the geometry of the space, thereby serving as an important bridge between geometric topology and hyperbolic dynamical systems.

Cellular homology and notion for closed geodesics

The dual complex

$$X^* = Z(C_n, (D^1, S^0))^*$$

is a cell complex whose 2-cells are 2^n many n-gons, whose 1-cells are $n \cdot 2^{n-1}$ edges, and whose 0-cells are $n \cdot 2^{n-2}$ vertices.

The 2-cells of X^* correspond to the vertices of X, that is, to the vertices of Q_n. Hence they can be labeled by elements of the vector space $\mathbb{F}_2^n$, namely by binary sequences

$$(a_1, a_2, \dots, a_n), \qquad a_i \in \mathbb{F}_2,$$

where the indices are understood cyclically modulo n.

We use the same notation for corresponding cells in X and X^*: vertices correspond to 2-cells, and edges correspond to edges. More precisely:

- A 2-cell of X^* corresponds to a vertex of X, and is labeled by its coordinate

$$(a_1, a_2, \dots, a_n).$$

- A 1-cell of X^* corresponds to an edge of X, obtained by changing the i-th coordinate. We introduce the symbol $*$ to indicate that the corresponding entry takes both values 0 and 1. Thus such an edge is denoted by

$$(a_1, \dots, *, \dots, a_n),$$

where the i-th entry is $*$, and all other entries are fixed in $\{0, 1\}$.

- A 0-cell of X^* corresponds to a 2-cell of X. This 2-cell is determined by allowing two adjacent coordinates, say the i-th and $(i+1)$-st, to vary over $\{0, 1\}$, producing four vertices. Accordingly, such a vertex of X^* is denoted by

$$(a_1, \dots, *, *, \dots, a_n),$$

where the i-th and $(i+1)$-st entries are $*$, and all other entries are fixed in $\{0, 1\}$.

The cellular homology of X^* can be computed from its cellular chain complex. For convenience, we work throughout with coefficients in $\mathbb{F}_2$. According to the incidence relations among faces, edges, and vertices, the boundary operators are described as follows.

First, each 2-cell is adjacent to n edges, obtained by replacing one coordinate with

$*$. Therefore,

$$d_2(a_1, a_2, \dots, a_n) = (*, a_2, \dots, a_n) + (a_1, *, a_3, \dots, a_n) + \cdots + (a_1, a_2, \dots, *, a_n) + (a_1, a_2, \dots, a_{n-1}, *).$$

Second, the boundary of each edge consists of the two vertices obtained by replacing the $*$ together with one of its two adjacent positions by $*$. For example,

$$d_1(a_1, *, a_3, \dots, a_n) = (*, *, a_3, \dots, a_n) + (a_1, *, *, \dots, a_n).$$

Hence the cellular chain complex of X^* over $\mathbb{F}_2$ is

$$0 \longrightarrow C_2 \xrightarrow{d_2} C_1 \xrightarrow{d_1} C_0 \longrightarrow 0,$$

that is,

$$0 \longrightarrow \mathbb{F}_2^{2^n} \longrightarrow \mathbb{F}_2^{n\cdot 2^{n-1}} \longrightarrow \mathbb{F}_2^{n\cdot 2^{n-2}} \longrightarrow 0.$$

Moreover, the first homology group is

$$H_1(X^*) \cong \mathbb{Z}^{(n-4)\cdot 2^{n-2}+2}.$$

It is generated by the 1-cells of X^*, and the relations among these generators are exactly those coming from the boundaries of the 2-cells, namely the n-gons.

Next we describe a labeling of the shortest closed geodesics, namely the systoles. Each systole is composed of four edges, which form a square of the following form:

$$(\dots, 0, *, 0, \dots) \to (\dots, 0, *, 1, \dots) \to (\dots, 1, *, 1, \dots) \to (\dots, 1, *, 0, \dots) \to (\dots, 0, *, 0, \dots).$$

After choosing an orientation, equivalently, after fixing the position of the symbol $*$ to be the i-th coordinate, the systole can be labeled by this cyclic sequence of four edges. In this description, the $(i-1)$-st and $(i+1)$-st coordinates vary through the pattern

$$(0,0) \to (0,1) \to (1,1) \to (1,0),$$

while all remaining coordinates are fixed arbitrarily in $\{0, 1\}$.

Accordingly, a systole may be denoted by

$$(a_1, \dots, \star, *, \star, \dots, a_n),$$

where the symbol $*$ indicates the fixed direction of the systole, and the two symbols $\star$ indicate the two adjacent coordinates involved in the above cyclic pattern. The other coordinates a_j are arbitrary elements of $\mathbb{F}_2$. Indeed, there are n possible choices for the position of the distinguished coordinate $*$, and for each such choice, the remaining $n-3$ coordinates can be chosen freely in $\mathbb{F}_2$. Therefore, the total number of distinct systoles is

$n\,2^{n-3}$.

Standard Kernel Bases Construction

Consider the Hurewicz map of the real moment-angle complex $X = Z(C_n; (D^1, S^0))$:

$$h : \pi_k(X) \to H_k(X).$$

Since X is a closed surface of genus g, its homology and homotopy groups are well known: for $k = 1$, h is the abelianization map $\pi_1(X) \to H_1(X)$; for $k \geq 2$, both $\pi_k(X)$ and $H_k(X)$ vanish (except possibly when $n = 3$ and $g = 0$, where $\pi_2(S^2) \cong \mathbb{Z}$ and h is an isomorphism). Thus the Hurewicz map can be completely described by the topology of the surface.

The correspondence between closed geodesics on a hyperbolic Riemannian manifold X and conjugacy classes in its fundamental group $\pi_1(X)$ is well-established. Let S denote the systoles (the set of shortest non-contractible closed geodesics) of X. There exists a natural inclusion $\iota : S \hookrightarrow \mathrm{Conj}(\pi_1(X))$, which maps each systole to its corresponding conjugacy class. Composing ι with the Hurewicz homomorphism $h : \mathrm{Conj}(\pi_1(X)) \to H_1(X)$ yields a morphism embedding the systoles set into the first homology group. By virtue of $H_1(X)$ being abelian and through the universal property of free abelian groups, this morphism extends uniquely to a homomorphism from the free abelian group $\tilde{S} := \mathbb{Z}^S$ generated by S. This relationship is captured in the following commutative diagram:

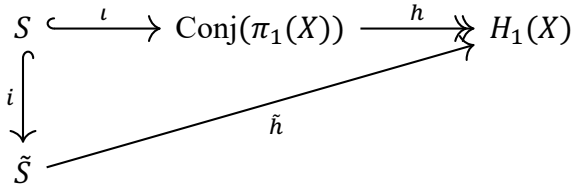

There is a exact sequence:

$$0 \to Ker\ \tilde{h} \to \tilde{S} \xrightarrow{\tilde{h}} H_1 \to Coker\ \tilde{h} \to 0$$

Construction 2.8: We can construct a basis for the intersection space $S \cap B$. This construction leverages combinatorial insights via the independent set structure of circular graphs $C_n = \partial P^n$.

The core framework involves two key maps:

$$\psi_s : I(C_n) \to \tilde{S} \quad \text{and} \quad \psi_f : I(C_n) \to C_2,$$

which are designed to commute with the boundary map d_2. This compatibility is captured by the following commutative diagram:

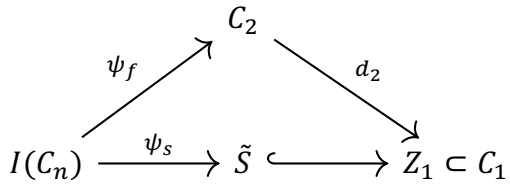

The map ψ_s is constructed by associating each independent set $I \subset [n]$ with a specific linear combination of systoles, while ψ_f maps the same independent set to a corresponding linear combination of faces in the chain complex. The commutativity of the diagram ensures that the image of ψ_s lies within the kernel of d_2, thus providing a systematic way to identify elements in $S \cap B$.

To carry out the construction, one first fixes a vector $v \in \mathbb{F}_2^n$, for instance $v = (1, 1, \dots, 1)$.Different choices of f lead to different bases.

Now let $A \subset [n]$ be a non-empty independent set. The element $\psi_f(A)$ is defined as the linear combination of all 2-cells obtained by fixing the coordinates indexed by A to be 1 (the corresponding element in vector v), while allowing the coordinates indexed by $[n] \setminus A$ to vary freely in $\mathbb{F}_2$. In our notation, this means that for each $i \in A$ the i-th coordinate is replaced by 1, whereas for each $i \notin A$ the i-th coordinate is replaced by $\star$, indicating that one sums over both possible values 0 and 1 of the corresponding free variable.

Applying the boundary map d_2 to $\psi_f(A)$, we obtain $\psi_s(A)$. More explicitly, $\psi_s(A)$ is the sum over all $i \in A$ of the 1-chains in which the i-th coordinate is marked by $*$, the $(i-1)$-st and $(i+1)$-st coordinates are marked by $\star$, and all remaining coordinates vary freely over $\{0, 1\}$. Symbolically, each summand has the form $(\dots, \star, *, \star, \dots)$, with $*$ in the i-th position.

Since A is an independent set, for every $i \in A$ neither $i-1$ nor $i+1$ belongs to A. Therefore, in the expression for $\psi_s(A)$, the coordinates in positions $i-1$ and $i+1$ are indeed free, and hence are labeled by $\star$. This guarantees that every summand in $\psi_s(A)$ is a linear combination of systoles. Consequently,

$$d_2\big(\psi_f(A)\big) = \psi_s(A).$$

Example 2.4: We illustrate two concrete instances of ψ_s and ψ_f for independent set $\{1, 3, 5\} = (\bullet, \circ, \bullet, \circ, \bullet, \circ)$ and $\{1, 4\} = (\bullet, \circ, \circ, \bullet, \circ, \circ)$ on the case $n = 6$.

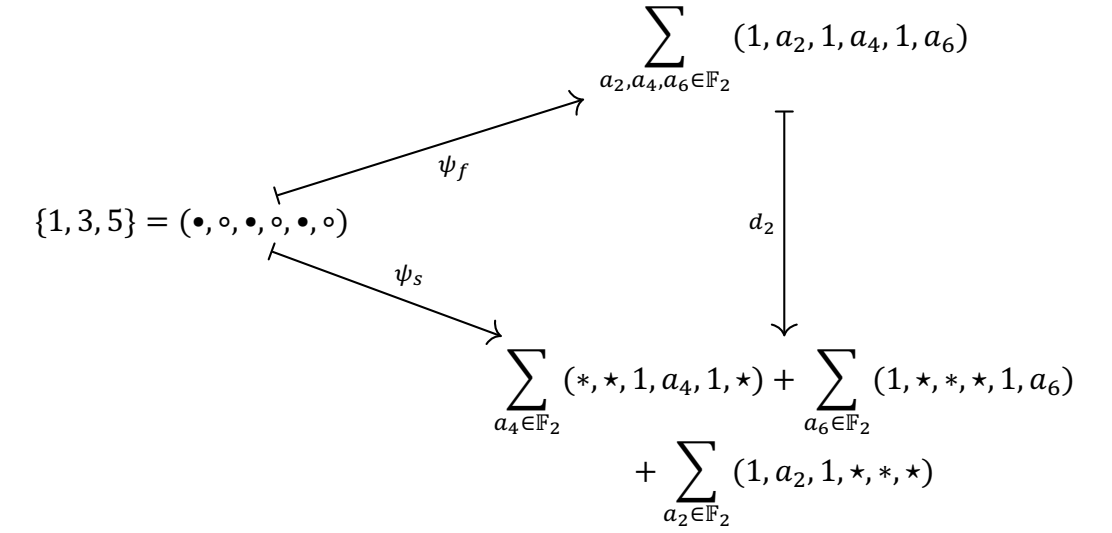

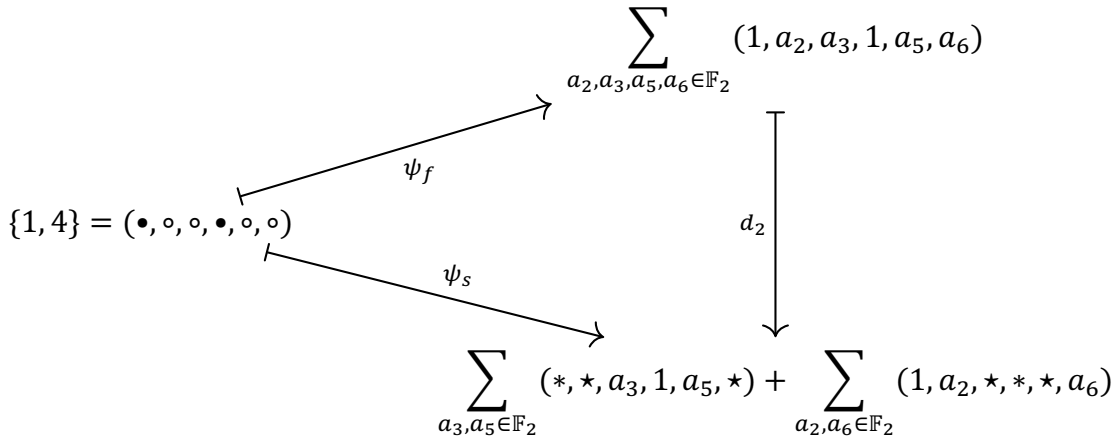

Then we can express the construction for general case as the following commutative diagram:

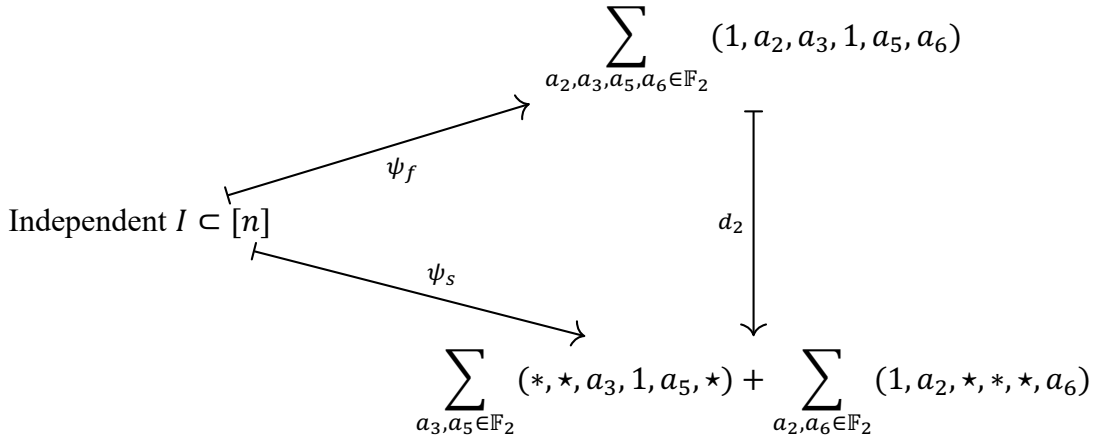

We want to know the rank of systoles in homology group H_1, that is

$$\text{Image } \tilde{h} = \frac{\tilde{S}}{\tilde{S} \cap B_1} = \frac{\tilde{S} + B_1}{B_1}$$

$$\begin{aligned}\dim \text{Image } \tilde{h} &= \dim(\tilde{S}) - \dim(\tilde{S} \cap B_1) \\ &= \dim(\tilde{S} + B_1) - \dim(B_1)\end{aligned}$$

we can easily understand $\tilde{S} \cap B_1$ is exactly the $Ker\ \tilde{h}$.

$$\text{Coker } \tilde{h} = \frac{Z_1}{\tilde{S} + B_1}$$

Theorem 2.10: The image of ψ_s is a basis of $\text{Ker}\,\tilde{h}$.

Proof: To prove the theorem, it suffices to show two things: first, that the elements in $\text{Im}\,\psi_s$ are linearly independent; second, that they span $\text{Ker}\,\tilde{h}$.

We first prove linear independence. Suppose that

$$\alpha = \sum_A c_A\, \psi_s(A) = 0, \qquad c_A \in \mathbb{F}_2,$$

where the sum runs over all non-empty independent sets $A \subset [n]$. Consider

$$\beta := \sum_A c_A\, \psi_f(A) \in C_2(X^*; \mathbb{F}_2).$$

By construction, $d_2(\psi_f(A)) = \psi_s(A)$ for every non-empty independent set A, and hence

$$d_2(\beta) = \sum_A c_A\, d_2(\psi_f(A)) = \sum_A c_A\, \psi_s(A) = \alpha = 0.$$

Therefore $\beta \in \ker d_2$.

Since X^* is a closed connected surface, over $\mathbb{F}_2$ the kernel of d_2 is one-dimensional, generated by the sum of all 2-cells, i.e., $(\star, \dots, \star)$. Thus either $\beta = 0$ or $\beta = (\star, \dots, \star)$.

However, by the definition of $\psi_f(A)$, every term in $\psi_f(A)$ has at least one coordinate fixed to 1, because $A \neq \emptyset$. Hence no linear combination of the $\psi_f(A)$ can equal $(\star, \dots, \star)$, since the latter contains the face $(0, \dots, 0)$, while $(0, \dots, 0)$ never appears in any $\psi_f(A)$. It follows that $\beta = 0$. Since the family $\{\psi_f(A)\}$ is linearly independent, all coefficients c_A must be zero. Therefore the family $\{\psi_s(A)\}$ is linearly independent.

It remains to prove that $\text{Im}\,\psi_s$ spans $\text{Ker}\,\tilde{h}$. Let $\alpha \in \text{Ker}\,\tilde{h}$. Then α is a null-homologous linear combination of systoles, so there exists a 2-chain

$$f \in C_2(X^*; \mathbb{F}_2)$$

such that $\partial f = \alpha$. Since α is a union of closed geodesics, the support of ∂f is a union of closed geodesics.

We now analyze the local form of f around a vertex. Let v be any vertex of X^*. Write the four faces around v in cyclic order as

$$F_0, F_1, F_2, F_3,$$

and denote the four edges between adjacent faces by

$$e_i = F_i \cap F_{i+1}, \qquad i \in \mathbb{Z}/4\mathbb{Z}.$$

Let $a_i \in \mathbb{F}_2$ be the coefficient of F_i in f. Then

$$e_i \subset \partial f \iff a_i + a_{i+1} = 1.$$

Indeed, each edge is adjacent to exactly two faces: if the coefficients on the two sides are equal, the edge cancels in ∂f; if they are different, the edge remains.

Since ∂f is a union of closed geodesics, only the following local configurations can occur at v.

(1) No edge passes through v. In this case $a_0 = a_1 = a_2 = a_3$, so the local pattern is 0000 or 1111.

(2) Exactly two edges pass through v. Since a geodesic must go straight through a vertex, these two edges must be opposite edges. Solving $a_i + a_{i+1} = 1$ shows that the only possible local pattern is 1100 up to cyclic permutation.

(3) All four edges pass through v. Then

$$a_0 + a_1 = a_1 + a_2 = a_2 + a_3 = a_3 + a_0 = 1,$$

which implies

$$a_0 = a_2, \qquad a_1 = a_3, \qquad a_0 \neq a_1.$$

Hence the local pattern is 1010 or 0101.

Therefore only the four local types $0000, 1111, 1100$(up to cyclic permutation),1010 (up to cyclic permutation) can occur at a vertex.

Now consider a vertex of type 1010. Let the four surrounding faces in cyclic order be A, B, C, D, and suppose the local contribution of f is $A + C$, that is, A and C are chosen while B and D are not. Geometrically, ∂f consists of two geodesics crossing at v: one passes through one pair of opposite edges, and the other passes through the other pair.

At each such vertex, we perform a local splitting: we replace the single crossing point by two distinct vertices, so that the two geodesics are separated and no longer intersect at that point. This operation changes only the identification of the vertices; it does not alter

any 2-cell itself. After performing this splitting at every vertex of type 1010, we obtain a new 2-dimensional cell complex, denoted by Σ, together with a natural cellular map

$$p : \Sigma \to X^*,$$

which is the original isometric embedding on each 2-cell. Since no face has been changed, the pushforward of the 2-chain defined by Σ is exactly f.

At a vertex of type 1100, the two chosen faces meet along two right angles, so the total interior angle is $\frac{\pi}{2} + \frac{\pi}{2} = \pi$, and hence the boundary passes straight through that point, with no right-angled turn. At a split vertex coming from a former 1010 crossing, each branch still follows the original geodesic, so again there is no right-angled turn. Therefore every boundary component of Σ maps to a closed geodesic in X^*, and no boundary component has a right-angled corner at a vertex.

Now decompose Σ into connected components:

$$\Sigma = \Sigma_1 \sqcup \cdots \sqcup \Sigma_m.$$

Let

$$f_i := p_*([\Sigma_i]) \in C_2(X^*; \mathbb{F}_2).$$

Since addition over $\mathbb{F}_2$ is symmetric difference and Σ is the disjoint union of the Σ_i, we have

$$f = f_1 + \cdots + f_m.$$

Moreover, each f_i is represented by a compact surface Σ_i with boundary, and the boundary of Σ_i maps to a union of closed geodesics in X^* without right-angled turns.

For each connected component Σ_i, its boundary is a disjoint union of closed geodesics. Hence the directions corresponding to the symbols $*$ in ∂f_i must form an independent set; otherwise two adjacent directions would create a local configuration of type 1010, contradicting the fact that all such crossings were separated in the construction of Σ.

It remains to show that each such f_i can be written as a linear combination of the standard generators $\psi_f(A)$. For this we use the elementary identity over $\mathbb{F}_2$:

$$(\dots, \star, 1, \star, \dots) + (\dots, \star, 0, \star, \dots) = (\dots, \star, \star, \star, \dots).$$

Equivalently,

$$(\dots, \star, 0, \star, \dots) = (\dots, \star, 1, \star, \dots) + (\dots, \star, \star, \star, \dots).$$

Thus whenever a local term contains a coordinate fixed to 0, we may replace it by a sum of a term with that coordinate fixed to 1 and a term with fewer fixed coordinates. Repeating this procedure, every f_i can be written as a linear combination of chains of the form $\psi_f(A)$, where A is a non-empty independent set.

Applying d_2 to such an expression and using

$$d_2(\psi_f(A)) = \psi_s(A),$$

we conclude that

$$\partial f_i \in \text{span}(\text{Im}\,\psi_s)$$

for every i. Therefore,

$$\alpha = \partial f = \partial f_1 + \cdots + \partial f_m \in \text{span}(\text{Im}\,\psi_s).$$

This proves that $\text{Im}\,\psi_s$ spans $\text{Ker}\,\tilde{h}$.

Combining linear independence and spanning, we conclude that $\text{Im}\,\psi_s$ is a basis of $\text{Ker}\,\tilde{h}$. ■

Corollary 2.2: By the enumeration formula, we can determine the ranks of the free abelian groups:

$$\text{rank Ker}\,\tilde{h} = L(n) - 1,$$

$$\text{rank Im}\,\tilde{h} = n \cdot 2^{n-3} - L(n) + 1.$$

Proof: The exact sequence and its rank of each terms is displays as following:

$$\begin{array}{ccccccccc} 0 & \to & \text{Ker}\,\tilde{h} & \to & \tilde{S}(X) & \xrightarrow{\tilde{h}} & H_1(X) & \to & \text{Coker}\,\tilde{h} & \to & 0 \\ 0 & \to & \mathbb{F}_2^{L_n-1} & \to & \mathbb{F}_2^{n\cdot 2^{n-3}} & \to & \mathbb{F}_2^{2((n-4)2^{n-3}+1)} & \to & \mathbb{F}_2^{(n-8)2^{n-3}+L_n+1} & \to & 0 \end{array}$$

■

Combinatorial identities

Similar to the previous Theorem 2.4 (Proposition 3.5.10 in Al-Raisi[65]), by counting the number of orbits of a given set under the action of a cyclic group using different methods, we obtain another identity relating the Möbius function and the Euler totient function.

The cyclic group C_n acts naturally on both the set of systoles $\tilde{S}$ and the first homology group $H_1(X_n)$. Moreover, the map $\tilde{h} : \tilde{S} \to H_1(X_n)$ is equivariant with respect to this action. Consequently, C_n also acts on the kernel of $\tilde{h}$, giving rise to the following short

exact sequence of $\mathbb{Z}[\mathbb{Z}/n]$-modules:

$$0 \longrightarrow \operatorname{Ker} \tilde{h} \longrightarrow \tilde{S} \longrightarrow H_1(X_n).$$

Theorem 2.11: For $n \geq 4$, there is an identity

$$\frac{1}{n}\left(\sum_{d|n} \mu(d) L\left(\frac{n}{d}\right)\right) + \sum_{\substack{d|n \\ 1<d<n}} \left(\frac{1}{d} \sum_{d_1|d} \mu(d_1) L\left(\frac{d}{d_1}\right)\right) = \frac{1}{n}\left(\sum_{d|n} \phi(d) L\left(\frac{n}{d}\right)\right) - 1,$$

relating the Möbius inversion function, the Euler totient function and the Lucas numbers by equating the two different orbit counting methods of the systoles.

Proof: The action of $\mathbb{Z}/n$ acts equivariantly on the free abelian group generated by the mapping systole set, mapping to the Hurewicz map of the cohomology class, so it must act on the kernel of this map. The way it acts is still by rotating the cycle graph C_n, and thus it acts on the non-empty independent sets. That is to say, it acts naturally on the standard basis we have given. We then count the orbits of this group action in two different ways to obtain such an identity. One method is to use Burnside's lemma for the calculation, which gives the right-hand side of the identity. The other method is to directly count the aperiodic independent sets, which gives the left-hand side of the identity.

By Theorem 2.12 and Theorem 2.13 we can get identity:

$$\frac{1}{n}\left(\sum_{d|n} \mu(d) L\left(\frac{n}{d}\right)\right) + \sum_{\substack{d|n \\ 1<d<n}} \left(\frac{1}{d} \sum_{d_1|d} \mu(d_1) L\left(\frac{d}{d_1}\right)\right) = \frac{1}{n}\left(\sum_{d|n} \phi(d) \left(L\left(\frac{n}{d}\right) - 1\right)\right).$$

The last -1 term can be collected using the formula $\sum_{d|n} \phi(d) = n$. ■

Theorem 2.12: Let C_n be the cycle graph with n vertices ($n \geq 3$). The number of orbits of all non-empty independent sets of C_n under the action of the cyclic group $\mathbb{Z}/n$ (by rotations) is given by

$$N = \frac{1}{n} \sum_{d|n} \varphi(d) \left(L\left(\frac{n}{d}\right) - 1\right),$$

where $L(m) = L_m$ is the Lucas number, defined as $L_m = F_{m-1} + F_{m+1}$ (with F_m the Fibonacci numbers, $F_0 = 0$, $F_1 = 1$), and φ is Euler's totient function.

Proof: By Burnside's lemma, the number of orbits equals the average number of fixed points under the group action, i.e.,

$$N = \frac{1}{n} \sum_{k=0}^{n-1} \operatorname{Fix}(k),$$

where $\operatorname{Fix}(k)$ denotes the number of non-empty independent sets that are invariant under

a rotation by k steps.

For a given rotation by k, let $d = \gcd(n, k)$. This rotation partitions the vertex set into d orbits, each of length n/d. An independent set S is invariant under this rotation if and only if S consists of a union of whole orbits, and these orbits (viewed as vertices of the induced cycle graph C_d) form an independent set in C_d (since vertices from adjacent orbits are adjacent in the original graph). Therefore, the number of such S (including the empty set) equals the number of all independent sets of the cycle graph C_d. It is well known that the number of independent sets of the cycle graph C_m is the Lucas number $L_m = F_{m-1} + F_{m+1}$. Hence, the number of independent sets (including empty) invariant under this rotation is L_d, and consequently the number of non-empty invariant sets is $L_d - 1$, i.e., $\mathrm{Fix}(k) = L_d - 1$.

Now we group the values of k by their greatest common divisor with n: for each divisor d of n, the number of k such that $\gcd(n, k) = d$ is $\varphi(n/d)$ (with the convention that $\varphi(1) = 1$ corresponds to $k = 0$ when $d = n$). Thus,

$$\sum_{k=0}^{n-1} (L_{\gcd(n,k)} - 1) = \sum_{d|n} \varphi\left(\frac{n}{d}\right)(L_d - 1).$$

Substituting into Burnside's formula yields

$$N = \frac{1}{n}\sum_{d|n} \varphi\left(\frac{n}{d}\right)(L_d - 1) = \frac{1}{n}\sum_{d|n} \varphi(d)(L_{n/d} - 1).$$

This completes the proof. ■

Theorem 2.13: Let C_n be the cycle graph on $n \geq 3$ vertices. Consider binary necklaces of length n, up to cyclic rotation, where the vertices colored 1 form an independent set of C_n. Equivalently, these are cyclic binary words of length n with no two consecutive 1's, including the first and last positions.

Then the number of aperiodic (equivalently, primitive) such necklaces with the 1-set nonempty is

$$N = \frac{1}{n}\sum_{d|n} \mu(d)\, L_{n/d}$$

where μ is the Möbius function and $L_m = L(m)$ is the m-th Lucas number.

Proof: Let $A(n)$ be the number of cyclic binary words of length n in which no two 1's are adjacent (cyclically). This is exactly the number of independent sets of the cycle graph C_n, and it is well known that

$$A(n) = L_n.$$

Now let $P(n)$ denote the number of such cyclic words that are primitive, i.e., whose least period is exactly n. Every admissible cyclic word has a unique least period $d \mid n$, and it is obtained by repeating a primitive admissible cyclic word of length d exactly n/d times. Hence

$$A(n) = \sum_{d|n} P(d).$$

Applying Möbius inversion gives

$$P(n) = \sum_{d|n} \mu(d)\, A(n/d) = \sum_{d|n} \mu(d)\, L_{n/d}.$$

Each primitive necklace has exactly n distinct rotations, so the number N_n of primitive necklaces is

$$N = \frac{P(n)}{n} = \frac{1}{n} \sum_{d|n} \mu(d)\, L_{n/d}.$$

Finally, the condition that the 1-set be nonempty does not change the count: the only admissible necklace with empty 1-set is $00\cdots0$, which has period 1 and is therefore not primitive for $n \geq 3$. Thus the same formula counts primitive necklaces whose 1-set is a nonempty independent set. ■

2.5 Generalization and Future Work

The following questions and directions remain open for further investigation.

We aim to determine whether the cokernel group contains any torsion elements. This can be approached computationally using Smith normal form decomposition. Beyond computation, we seek to understand the geometric and homotopy-theoretic implications of such torsion.

We intend to write down the explicit edges corresponding to each homology class (using the stable decomposition theorem) and then compare them directly with the edges representing geodesics. This comparison may reveal deeper relationships between combinatorial cycles and minimal length representatives.

The maximum independent set cuts the surface into certain basic pieces, suggesting the possibility of a natural Fenchel-Nielsen coordinate system. Currently, there is no canonical pants decomposition that respects the cell structure—any decomposition into a union of pants would necessarily destroy the existing cell decomposition. We hope to find a more suitable coordinate system for Teichmüller space that uses fewer parameters

and is more natural than the current approach based on edge lengths and angles.

Our current work focuses on the systole function (the shortest closed geodesic). In the future, we can study geodesics of arbitrary length. Due to the nature of hyperbolic geometry, as the length grows, the multiplicity of geodesics becomes unbounded. This allows us to introduce a filtration by geodesic length and investigate how the size of the kernel of the Hurewicz map varies as the length increases. This would provide a more refined understanding of the relationship between topology and geometry.

For infinite-type surfaces (those with infinite genus or infinitely many ends), the mapping class group often called a big mapping class group, it has become a distinct area of study. Research has shifted from the discrete, finitely generated groups of the finite-type case to non-locally compact, typically uncountable Polish groups, together with their actions on arc graphs, Teichmüller spaces, and newly developed "marked" moduli spaces. Recent progress focuses on large-scale geometry, continuity and rigidity phenomena, classification up to isomorphism, and topological-dynamical properties such as Rokhlin-type behavior and amenability, as well as on constructing appropriate moduli space frameworks for infinite-type surfaces. For instance, recent surveys have established the field as an independent direction; Mann-Rafi study their coarse geometry; and Tappu introduces moduli spaces of marked Nielsen-convex hyperbolic structures adapted to the infinite-type setting, proving continuity of the mapping class group action. This line of research is important because infinite-type surfaces form a natural boundary of classical Teichmüller and moduli space theory, yet exhibit fundamentally new group-theoretic and dynamical phenomena; at the same time, they connect low-dimensional topology, geometric group theory, complex analysis, and moduli theory, and challenge the classical principle that a surface is determined by its symmetries in a non-compact, infinitely complex setting.

The family $Z(C_n, (D^1, S^0))^*$, in the limit $n \to \infty$, suggests a new class of infinite-type surfaces with ends whose topology is more complicated than the standard examples such as the Loch Ness monster surface, Jacob's ladder surface, and the blooming Cantor tree surface. Since its automorphism group contains an infinite cyclic subgroup, the surface carries a nontrivial recurring symmetry that may influence its mapping class group, its end space, and the corresponding moduli-theoretic structure. This makes it a natural object to incorporate into the broader program of studying big mapping class groups and moduli spaces of infinite-type surfaces, especially as a candidate example where classical intuition from known infinite-type surfaces may no longer suffice.

CHAPTER 3 REGULAR MAP THEORY

3.1 Topological Graph Theory

The inquiry of graphs on surfaces is a relatively young branch of mathematics, commonly known as topological graph theory[73]. Although this discipline truly took shape in modern times, its intellectual origins can be traced back to the 19th century, or even earlier[33,56]. It is generally acknowledged that Heawood's research on Map Coloring Problems laid the modern foundation for this field[35,68]. However, from a broader historical perspective, its roots extend even further back: for instance, Kepler[48] studied highly symmetric polyhedra and attempted to use these "perfect solids" to explain the hierarchical relationships between planetary orbits; similarly, Plato and his school showed profound interest in the five regular polyhedra later known as the Platonic solids[21]. In fact, regular maps, as one of the central objects in topological graph theory, can be viewed as a natural generalization of the Platonic solids to arbitrary surfaces[45].

Topological graph theory as we now understand it took shape largely from the study of map coloring problems in the 19th century[35,47]. Its landmark beginning is often identified with the Four Color Conjecture posed in 1852: Can every planar map be colored using only four colors so that adjacent regions differ in color? This deceptively simple combinatorial question profoundly revealed the deep connections between graph structures and the topological properties of surfaces. Mathematicians soon realized that map coloring could be reformulated in terms of vertex coloring of planar graphs[51], thereby integrating it into the broader framework of graph theory.

As research progressed, it became clear that core questions, such as planarity testing and the embeddability of graphs on surfaces, were tied not only to combinatorial graph structure but also to the topological classification of surfaces (such as sphere, torus, double torus, etc.)[33,56]. The field matured rapidly in the mid-20th century alongside advances in topology and discrete mathematics. A major milestone came in 1976 with the computer-assisted proof of the Four Color Theorem[3-4,69], which served as a powerful catalyst for the development of topological graph theory. The graph minor theory pioneered by Robertson and Seymour in the late 20th century provided a profound finite characterization for surface embeddings, elevating topological graph theory to a central position in

modern graph theory[70]. These achievements helped systematically establish important subfields such as graph embedding theory, surface coloring formulas, and graph minor theory, shaping the discipline into its modern form.

The background of topological graph theory is inseparable from the fusion of two major branches of mathematics: on the one hand, graph theory provides discrete, combinatorial models; on the other hand, topology offers continuous, spatial theoretical tools. The core motivation for this intersection stems from the mathematical abstraction of the fundamental act of "drawing map"—how to depict network structures on surfaces without crossings. From circuit board wiring in engineering to network embedding in theoretical computer science, and further to knot theory in low-dimensional topology, this fundamental problem has given rise to a rich research system.

Regular Maps and Symmetry of surfaces

Regular maps are the most symmetric objects in classical map theory: a map is an embedding of a graph on a closed surface such that faces are topological discs, and it is regular when its automorphism group acts transitively on flags, which are incident vertex-edge-face triples. Equivalently, a regular map can be encoded by a highly symmetric permutation description (often via triangle groups), making the subject a meeting point of combinatorics, group theory, and surface topology. Standard foundational treatments develop the flag-transitivity viewpoint, the group-theoretic presentations, and the classification/programs for families of regular maps[45,75]. For a broader perspective emphasizing highly symmetric and related map classes and modern developments, see[73].

Dessins d'Enfants ("children's drawings") are combinatorial objects—typically connected bipartite graphs embedded on an oriented surface—that encode rich geometric and arithmetic data. Concretely, a dessin can be viewed as a map (a graph embedded so that faces are simply connected) with vertices colored black/white, and it corresponds to a holomorphic branched covering of the Riemann sphere ramified only over $\{0, 1, \infty\}$, i.e. a Belyi map[42-44]. By Belyi's theorem, a compact Riemann surface admits such a map iff it can be defined over $\overline{\mathbb{Q}}$; thus dessins form a bridge between Riemann surfaces and number fields, and they admit a natural action of $\mathrm{Gal}(\overline{\mathbb{Q}}/\mathbb{Q})$, an idea emphasized by Grothendieck following Belyi's insights[42,46].

Because dessins sit simultaneously in topology as embedded graphs, complex analysis (branched covers), and arithmetic geometry (fields of definition and Galois action), they connect to areas far beyond group theory—such as hyperbolic geometry and the uni-

formization of surfaces, the theory of Riemann surfaces, and surprisingly directly to Galois theory and arithmetic invariants[31,46]. For approachable treatments and useful viewpoints, see elementary introductions and surveys[34] as well as broader accounts focusing on Belyi maps, bipartite structures, and map-theoretic techniques[42-44]. Recent work also explores extensions beyond the classical compact setting, including non-compact surface generalizations[6].

3.2 Fixed Graph Embedding

Biggs[14] discovered all constructions of orientably regular embeddings of complete graphs in 1971, and James and Jones[41] later in 1985 proved that this list is complete, thereby completing the classification.

Catalano, Conder, Du, Kwon, Nedela, and Wilson[19] provided a complete classification of orientably regular embeddings of the n-dimensional binary hypercubes Q_n. Research in this direction began with the work of Nedela and Škoviera[61], who, for every $n \geq 3$, constructed a covering map family of $\varphi(n)$ non-isomorphic orientably regular embeddings of Q_n by lifting the regular orientable embeddings of n-dipoles, where φ denotes Euler's totient function.Dipoles are graphs consisting of two vertices joined by n parallel edges, whose regular embeddings were classified by Nedela and Škoviera[60]. In that classification, each solution e of the congruence $e^2 \equiv 1 \pmod{n}$ yields a distinct regular map, and different solutions correspond to non-isomorphic embeddings. They conjectured that this lifting construction exhausts all orientably regular embeddings of Q_n. Later, Du, Kwak, and Nedela[26] proved that for odd n, this is indeed the case.

Subsequently, Kwon[52] discovered new families of orientably regular embeddings for all even $n \geq 6$ by applying a switch operator, and Xu[76] established that for $n \equiv 2 \pmod 4$, Kwon's embeddings are the only additional ones beyond those from the covering construction. Further new embeddings were later constructed by Catalano and Nedela[20], who provided a characterization of all orientably-regular embeddings of Q_n in terms of certain quadrilateral identities, and introduced a construction for new regular embeddings of Q_n for all n divisible by 16, not covered by the family of embeddings previously found by Kwon. The full classification was ultimately completed by the comprehensive work of Catalano Conder, Du, Kwon, Nedela, and Wilson[19], which settled all remaining cases.

Additionally, it was shown by Kwon and Nedela[53] that for $n \geq 3$, the n-cube admits

no regular embeddings on non-orientable surfaces.

NS construction

We have achieved a comprehensive grasp of the NS construction, which establishes a framework for classifying regular embeddings of the hypercube graph Q_n by first analyzing the dipole graph D_n . The methodology begins with a canonical projection from Q_n to D_n, followed by a complete classification of all regular embeddings of the simpler graph D_n. These embeddings are then systematically lifted to classify the regular embeddings of Q_n itself.

The next step involves a two-stage explicit demonstration: first, presenting the embedding $D(3,1)$ of the dipole graph D_3 in the torus T^2 , and then showing how this embedding lifts to yield the corresponding embedding $M(3,1)$ of the hypercube graph Q_3 on the torus T^2.

The regular embedding $D(3,1)$ of the cube graph D_3 on the torus T^2 is illustrated in Figure 3-1 .

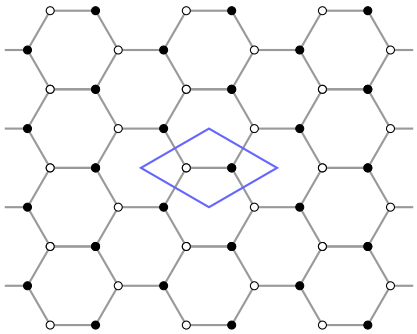

Figure 3-1 The regular embedding $D(3,1)$ of the cube graph D_3 on the torus T^2

The embedding $M(3,1)$ of the cube graph Q_3 on the torus T^2 .

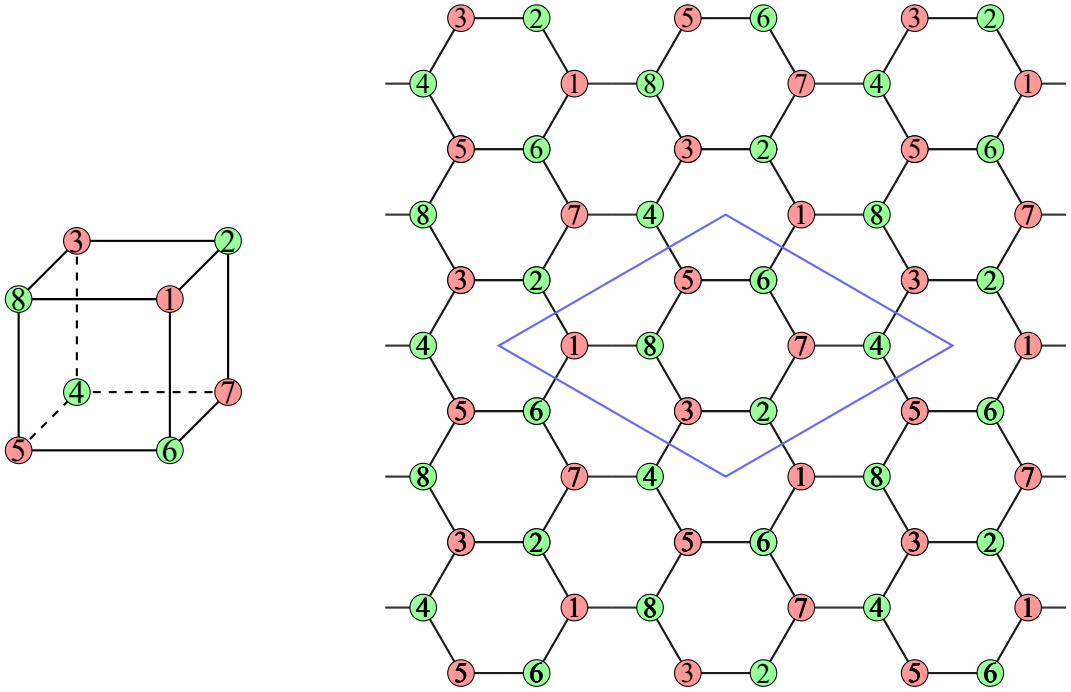

3.3 Homological Redundancy of Geodesics in Regular Maps

3.3.1 General Constructions

Through our study in the crossroad of regular map theory in topological graph theory and hyperbolic geometric, we could found that the problem of counting the homological rank of systoles can be generalized to a broader context. The geometric objects we have studied specifically in the second section is the regular embedding maps of hypercube graphs with minimal genus represent a special case of this broader framework.

Combinatorialists have already classified all regular embeddings of hypercube graphs in an elegant list. More importantly, all these embeddings consist of even polygons as faces. This allows us to pose the same question for their dual maps and compute the homological rank of the cycles formed by their edges. If desired, we may also endow these maps with a standard hyperbolic structure so that all cycles become geodesics—though it should be noted that in this setting, they may not necessarily be the shortest geodesics.

Conversely, the regular embeddings of hypercube graphs themselves can be studied in a similar manner. We may investigate the homological relations among their edges as the dual graph. This case is more complex, as it requires distinguishing between odd and even cases. Only in the even case can all edges of the hypercube graph form closed cycles on the surface. In the odd case, we must also consider the principal diagonals of the faces. Even in the even case, we may further study cycles formed by these principal diagonals.

Furthermore, we can enrich these topological questions with additional geometric structure. While regular maps inherently define a compact topological 2-manifold, we may endow each 2-cell with a standard hyperbolic structure modeled on a right-angled polygon. By assembling these pieces consistently, we obtain a globally hyperbolic structure on the underlying topological surface. This construction yields a distinguished point in the corresponding Teichmüller space. After analyzing the homological behavior of the edge-sets of the graph, we may then study the local geometry of hyperbolic structures around this point. Analogously, the same procedure can be carried out and analogous questions asked for the dual map of the embedding. These topics will be developed in the next chapter.

3.3.2 Calculation of Hypercube Graphs

Proposition 3.1: Table 3-1 presents the computed results of the homological rank and kernel dimension of the regular embeddings of hypercube graphs Q_n for even values of n.

Table 3-1 Homological ranks of edge geodesics in the regular embedding $M(n,-1)$ for $n = 2k$ (even).

k	$n = 2k$	face dim	dim H_1	Geo num	Ker dim	rank in H_1
2	4	15	2	8	6	2
3	6	95	34	48	24	24
4	8	511	258	256	96	160
5	10	2559	1538	1280	400	880
6	12	12287	8194	6144	1732	4412
7	14	57343	40962	28672	7644	21028
8	16	262143	196610	131072	33920	97152
9	18	1179647	917506	589824	150240	439584

Abbreviations: “face dim” denotes the dimension of two dimensional cellular chain. “Geo num” denotes the number of closed geodesics formed by edges; “Ker dim” denotes the dimension of the kernel of the Hurewicz map.

Remark 3.1: Given that the problem scales beyond exponential growth, the computational time grows accordingly. On a personal computer, this essentially represents the practical limit. For instance, the case of $k = 9$ required a full week of computation, which we consider to be the maximum feasible in terms of both computational cost and acceptable runtime under our current programming setup. Alternatively, one may seek to

derive the results directly from mathematical theory by providing formulas and proofs.

While analyzing the accumulated data, we can observed a pattern: the ratio of kernel dimensions to the number of geodesics tends toward $\frac{1}{4}$, and the convergence appears to follow an exponential trend. To investigate further, one can subtract $\frac{1}{4}$ from the ratio and compared the difference with $\frac{1}{2^k}$. Interestingly, the first four values align perfectly with an exponential decay of the form $\frac{1}{2^k}$. However, the subsequent four terms deviate slightly, exceeding the expected $\frac{1}{2^k}$ values.

Fortunately, the deviation for the latter terms can be characterized using triangular numbers with a denominator of 48. We have recorded this finding here in Table 3-2. We are now awaiting additional computational results to verify the consistency of this pattern. Although the expression is not as elegant as those encountered in the dual graph case, it appears to capture the observed behavior.

$$\dim \mathrm{Ker}_n = n \cdot 2^{n-3} \cdot \left(\frac{1}{4} + \frac{1}{2^{\frac{n}{2}-1}} \cdot \left(1 + \frac{\theta_n}{48} \right) \right)$$

where

$$\theta_n = \begin{cases} 0, & 4 \le n < 8 \\ \frac{1}{2}\left(\frac{n}{2}-4\right)\left(\frac{n}{2}-5\right), & 8 \le n \le 18 \end{cases}$$

Table 3-2 The ratio pattern result of edge geodesics in the regular embedding $M(n,-1)$, for $n = 2k$ even

k	$n = 2k$	$\dim H_1$	Geo num	Ker dim	$\frac{\text{Ker dim}}{\text{Geo num}}$	ratio pattern
2	4	2	8	6	0.75	$\frac{3}{4} = \frac{1}{4} + \frac{1}{2}$
3	6	34	48	24	0.5	$\frac{1}{2} = \frac{1}{4} + \frac{1}{4}$
4	8	258	256	96	0.375	$\frac{3}{8} = \frac{1}{4} + \frac{1}{8}$
5	10	1538	1280	400	0.3125	$\frac{5}{16} = \frac{1}{4} + \frac{1}{16}$
6	12	8194	6144	1732	0.281901042	$\frac{433}{1536} = \frac{1}{4} + \frac{1}{32} \cdot \frac{49}{48}$
7	14	40962	28672	7644	0.266601563	$\frac{273}{1024} = \frac{1}{4} + \frac{1}{64} \cdot \frac{17}{16}$
8	16	196610	131072	33920	0.258789063	$\frac{265}{1024} = \frac{1}{4} + \frac{1}{128} \cdot \frac{9}{8}$
9	18	917506	589824	150240	0.254720052	$\frac{1565}{6144} = \frac{1}{4} + \frac{1}{256} \cdot \frac{29}{24}$

Conjecture 3.1: Based on this empirical evidence, we propose the following closed-form expression for the kernel dimension for all even n:

$$\dim \mathrm{Ker}_n = n \cdot 2^{n-3}\left(\frac{1}{4} + \frac{1}{2^{\frac{n}{2}-1}}\left(1 + \frac{\theta_n}{48}\right)\right),$$

where

$$\theta_n = \begin{cases} 0, & n < 8 \\ \frac{1}{2}\left(\frac{n}{2} - 4\right)\left(\frac{n}{2} - 5\right), & n \geq 8. \end{cases}$$

Note that θ_n vanishes for $n = 8$ and 10 as well, so the correction only becomes active for $n \geq 12$. Although the formula is less elegant than the one obtained for the dual graph case, it captures the observed behaviour accurately. Further computational results are awaited to confirm the pattern for larger n.

Through extensive computational experiments, we observe that all geodesic paths in the dual maps are composed of either 2 or 4 edges.

An embedding is algebraically characterized by a triple (D, R, L), where D is the set of darts, R is a rotation action of order n, and L is an involution (of order 2) that reverses dart direction. The action of L is straightforward to understand. Therefore, once the rotation R is fully described by its explicit permutation action, we can derive an algorithm to construct the cellular chain complex. Within this framework, closed geodesics can be identified as specific elements, and their behavior in homology can be computed. The entire construction is elucidated by analyzing the interplay of these two actions.

To operationalize this approach, we proceed in two stages:

（1）**Face Boundaries in the Dual Map:** First we need to find the edges of every face in the dual map. Each face f^* in the dual map corresponds to a vertex v in the original hypercube graph Q_n. The boundary of f^* exactly consists of dual edges e^* corresponding to the edges e incident to v in Q_n. These dual edges can be collected by the orbit of the rotation action R. By assigning appropriate signs to these edges, we obtain a generator that spans the boundary subgroup within the chain complex.

（2）**Geodesic Assembly from Edges:** Then we need know which edges compose a geodesic in the dual map, In the dual map, two edges e_1^* and e_2^* are consecutive in a geodesic if and only if their corresponding original edges e_1 and e_2 are opposite sides of a common face f in the original map. The number of sides of a face, denoted $2m$, is given by the formula $\frac{4n}{\gcd(e+1,n)}$ for $1 < e < n-1$, with special cases $4n$ for $e = 1$ and 4 for $e = -1$. Let d_1 and d_2 be darts on e_1 and e_2, respectively, oriented consistently of the second coordination value. The dart d_2 is obtained from d_1 by applying the composition

$L \circ R$ exactly m times (to traverse half the face perimeter), followed by a final L to correct the orientation. This defines a new operator $A = L \circ (L \circ R)^m$. The orbit of any dart under A traces a sequence of edges that form a geodesic in the dual map.

Computational investigations into specific linear families reveal distinct and consistent patterns regarding the geometry of faces – specifically, the number of edges per face and the dynamical period of the operator A.

For the family parametrized by $(4k, 2k-1)$, each face is found to have a fixed number of 8 edges. The period of the operator A depends on the parameter k: it is 4 for $k \geq 2$, but reduces to 2 for the fundamental case for $k = 1$, which corresponds to the fundamental family $(n, 1)$.

In contrast, the family $(4k, 2k+1)$ exhibits a more complex dependence on k. The number of edges per face is $4k$ when k is odd and $8k$ when k is even. Despite this variability in face geometry, the period of A still follows a clear pattern: it is 4 when k is odd and 2 when k is even.

A distinct pattern emerges for the pair of families $(3(3k+2), 3k+1)$ and $(3(3k-2), -(3k-1))$. In both cases, the number of edges per face is consistently 12, and the period of A is uniformly 4. Similarly, for the families $(5(5k+2), 5k+1)$ and $(5(5k-2), -(5k-1))$, the number of edges per face is fixed at 20, with the period of A again being a constant 4.

Finally, for the families $(3(3k+2), -(3k+1))$ and $(3(3k-2), 3k-1)$, the face geometry is parity-dependent. The number of edges per face is $\frac{2}{3}n$ when k is even and $\frac{4}{3}n$ when k is odd. Notably, despite this variation, the period of the operator A remains constant at 4 across all values of k. This pattern extends to the analogous families $(5(5k+2), -(5k+1))$ and $(5(5k-2), 5k-1)$, where the number of edges per face is $\frac{2}{5}n$ for even k and $\frac{4}{5}n$ for odd k, while the period of A is consistently 4.

Extensive computational experiments reveal distinct patterns in the face geometry (number of edges per face) and the dynamical period of the operator A across several linear families. The results are summarized in Table 3-3.

Table 3-3 Properties of special linear families $M(n, e)$

Family	**Face Edges**	**Period of** A
$(4k,\ 2k-1)$	Fixed: 8	4 ($k \geq 2$) 2 ($k = 1$)
$(4k,\ 2k+1)$	$4k$ (k odd) $8k$ (k even)	4 (k odd) 2 (k even)
$(3(3k+2),\ 3k+1)$ $(3(3k-2),\ -(3k-1))$	Fixed: 12	4
$(3(3k+2),\ -(3k+1))$ $(3(3k-2),\ 3k-1)$	$\frac{2}{3}n$ (k even) $\frac{4}{3}n$ (k odd)	4
$(5(5k+2),\ 5k+1)$ $(5(5k-2),\ -(5k-1))$	Fixed: 20	4
$(5(5k+2),\ -(5k+1))$ $(5(5k-2),\ 5k-1)$	$\frac{2}{5}n$ (k even) $\frac{4}{5}n$ (k odd)	4

CHAPTER 4 GEOMETRIC STRUCTURES OF HYPERBOLIC SURFACES

4.1 Hyperbolic Structures on Surfaces

The Poincaré model of the hyperbolic plane is the upper half-plane of complex numbers, denoted by $\mathbb{H} = \{z \in \mathbb{C} \mid \mathrm{Im}(z) > 0\}$, equipped with the hyperbolic metric:

$$ds^2 = \frac{1}{y^2}(dx^2 + dy^2)$$

The distance formula in this model is given by:

$$\cosh\left(\mathrm{dist}(z, w)\right) = 1 + \frac{2|z - w|^2}{\mathrm{Im}(z) \cdot \mathrm{Im}(w)}$$

where cosh denotes the hyperbolic cosine function, and $\mathrm{Im}(-)$ stands for the imaginary part of a complex number.

The projective special linear group is defined as:

$$\mathrm{PSL}(2, \mathbb{R}) = \mathrm{SL}(2, \mathbb{R})/\{\pm I\}$$

where $\mathrm{SL}(2, \mathbb{R}) = \left\{ \begin{pmatrix} a & b \\ c & d \end{pmatrix} \mid a, b, c, d \in \mathbb{R},\ ad - bc = 1 \right\}$ is the real special linear group, and I denotes the 2×2 identity matrix.

This group acts biholomorphically on $\mathbb{H}$ via fractional linear transformations (Möbius transformations) of the form:

$$z \mapsto \frac{az + b}{cz + d}$$

where $\begin{pmatrix} a & b \\ c & d \end{pmatrix} \in \mathrm{SL}(2, \mathbb{R})$. Moreover, this action preserves the above hyperbolic metric. Furthermore, $\mathrm{PSL}(2, \mathbb{R})$ is exactly the full group of orientation-preserving isometries of $\mathbb{H}$.

Another fundamental model of the hyperbolic plane is the unit disk model. The mapping:

$$z \mapsto \frac{z - i}{z + i}, \quad z \in \mathbb{H}$$

biholomorphically maps $\mathbb{H}$ onto the open unit disk $D = \{w = u + iv \in \mathbb{C} \mid u^2 + v^2 < 1\}$.

The hyperbolic metric induced on D by this mapping is:

$$ds^2 = \frac{4(du^2 + dv^2)}{(1 - (u^2 + v^2))^2}$$

In both the Poincaré upper half-plane model and the unit disk model, the geodesics are generalized circles that intersect the boundary of the model orthogonally. For convenience, we will also use $\mathbb{H}$ to denote the abstract hyperbolic plane when there is no need to specify which concrete model is being referenced.

For background on hyperbolic geometry, one may consult the standard references: Buser[18], Fenchel[27], Imayoshi et al.[38], Iversen[39], Ratcliffe[66], Thurston[74]. For a focused discussion on geodesics in hyperbolic space, see Klingenberg[50], Mirzakhani[55].

Teichmuller Space

The moduli problem for complex structures originates from a fundamental and profound fact: the same oriented two-dimensional differentiable manifold can often support many complex structures that are not isomorphic to each other. In other words, two closed Riemann surfaces, even if they are diffeomorphic as oriented smooth surfaces, are not necessarily biholomorphically equivalent. Therefore, a natural question arises: on a closed oriented surface of a given topological type, how many essentially different complex structures exist? This question is commonly referred to as the *Riemann moduli problem*, and it marks the historical starting point of moduli space theory and Teichmüller theory.

Let Σ_g be a closed oriented surface of genus g, and denote by $\mathcal{M}_g$ the moduli space of all complex structures on Σ_g considered up to biholomorphic equivalence. For low genus, the structure of this space is relatively clear: when $g = 0$, the uniqueness of the Riemann sphere implies that $\mathcal{M}_0$ consists of a single point; when $g = 1$, classical elliptic function theory and the theory of elliptic curves show that the moduli space of complex tori can be described by one complex parameter. The case $g \geq 2$ is where the true richness of geometric and analytic content lies. In 1857, Riemann pointed out that for a closed Riemann surface of genus g, the complex structures should depend on $3g-3$ complex parameters. This count was obtained by viewing the surface as a branched cover of the Riemann sphere and analyzing the degrees of freedom associated with the branch points. Although this argument lacked modern rigor at the time, it accurately revealed the dimension count for higher-genus moduli spaces and laid the foundation for subsequent theoretical developments.

From a modern perspective, an effective way to study $\mathcal{M}_g$ is to first introduce complex structures with a marking, leading to the **Teichmüller space**. Fix a surface Σ_g and consider all pairs (X, f), where X is a closed Riemann surface and $f : \Sigma_g \to X$ is an orientation-preserving homeomorphism, called a marking. Two pairs (X, f) and (Y, g) are considered equivalent if there exists a biholomorphic map $h : X \to Y$ such that $h \circ f$ is homotopic to g. The space of all such equivalence classes is denoted

$$\mathcal{T}_g = \mathcal{T}(\Sigma_g),$$

and is called the Teichmüller space of genus g. The group consisting of homotopy classes of markings, namely

$$\mathrm{Mod}(\Sigma_g) = \pi_0(\mathrm{Homeo}^+(\Sigma_g)),$$

is called the mapping class group. It acts naturally on $\mathcal{T}_g$, and the moduli space can be represented as its quotient:

$$\mathcal{M}_g \cong \mathcal{T}(\Sigma_g)/\mathrm{Mod}(\Sigma_g).$$

This formulation shows that the moduli space is essentially a quotient space obtained by ”forgetting the marking”; consequently, Teichmüller space plays the role of a fundamental object in modern moduli space theory.

Although the explicit notion of Teichmüller space appeared later, its rudiments were already implicit in the work of Klein and Poincaré on Fuchsian groups and automorphic functions. In particular, the Uniformization Theorem states that any closed Riemann surface of genus $g \geq 2$ can be represented as the quotient of the upper half-plane $\mathbb{H}$ by some torsion-free discrete group $\Gamma \subset \mathrm{PSL}(2, \mathbb{R})$,

$$X \cong \mathbb{H}/\Gamma.$$

Thus, the complex structure on a surface translates into a problem of discrete representations of Fuchsian groups, and the conformal geometry of the surface becomes closely linked to the hyperbolic geometry of $\mathbb{H}$. Along these lines, Fricke, Fenchel, and Nielsen systematically constructed Teichmüller space and established the so-called Fricke coordinates, using the parameters of Fuchsian group generators as coordinates. Within this framework, $\mathcal{T}_g$ is described as a space of real dimension $6g - 6$. Early theory already recognized clearly that Teichmüller space should serve as an ”unwrapped” version of moduli space, possessing a geometry more regular than that of $\mathcal{M}_g$ itself.

Teichmüller’s fundamental contribution lay in realizing that if one considers only

conformal maps, the moduli problem often becomes too rigid; however, by introducing *quasiconformal mappings*, the problem acquires a deformable analytic framework. Quasiconformal mappings can be characterized by the Beltrami equation

$$\partial_{\bar{z}} w = \mu \, \partial_z w,$$

where μ is a Beltrami differential satisfying $|\mu|_\infty < 1$, describing how the complex structure deforms relative to the original complex coordinates. One of Teichmüller's key discoveries was the profound correspondence between extremal quasiconformal mappings and holomorphic quadratic differentials. This insight not only provided an intrinsic description of coordinates, geodesics, and distances on Teichmüller space but also endowed the deformation theory of complex structures with a precise analytic formulation for the first time. Based on this idea, Teichmüller introduced the distance that now bears his name and asserted that $\mathcal{T}_g$ is homeomorphic to $\mathbb{R}^{6g-6}$. Although these conclusions lacked complete rigor in their original formulation, their core ideas had a decisive impact on subsequent developments.

By the late 1950s, Ahlfors and Bers laid a rigorous analytic foundation for Teichmüller theory. They systematically proved Teichmüller's main results on extremal quasiconformal mappings and moduli parameters, and further demonstrated that for $g \geq 2$, $\mathcal{T}_g$ is not only a manifold of real dimension $6g-6$ but also carries a natural complex manifold structure, with complex dimension exactly $3g-3$. More concretely, fix a closed Riemann surface X of genus g, and let the vector space of holomorphic quadratic differentials on X be denoted by

$$Q(X) = H^0(X, K_X^{\otimes 2}).$$

By the Riemann–Roch theorem, one obtains

$$\dim_{\mathbb{C}} Q(X) = 3g - 3.$$

Ahlfors and Bers proved that $\mathcal{T}_g$ can be realized via the Bers embedding as a bounded domain in some complex vector space $Q(X)$, thereby endowing Teichmüller space with a well-defined complex analytic structure. This result not only rigorously confirmed Riemann's dimension count but also unified complex analysis, hyperbolic geometry, and topological group actions within a single framework.

Concurrently, the mapping class group $\mathrm{Mod}(\Sigma_g)$ acts on $\mathcal{T}_g$ by biholomorphic auto-

morphisms, and the action is properly discontinuous. Consequently, the quotient space

$$\mathcal{M}_g = \mathcal{T}_g/\mathrm{Mod}(\Sigma_g)$$

naturally inherits the structure of a complex analytic space. In other words, Teichmüller space provides a local analytic model for moduli space, while the mapping class group records the discrete symmetries arising from different markings. In this sense, Teichmüller theory forms the foundation of modern moduli space theory: on one hand, it transforms the classification problem for closed Riemann surfaces into a problem of deforming complex structures and analyzing group actions; on the other hand, it provides essential tools for studying the geometric, topological, and dynamical properties of moduli space.

In summary, the development of Teichmüller space roughly followed this historical trajectory: Riemann first proposed that higher-genus moduli spaces should admit $3g-3$ complex parameters; the uniformization theory of Klein, Poincaré, and Koebe connected surface complex structures with Fuchsian groups; building on this, Fricke, Fenchel, and Nielsen constructed a parameter space in the real-analytic sense; subsequently, Teichmüller revealed the intrinsic geometry of this space through quasiconformal mappings and extremal problems; finally, Ahlfors and Bers established a rigorous complex analytic theory, elevating $\mathcal{T}_g$ to a fundamental object in modern complex geometry, low-dimensional topology, and geometric group theory. It was through this historical process that Teichmüller space evolved from an auxiliary parameter space for the moduli problem into an independent and profound field of study.

Throughout these developments, deformations of Riemann surfaces have been studied from at least three interrelated perspectives:

(1)deformations of Fuchsian groups,

(2)deformations of conformal structures induced by hyperbolic metrics, and

(3)deformations of complex structures induced by quasiconformal mappings.

The essence of the theory lies in exploring Teichmüller spaces from these viewpoints and clarifying the relationships among them.

4.2 Systole Function and Thurston Spine

The definition of topological Morse function is less restrictive than that of classical or smooth Morse function, because it only requires a local homeomorphism to a standard quadratic form, rather than a smooth diffeomorphism. This allows functions with cer-

tain degenerate or nonsmooth critical points to be included, if they are provided locally equivalent to a nondegenerate quadratic form in a topological sense.

Definition 4.1: Let M be an n-dimensional topological manifold. A continuous function $f : M \to \mathbb{R}$ is called a **topological Morse function** if every point $p \in M$ is either a regular point or a critical point with respect to f, characterized by the following local coordinate descriptions:

A point p is **regular** if there exists an open neighborhood U containing p that admits a homeomorphic parametrization $\phi : U \to \mathbb{R}^n$. The n real numbers $(x_1, \dots, x_n) \in \mathbb{R}^n$ are the parameters that uniquely label points in U. After possibly reordering the coordinates, we have:

$$f \circ \phi^{-1}(x) - f(p) = x_n^2.$$

A point p is **critical** if there exists an **index** $j \in \mathbb{Z}$, with $0 \le j \le n$, and a homeomorphic parametrization $\phi : U \to \mathbb{R}^n$ of an open neighborhood U of p, such that under the image coordinates $(x_1, \dots, x_n) \in \mathbb{R}^n$, the function f can be locally expressed as a non-degenerate quadratic form:

$$f \circ \phi^{-1}(x) - f(p) = \sum_{i=1}^{n-j} x_i^2 - \sum_{i=n-j+1}^{n} x_i^2$$

Here, the index j is defined as the "number of negative square terms" in this quadratic form, also called the "index of the critical point".

Example 4.1: Consider the real line $M = \mathbb{R}$ with various functions:

The function $f(x) = x^3$ has vanishing derivative hence is a degenerate critical point at $x = 0$ in the classical definition. However, the homeomorphism $\phi^{-1}(x) = x^{1/3}$ satisfies

$$f\left(\phi^{-1}(x)\right) = \left(x^{1/3}\right)^3 = x,$$

showing that f is locally just the linear coordinate x. Hence $x = 0$ is a topologically regular point, illustrating the topological notion is strictly weaker than the smooth one.

The function $f(x) = x^4$ is not a classical Morse function because its second derivative vanishes at $x = 0$. Nevertheless, an appropriate homeomorphism like

$$\phi^{-1}(z) = \operatorname{sgn}(z) \cdot \sqrt{|z|}$$

transforms f locally into z^2, i.e. $f\left(\phi^{-1}(z)\right) = z^2$. Thus f is a topological Morse function of index 0 at the origin.

The absolute value $f(x) = |x|$ is not smooth at 0, so it cannot be a classical Morse function. Yet the homeomorphism

$$\phi^{-1}(z) = \operatorname{sgn}(z) \cdot z^2$$

yields

$$f\left(\phi^{-1}(z)\right) = |\operatorname{sgn}(z) \cdot z^2| = z^2,$$

proving that $|x|$ is also a topological Morse function of index 0 at the origin.

A broader class of examples: The pointwise minimum of finitely many smooth functions,

$$f(x) := \min_{i=1}^{N} f_i(x),$$

though typically non-differentiable, always furnishes topological Morse functions. This shows that the topological approach easily includes more kinds of functions that commonly appear in variational problems and optimization.

Definition 4.2: The *systole function* $\operatorname{sys}(X)$ is defined as the length of the shortest essential simple closed geodesic on a hyperbolic surface X. It can be expressed as the minimum of a family of smooth geodesic-length functions $\ell_\gamma(X)$:

$$\operatorname{sys}(X) = \min_{\gamma} \ell_\gamma(X).$$

Because it is defined as a minimum, the function fails to be smooth at points where several distinct geodesics simultaneously realize the shortest length. At such points it develops "corners" (nonsmooth behavior), although it remains continuous.

Akrout[1] proved that the systole function, despite being nonsmooth as a minimum of geodesic-length functions, is a *topological Morse function* on both Teichmüller space and moduli space. Its critical points are characterized by a *eutacticity condition*: the origin lies in the (relative) interior of the convex hull of the Weil–Petersson gradients of the geodesic-length functions corresponding to systolic curves. Moreover, the Morse index at such a point equals the rank of these gradients.

Let $S(X)$ denote the set of all curves realizing the systole at X. Consider their Weil–Petersson gradients $\nabla\ell_\gamma(X)$. The *eutactic condition* states that the origin 0 lies in the interior of the convex hull of these gradients (within the subspace they span). Equivalently, there exist positive weights such that the weighted sum of these gradients vanishes. Geometrically, this means that no infinitesimal deformation can simultaneously increase the lengths of all systolic curves; the systole is therefore "locked" at that point. This condition

is necessary and sufficient for X to be a critical point of the systole function.

In topological Morse theory, the *index* of a critical point is the dimension of the space of descending directions. For the systole function, one has the important formula

$$\text{index}(X) = \dim \text{span}\{\nabla \ell_\gamma(X) : \gamma \in S(X)\}.$$

Thus, the index equals the dimension of the linear span of the gradients of the systolic curves, reflecting the number of independent constraints imposed at that point.

A collection of simple closed curves is said to be *filling* if their complement on the surface consists only of disks (or topological polygons). It is known that if X is a critical point of the systole function, then $S(X)$ must be filling. However, the converse does not hold: the filling condition alone does not imply the eutactic condition. Therefore, the set X_g of surfaces whose systoles are filling strictly contains the set of critical points. This distinction plays an important role in understanding the geometric structure of moduli space.

The *Thurston spine* is the subset of Teichmüller space consisting of points whose systoles decompose the surface into polygons. It forms a geometric "skeleton" of Teichmüller space. This set is larger than the set of critical points, as it includes all surfaces satisfying the combinatorial cutting condition. The Thurston spine provides a powerful framework for understanding the topology, geometry, and dynamics of Teichmüller space, and further illustrates the rich structure of the systole function as a geometric Morse function.

Theorem 37 in Schaller[72] provides a symmetry-based criterion for critical points of the systole function on Teichmüller space. It states that if a closed hyperbolic surface M has the property that its full isometry group acts transitively on the set of systolic curves $S(M)$, then M is a critical point of the systole function. The underlying reason is that transitivity forces all systolic geodesics to be geometrically equivalent, so their Weil-Petersson gradients form a single orbit under the isometry group. By symmetry, the sum (and hence a positive weighted combination) of these gradients must vanish, which implies that the origin lies in the interior of their convex hull; in other words, the eutactic condition is automatically satisfied. Thus, high symmetry guarantees the balance condition required for criticality, showing that many highly symmetric hyperbolic surfaces, such as those arising from triangle groups, are natural examples of critical points of the systole function.

4.3 Special Hyperbolic Structures from Regular Maps

Structure equations of polygons

The hyperbolic upper half-plane model has been defined as $\mathbb{H}^2 = \{z \in \mathbb{C} \mid \mathrm{Im}(z) > 0\}$, equipped with the hyperbolic metric $ds^2 = \frac{dx^2 + dy^2}{y^2}$ for $z = x + iy$. The group of orientation-preserving hyperbolic isometries of $\mathbb{H}^2$ is isomorphic to the projective special linear group $\mathrm{PSL}(2,\mathbb{R}) = \mathrm{SL}(2,\mathbb{R})/\{\pm I\}$, where $\mathrm{SL}(2,\mathbb{R}) = \left\{ \begin{pmatrix} a & b \\ c & d \end{pmatrix} \mid a,b,c,d \in \mathbb{R}, ad - bc = 1 \right\}$. Elements of $\mathrm{PSL}(2,\mathbb{R})$ act on $\mathbb{H}^2$ in the form of fractional linear transformations:

For $[A] \in \mathrm{PSL}(2,\mathbb{R})$ with $A = \begin{pmatrix} a & b \\ c & d \end{pmatrix} \in \mathrm{SL}(2,\mathbb{R})$,

$$z \cdot [A] = \frac{az + b}{cz + d}, \quad \forall z \in \mathbb{H}^2.$$

The symbol $[A]$ denotes the equivalence class of A modulo $\pm I$, since A and $-A$ induce the same fractional linear transformation. Where no confusion is likely to arise, we may omit the brackets indicating the equivalence class.

Theorem 4.1 (Rotation about i by Angle θ): The orientation-preserving hyperbolic rotation of $\mathbb{H}^2$ about the point imaginary unit i by angle $\theta \in \mathbb{R}$ is induced by the element

$$\left[\begin{pmatrix} \cos\frac{\theta}{2} & \sin\frac{\theta}{2} \\ -\sin\frac{\theta}{2} & \cos\frac{\theta}{2} \end{pmatrix} \right] \in \mathrm{PSL}(2,\mathbb{R}).$$

Here $\theta > 0$ corresponds to counterclockwise rotation, and $\theta < 0$ corresponds to clockwise rotation.

Proof: We just need to verify three properties of this transformation: 1. the matrix is in $\mathrm{SL}(2,\mathbb{R})$; 2. the transformation fixes point i (i.e. making it to be the center of rotation); 3. the transformation acts as a rotation by θ at the neighborhood of point i in the sense of conformal map.

Compute the determinant of $R_\theta = \begin{pmatrix} \cos\frac{\theta}{2} & \sin\frac{\theta}{2} \\ -\sin\frac{\theta}{2} & \cos\frac{\theta}{2} \end{pmatrix}$, we can easily get:

$$\det(R_\theta) = \cos\frac{\theta}{2} \cdot \cos\frac{\theta}{2} - \sin\frac{\theta}{2} \cdot \left(-\sin\frac{\theta}{2}\right) = \cos^2\frac{\theta}{2} + \sin^2\frac{\theta}{2} = 1.$$

Thus $R_\theta \in \mathrm{SL}(2,\mathbb{R})$, so $[R_\theta] \in \mathrm{PSL}(2,\mathbb{R})$.

Calculate the fractional linear transformation induced by R_θ at $z = i$, and multiply the numerator and denominator by the complex conjugate of the denominator ($\cos\theta +$

$i \sin\theta$) to simplify:

$$\begin{aligned} R_\theta \cdot i &= \frac{\cos\frac{\theta}{2} \cdot i + \sin\frac{\theta}{2}}{-\sin\frac{\theta}{2} \cdot i + \cos\frac{\theta}{2}} \\ &= \frac{(\cos\frac{\theta}{2} \cdot i + \sin\frac{\theta}{2})(\cos\frac{\theta}{2} + i\sin\frac{\theta}{2})}{(\cos\frac{\theta}{2})^2 + (\sin\frac{\theta}{2})^2} \\ &= i\left(\cos^2\frac{\theta}{2} + \sin^2\frac{\theta}{2}\right) + \left(-\cos\frac{\theta}{2}\sin\frac{\theta}{2} + \sin\frac{\theta}{2}\cos\frac{\theta}{2}\right) \\ &= i. \end{aligned}$$

Hence i is a fixed point of the transformation, as required for a rotation about i.

For a holomorphic map $f : \mathbb{C} \to \mathbb{C}$, the angle of rotation at a fixed point z_0 is the argument of the derivative $f'(z_0)$. Therefore, we compute the derivative of the fractional linear transformation $f(z) = R_\theta \cdot z$:

$$f'(z) = \frac{\det(R_\theta)}{(cz+d)^2} = \frac{1}{(-\sin\frac{\theta}{2} \cdot z + \cos\frac{\theta}{2})^2}$$

Evaluate at $z = i$:

$$f'(i) = \frac{1}{(-i\sin\frac{\theta}{2} + \cos\frac{\theta}{2})^2} = \frac{1}{(\cos\frac{\theta}{2} - i\sin\frac{\theta}{2})^2} = \left(\cos\frac{\theta}{2} + i\sin\frac{\theta}{2}\right)^2 = e^{i\theta}.$$

The hyperbolic metric is conformally equivalent to the Euclidean metric on $\mathbb{C}$, so the hyperbolic rotation angle at i is just the argument of $f'(i)$. Thus the hyperbolic rotation angle is θ, as desired.

Since R_θ and $-R_\theta$ induce the same transformation (i.e., $[R_\theta] = [-R_\theta]$), the rotation is uniquely represented by $[R_\theta]$ in $\mathrm{PSL}(2,\mathbb{R})$. ■

Theorem 4.2 (Hyperbolic Translation Upward by Length l): The orientation-preserving hyperbolic translation of $\mathbb{H}^2$ along the imaginary axis with length $l \in \mathbb{R}$ is induced by the element

$$\left[\begin{pmatrix} e^{l/2} & 0 \\ 0 & e^{-l/2} \end{pmatrix}\right] \in \mathrm{PSL}(2,\mathbb{R}).$$

Here $l > 0$ corresponds to upward translation (increasing imaginary part), and $l < 0$ corresponds to downward translation (decreasing imaginary part). The magnitude $|l|$ is the hyperbolic displacement along the imaginary axis.

Proof: First, recall the hyperbolic arc length formula of a curve $\gamma(t) = x(t) + iy(t) \subset$

$\mathbb{H}^2$ ($t \in [a,b] \subset \mathbb{R}$) is integration under the hyperbolic metric:

$$L(\gamma) = \int_a^b \sqrt{\frac{dx(t)^2 + dy(t)^2}{y(t)^2}} = \int_a^b \frac{\|\gamma'(t)\|_{\mathbb{E}}}{\mathrm{Im}(\gamma(t))} dt,$$

where $\|\cdot\|_{\mathbb{E}}$ is the Euclidean norm on $\mathbb{R}^2$. So we only need to verify three properties: 1. the matrix is in $\mathrm{SL}(2,\mathbb{R})$; 2. the transformation acts as a translation along the imaginary axis; 3. the translation moves hyperbolic length l.

Let $T_l = \begin{pmatrix} e^{l/2} & 0 \\ 0 & e^{-l/2} \end{pmatrix}$. Compute its determinant:

$$\det(T_l) = e^{l/2} \cdot e^{-l/2} - 0 \cdot 0 = e^0 = 1.$$

Thus $T_l \in \mathrm{SL}(2,\mathbb{R})$, so $[T_l] \in \mathrm{PSL}(2,\mathbb{R})$.

Evaluate the fractional linear transformation induced by T_l on an arbitrary $z = x + iy \in \mathbb{H}^2$:

$$T_l \cdot z = \frac{e^{l/2} \cdot z + 0}{0 \cdot z + e^{-l/2}} = e^{l/2} \cdot e^{l/2} z = e^l z.$$

For a point on the imaginary axis $z = iy$ ($y > 0$), this simplifies to $T_l \cdot iy = e^l \cdot iy$, which is a pure imaginary axis map (upward along the positive imaginary axis if $l > 0$). For a general point $z = x + iy$, $T_l \cdot z = e^l x + ie^l y$, which preserves Euclidean lines parallel to the imaginary axis and maps the imaginary axis to itself, this is the defining property of a hyperbolic translation along the imaginary axis in $\mathbb{H}^2$.

To confirm the translation length is l, consider the canonical curve along the imaginary axis: $\gamma(t) = ie^t$ for $t \in \mathbb{R}$. Compute its hyperbolic length from $t = 0$ (i.e., $\gamma(0) = i$) to $t = l$ (i.e., $\gamma(l) = ie^l$):

$$\begin{aligned} L(\gamma|_{[0,l]}) &= \int_0^l \frac{\|\gamma'(t)\|_{\mathbb{E}}}{\mathrm{Im}(\gamma(t))} dt \\ &= \int_0^l \frac{e^t}{e^t} dt = \int_0^l 1 dt = l. \end{aligned}$$

The transformation T_l maps $\gamma(t) = ie^t$ to $T_l \cdot \gamma(t) = e^l \cdot ie^t = ie^{t+l} = \gamma(t+l)$. Thus T_l shifts the curve γ by hyperbolic length l along the imaginary axis, which is exactly the hyperbolic translation in the problem statement.

Finally, T_l and $-T_l$ induce the same fractional linear transformation (i.e., $[T_l] = [-T_l]$), so the upward hyperbolic translation is uniquely represented by $[T_l]$ in $\mathrm{PSL}(2,\mathbb{R})$.

■

In the upper half-plane model $\mathbb{H} = \{z \in \mathbb{C} : \mathrm{Im}(z) > 0\}$ of the hyperbolic plane,

the isometry group is $\mathrm{PSL}(2,\mathbb{R}) = \mathrm{SL}(2,\mathbb{R})/\{\pm I\}$. Consider a geodesic polygon with n sides, with vertices $P_1, P_2, \ldots, P_n$ listed counterclockwise, edges l_i connecting P_{i-1} and P_i (indices modulo n), interior angles α_i at vertices P_i, and exterior angles defined as $\theta_i = \pi - \alpha_i$.

To derive the closure condition, we place the polygon in $\mathbb{H}$ and successively apply isometries. Initially, we arrange edge l_1 to lie along the imaginary axis, with vertex P_n aligned at the imaginary unit i. The transformation after this initial state is denoted by $\gamma \in \mathrm{PSL}(2,\mathbb{R})$. The initial transformation is $\gamma_0 = I$.

The process of translating and rotating around the polygon until it returns to its original position proceeds as follows:

（1）Translate along the positive imaginary axis by distance l_1, corresponding to right multiplying by the translation matrix $T(l_1)$, yielding $\gamma_1 = T(l_1)$. At this stage, vertex P_1 is aligned at the point i.

（2）Rotate counterclockwise about point i by the exterior angle θ_1, corresponding to right multiplying by the rotation matrix $R(\theta_1)$, yielding $\gamma_2 = T(l_1)R(\theta_1)$. Edge l_2 now lies along the imaginary axis.

（3）Translate along the positive imaginary axis by distance l_2, corresponding to right multiplying by $T(l_2)$, yielding $\gamma_3 = T(l_1)R(\theta_1)T(l_2)$.

（4）Continue this process, alternating translations and rotations for a total of n translations and n rotations, until all edges and vertices have been traversed. This procedure is illustrated in Figure 4-1.

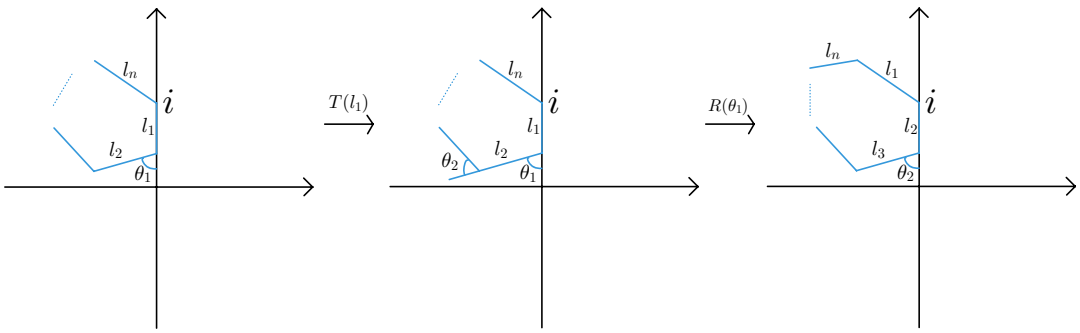

Figure 4-1 The first two steps of translation and rotation for a polygon

The resulting transformation matrix, which incorporates every edge length and vertex angle, is

$$T(l_1)R(\theta_1)T(l_2)R(\theta_2)\cdots T(l_n)R(\theta_n).$$

The condition that the polygon closes and returns to its original position requires that $[\gamma_{2n}] = [I] \in \mathrm{PSL}(2,\mathbb{R})$; that is,

$$\gamma_{2n} = T(l_1)R(\theta_1)T(l_2)R(\theta_2)\cdots T(l_n)R(\theta_n) = \pm I.$$

In fact, the resulting matrix is always $-I$. Here,

$$T(l) = \begin{pmatrix} e^{l/2} & 0 \\ 0 & e^{-l/2} \end{pmatrix}, \qquad R(\theta) = \begin{pmatrix} \cos(\theta/2) & -\sin(\theta/2) \\ \sin(\theta/2) & \cos(\theta/2) \end{pmatrix}.$$

This matrix equation, understood in $\mathrm{PSL}(2,\mathbb{R})$ (allowing for an overall sign), imposes three real constraints. These three constraints determine the geometry of the polygon.

Theorem 4.3: Let $n \geq 5$ be a positive integer. In the hyperbolic plane with curvature $K = -1$, the side length s of a regular n-gon with all interior angles equal to right angles is given by

$$s = 2\ \mathrm{arcosh}\left(\sqrt{2}\cos\frac{\pi}{n}\right).$$

Proof: Consider the hyperbolic plane with curvature $K = -1$, and take a regular n-gon with each interior angle equal to $\alpha = \frac{\pi}{2}$ and side length s. The geometric configuration is illustrated in Figure 4-2.

By symmetry, connect the center O of the polygon to two adjacent vertices A and B, forming an isosceles hyperbolic triangle $\triangle OAB$ where

$$AB = s, \qquad \angle A = \angle B = \frac{\alpha}{2} = \frac{\pi}{4}, \qquad \angle O = \frac{2\pi}{n}.$$

Apply the angular form of the law of cosines to the hyperbolic triangle $\triangle OAB$:

$$\cos\angle O = -\cos\angle A\cos\angle B + \sin\angle A\sin\angle B\cosh(AB).$$

Substituting the known angles gives:

$$\cos\frac{2\pi}{n} = -\left(\cos\frac{\pi}{4}\right)^2 + \left(\sin\frac{\pi}{4}\right)^2\cosh s = -\frac{1}{2} + \frac{1}{2}\cosh s.$$

Rearranging yields:

$$\cosh s = 1 + 2\cos\frac{2\pi}{n}.$$

Thus the side length formula is:

$$s = \mathrm{arcosh}\left(1 + 2\cos\frac{2\pi}{n}\right).$$

Using the identity $\cosh s = 2\cosh^2\frac{s}{2} - 1$, we have

$$2\cosh^2\frac{s}{2} - 1 = 1 + 2\cos\frac{2\pi}{n} \Longrightarrow \cosh\frac{s}{2} = \sqrt{1 + \cos\frac{2\pi}{n}}.$$

Since $\sqrt{1+\cos\theta} = \sqrt{2}\cos\frac{\theta}{2}$ (for $\theta \in [0,\pi]$), taking $\theta = \frac{2\pi}{n}$ gives

$$\cosh\frac{s}{2} = \sqrt{2}\cos\frac{\pi}{n}.$$

Therefore the equivalent form is:

$$s = 2\ \mathrm{arcosh}\left(\sqrt{2}\ \cos\frac{\pi}{n}\right).$$

Note that in the hyperbolic plane, the sum of the interior angles of a regular n-gon must be less than $(n-2)\pi$. Here the sum of interior angles is $n \cdot \frac{\pi}{2}$, so we require $\frac{n\pi}{2} < (n-2)\pi$, i.e., $n > 4$. When $n = 4$, $\cos(2\pi/4) = \cos(\pi/2) = 0$, yielding $\cosh s = 1$ and hence $s = 0$, which degenerates to a point. Therefore, hyperbolic right-angled regular polygons actually exist only for $n \geq 5$. ■

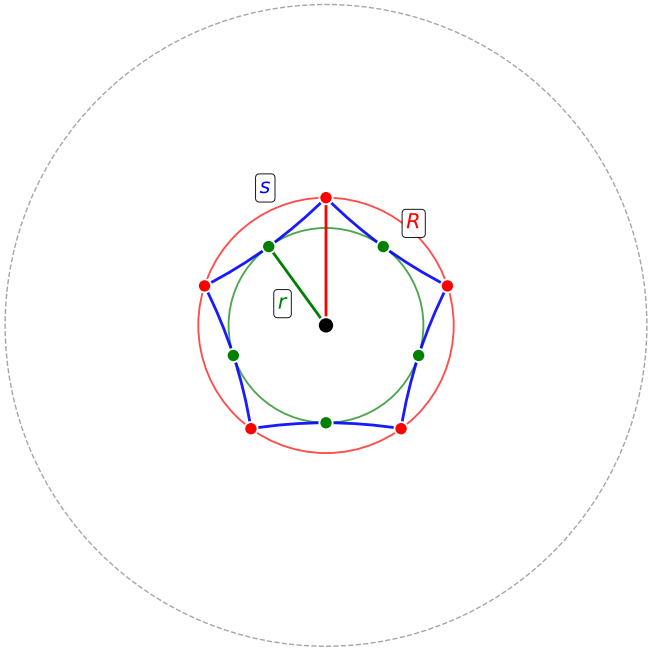

Figure 4-2 Regular right-angled pentagon ($n = 5$) in the Poincaré disk model, drawn to scale. Blue arcs are geodesic edges; red and green circles are the circumcircle (radius R) and incircle (radius r), respectively.

Theorem 4.4: In the hyperbolic plane with curvature $K = -1$, let P be a regular n-gon with interior angle $\alpha = \pi/2$ and side length s ($n \geq 5$). Let O be its center. Then

1. Circumradius (center to vertex) R satisfies:

$$\sinh R = \frac{\sqrt{\cos(2\pi/n)}}{\sin(\pi/n)}, \qquad \cosh R = \cot\frac{\pi}{n}, \qquad R = \operatorname{arcosh}\left(\cot\frac{\pi}{n}\right)$$

2. Inradius (center to midpoint of side) r satisfies:

$$\sinh r = \frac{\sqrt{\cos(2\pi/n)}}{\sqrt{2}\sin(\pi/n)}, \qquad \cosh r = \frac{1}{\sqrt{2}\sin(\pi/n)}, \qquad r = \operatorname{arcosh}\left(\frac{1}{\sqrt{2}\sin(\pi/n)}\right)$$

Proof: It is known in Theorem 4.3 that $\cosh s = 1 + 2\cos\frac{2\pi}{n}$, hence

$$\sinh s = 2\sqrt{\cos\frac{2\pi}{n}(1+\cos\frac{2\pi}{n})} = 2\sqrt{2}\cos\frac{\pi}{n}\sqrt{\cos\frac{2\pi}{n}}.$$

As illustrated in Figure 4-2, $\triangle OAB$ satisfies $OA = OB = R$, $AB = s$, $\angle AOB = 2\pi/n$. Since OA bisects the interior angle $\pi/2$, $\angle OAB = \angle OBA = \pi/4$. Applying the hyperbolic law of sines:

$$\frac{\sin(\pi/4)}{\sinh R} = \frac{\sin(2\pi/n)}{\sinh s}$$

Substituting $\sinh s$ and simplifying yields $\sinh R = \sqrt{\cos(2\pi/n)}/\sin(\pi/n)$. Then $\cosh R = \sqrt{1+\sinh^2 R} = \cot(\pi/n)$ using $\cos(2\pi/n) = 1 - 2\sin^2(\pi/n)$. Hence

$$R = \operatorname{arcosh}(\cot(\pi/n)).$$

Let M be the midpoint of AB, in the right hyperbolic triangle $\triangle OAM$, $\angle M = \pi/2$, $\angle A = \pi/4$, $OA = R$, $OM = r$. By the law of sines:

$$\frac{\sin(\pi/4)}{\sinh r} = \frac{\sin(\pi/2)}{\sinh R}$$

Thus $\sinh r = \sin(\pi/4)\sinh R = \frac{1}{\sqrt{2}}\sinh R = \frac{\sqrt{\cos(2\pi/n)}}{\sqrt{2}\sin(\pi/n)}$. Using $\cosh r = \sqrt{1+\sinh^2 r}$ and $\cos(2\pi/n) = 1 - 2\sin^2(\pi/n)$ gives $\cosh r = \frac{1}{\sqrt{2}\sin(\pi/n)}$, so

$$r = \operatorname{arcosh}\left(\frac{1}{\sqrt{2}\sin(\pi/n)}\right).$$

■

Corollary 4.1 (Asymptotic Behavior): In the hyperbolic plane $K = -1$, consider a regular n-gon ($n \geq 5$) with interior angle $\alpha = \pi/2$. As $n \to \infty$, The side length s_n converges to a positive constant:

$$s_n \longrightarrow s_\infty = 2\ln(1+\sqrt{2}).$$

Both the circumradius R_n and the inradius r_n diverge to infinity, growing logarithmically

in n. However, their difference tends to a finite limit:

$$R_n - r_n \longrightarrow \ln\sqrt{2}.$$

Proof: From $\cosh s = 1 + 2\cos\frac{2\pi}{n}$. As $n \to \infty$, $\cos\frac{2\pi}{n} \to 1$, one has $\cosh s \to 3$. Therefore, side length $s_n \to \operatorname{arcosh} 3 = 2\ln(1+\sqrt{2})$, a constant.

For circumradius R_n, $\cosh R = \cot\frac{\pi}{n} \sim \frac{n}{\pi}$ for large n. Since $\cosh R_n \sim \frac{1}{2}e^{R_n}$, we get $\frac{1}{2}e^{R_n} \sim \frac{n}{\pi}$, $R \sim \ln\frac{2n}{\pi}$. For inradius r_n, $\cosh r_n = \frac{1}{\sqrt{2}\sin(\pi/n)} \sim \frac{n}{\sqrt{2}\,\pi}$. Hence $\frac{1}{2}e^{r_n} \sim \frac{n}{\sqrt{2}\,\pi}$, $r \sim \ln\frac{\sqrt{2}\,n}{\pi}$.

At the end we check the difference of radii. $R_n - r_n \sim \ln\frac{2n}{\pi} - \ln\frac{\sqrt{2}\,n}{\pi} = \ln\sqrt{2}$. The limit $\ln\sqrt{2}$ follows directly from the leading terms. ■

Let $M(l,\theta) = T(l)R(\theta) = \begin{pmatrix} e^{l/2} & 0 \\ 0 & e^{-l/2} \end{pmatrix}\begin{pmatrix} \cos(\theta/2) & -\sin(\theta/2) \\ \sin(\theta/2) & \cos(\theta/2) \end{pmatrix} = \begin{pmatrix} e^{\frac{l}{2}}\cos\frac{\theta}{2} & -e^{\frac{l}{2}}\sin\frac{\theta}{2} \\ e^{-\frac{l}{2}}\sin\frac{\theta}{2} & e^{-\frac{l}{2}}\cos\frac{\theta}{2} \end{pmatrix}$. According to Theorem 4.3, the shape parameters of a right-angled regular polygon are $\theta = \pi/2,\ l = 2\operatorname{arcosh}\left(\sqrt{2}\cos\frac{\pi}{n}\right)$. At this given shape, we compute the values of the transformation $T(l)R(\theta)$ and their partial derivatives as binary functions.

Corollary 4.2: At the right-angled regular n-gon, the parameters take the values $\theta = \pi/2,\ l = s = 2\operatorname{arcosh}\left(\sqrt{2}\cos\frac{\pi}{n}\right)$. We can compute the values of the transformation $T(l)R(\theta)$ and their partial derivatives as binary functions as follows:

$$M\left(s,\frac{\pi}{2}\right) = \frac{\sqrt{2}}{2}\begin{pmatrix} a & -a \\ a^{-1} & a^{-1} \end{pmatrix},$$

$$\left.\frac{\partial M}{\partial\theta}\right|_{(s,\frac{\pi}{2})} = \frac{\sqrt{2}}{4}\begin{pmatrix} -a & -a \\ a^{-1} & -a^{-1} \end{pmatrix},$$

$$\left.\frac{\partial M}{\partial l}\right|_{(s,\frac{\pi}{2})} = \frac{\sqrt{2}}{4}\begin{pmatrix} a & -a \\ -a^{-1} & -a^{-1} \end{pmatrix},$$

where:

$$a = \sqrt{2}\cos\frac{\pi}{n} + \sqrt{\cos\frac{2\pi}{n}}\quad (>1),\quad a^{-1} = \sqrt{2}\cos\frac{\pi}{n} - \sqrt{\cos\frac{2\pi}{n}}.$$

Proof: Given the matrix $M(l,\theta) = T(l)\,R(\theta)$, where

$$T(l) = \begin{pmatrix} e^{l/2} & 0 \\ 0 & e^{-l/2} \end{pmatrix}, \quad R(\theta) = \begin{pmatrix} \cos(\theta/2) & -\sin(\theta/2) \\ \sin(\theta/2) & \cos(\theta/2) \end{pmatrix}.$$

First, clarify:

$$M(l,\theta) = \begin{pmatrix} e^{l/2}\cos(\theta/2) & -e^{l/2}\sin(\theta/2) \\ e^{-l/2}\sin(\theta/2) & e^{-l/2}\cos(\theta/2) \end{pmatrix}.$$

Substitute the given values of the parameters:

$$\theta = \frac{\pi}{2}, \quad l = 2\ \operatorname{arcosh}\left(\sqrt{2}\cos(\pi/n)\right).$$

Let:

$$a = e^{l/2} = \sqrt{2}\cos\frac{\pi}{n} + \sqrt{\cos\frac{2\pi}{n}}, \quad a^{-1} = e^{-l/2} = \sqrt{2}\cos\frac{\pi}{n} - \sqrt{\cos\frac{2\pi}{n}}.$$

Substituting the values $l = s$ and $\theta = \pi/2$, the transformation matrix can be written as:

$$M\left(s, \frac{\pi}{2}\right) = \frac{\sqrt{2}}{2}\begin{pmatrix} a & -a \\ a^{-1} & a^{-1} \end{pmatrix}.$$

Taking the partial derivative with respect to θ, we obtain:

$$\frac{\partial M}{\partial \theta} = \frac{1}{2}\begin{pmatrix} -e^{l/2}\sin(\theta/2) & -e^{l/2}\cos(\theta/2) \\ e^{-l/2}\cos(\theta/2) & -e^{-l/2}\sin(\theta/2) \end{pmatrix}.$$

Taking the partial derivative with respect to l, we obtain:

$$\frac{\partial M}{\partial l} = \frac{1}{2}\begin{pmatrix} e^{l/2}\cos(\theta/2) & -e^{l/2}\sin(\theta/2) \\ -e^{-l/2}\sin(\theta/2) & -e^{-l/2}\cos(\theta/2) \end{pmatrix}.$$

Evaluating the partial derivative with respect to θ at the given values:

$$\left.\frac{\partial M}{\partial \theta}\right|_{(s,\pi/2)} = \frac{\sqrt{2}}{4}\begin{pmatrix} -a & -a \\ a^{-1} & -a^{-1} \end{pmatrix}.$$

Evaluating the partial derivative with respect to l at the given values:

$$\left.\frac{\partial M}{\partial l}\right|_{(s,\pi/2)} = \frac{\sqrt{2}}{4}\begin{pmatrix} a & -a \\ -a^{-1} & -a^{-1} \end{pmatrix}.$$

■

Lemma 4.1 (Derivative of Matrix Product): Let $A : U \to \mathbb{R}^{m\times n}$ and $B : U \to \mathbb{R}^{n\times p}$ be matrix-valued functions defined on an open set $U \subseteq \mathbb{R}^q$, whose entries $A_{ik}(x)$ and

$B_{kj}(x)$ are continuously differentiable functions of the variable $x = (x_1, \dots, x_q)$. Define $C(x) = A(x)B(x)$ with entries

$$C_{ij}(x) = \sum_{k=1}^{n} A_{ik}(x)B_{kj}(x), \quad i = 1, \dots, m,\ j = 1, \dots, p.$$

Then for each component index (i, j) and each partial derivative variable x_ℓ ($\ell = 1, \dots, q$),

$$\frac{\partial C_{ij}}{\partial x_\ell}(x) = \sum_{k=1}^{n} \left[\frac{\partial A_{ik}}{\partial x_\ell}(x)B_{kj}(x) + A_{ik}(x)\frac{\partial B_{kj}}{\partial x_\ell}(x) \right].$$

Proof: Fix indices i, j and a coordinate direction x_ℓ. By definition,

$$C_{ij}(x) = \sum_{k=1}^{n} A_{ik}(x)B_{kj}(x).$$

Since differentiation is linear and the sum is finite,

$$\frac{\partial C_{ij}}{\partial x_\ell}(x) = \sum_{k=1}^{n} \frac{\partial}{\partial x_\ell}\big[A_{ik}(x)B_{kj}(x)\big].$$

For each fixed k, the term $A_{ik}(x)B_{kj}(x)$ is a product of two real-valued differentiable functions of x. By the ordinary product rule from multivariable calculus,

$$\frac{\partial}{\partial x_\ell}\big[A_{ik}(x)B_{kj}(x)\big] = \frac{\partial A_{ik}}{\partial x_\ell}(x)B_{kj}(x) + A_{ik}(x)\frac{\partial B_{kj}}{\partial x_\ell}(x).$$

Substituting this into the sum gives

$$\frac{\partial C_{ij}}{\partial x_\ell}(x) = \sum_{k=1}^{n} \left[\frac{\partial A_{ik}}{\partial x_\ell}(x)B_{kj}(x) + A_{ik}(x)\frac{\partial B_{kj}}{\partial x_\ell}(x) \right].$$

Thus the formula holds for each i, j, ℓ.

If we denote by $\frac{\partial A}{\partial x_\ell}$ the matrix of entrywise partial derivatives $\left[\frac{\partial A_{ik}}{\partial x_\ell}\right]_{i,k}$, then the above componentwise equality can be written in matrix form as

$$\frac{\partial}{\partial x_\ell}(AB) = \frac{\partial A}{\partial x_\ell}B + A\frac{\partial B}{\partial x_\ell}.$$

This is exactly the product rule for matrix-valued functions, applied componentwise and summed. ■

Lemma 4.2 (Derivative for Products of Several Matrix-Valued Functions): Let $A_1 : U \to \mathbb{R}^{m_0 \times m_1}$, $A_2 : U \to \mathbb{R}^{m_1 \times m_2}$, …, $A_N : U \to \mathbb{R}^{m_{N-1} \times m_N}$ be matrix-valued functions defined on an open set $U \subseteq \mathbb{R}^q$, whose entries are continuously differentiable functions of $x = (x_1, \dots, x_q)$. Define the product

$$P(x) = A_1(x)A_2(x) \cdots A_N(x) \in \mathbb{R}^{m_0 \times m_N}.$$

Then for each partial derivative variable x_ℓ ($\ell = 1, \dots, q$),

$$\frac{\partial P}{\partial x_\ell}(x) = \sum_{i=1}^{N} A_1(x) \cdots A_{i-1}(x) \left(\frac{\partial A_i}{\partial x_\ell}(x) \right) A_{i+1}(x) \cdots A_N(x).$$

Equivalently, for each entry index (r, s) with $r \in \{1, \dots, m_0\},\ s \in \{1, \dots, m_N\}$,

$$\frac{\partial P_{rs}}{\partial x_\ell}(x) = \sum_{i=1}^{N} \sum_{\substack{k_1, \dots, k_{N-1} \\ \text{matching dimensions}}} (A_1)_{r,k_1} \cdots (A_{i-1})_{k_{i-2},k_{i-1}} \left(\frac{\partial A_i}{\partial x_\ell} \right)_{k_{i-1},k_i} (A_{i+1})_{k_i,k_{i+1}} \cdots (A_N)_{k_{N-1},s}.$$

Proof: We proceed by induction on N, the number of matrices.

Base case $N = 2$. Let $P = A_1 A_2$. By the standard matrix product rule (which follows from the scalar product rule applied entrywise, as proven in the previous theorem),

$$\frac{\partial P}{\partial x_\ell} = \frac{\partial A_1}{\partial x_\ell} A_2 + A_1 \frac{\partial A_2}{\partial x_\ell}.$$

This matches the claimed formula with $i = 1, 2$.

Assume the formula holds for a product of $N - 1$ matrices. Write

$$P = (A_1 A_2 \cdots A_{N-1}) A_N = Q A_N,$$

where $Q = A_1 \cdots A_{N-1}$. By the product rule for two matrices,

$$\frac{\partial P}{\partial x_\ell} = \frac{\partial Q}{\partial x_\ell} A_N + Q \frac{\partial A_N}{\partial x_\ell}.$$

Apply the induction hypothesis to $\frac{\partial Q}{\partial x_\ell}$:

$$\frac{\partial Q}{\partial x_\ell} = \sum_{i=1}^{N-1} A_1 \cdots A_{i-1} \left(\frac{\partial A_i}{\partial x_\ell} \right) A_{i+1} \cdots A_{N-1}.$$

Multiplying on the right by A_N gives

$$\frac{\partial Q}{\partial x_\ell} A_N = \sum_{i=1}^{N-1} A_1 \cdots A_{i-1} \left(\frac{\partial A_i}{\partial x_\ell} \right) A_{i+1} \cdots A_{N-1} A_N.$$

The second term $Q \cdot \frac{\partial A_N}{\partial x_\ell}$ is simply $A_1 \cdots A_{N-1} \cdot \frac{\partial A_N}{\partial x_\ell}$, which corresponds to the $i = N$ term in the sum. Adding them together, we obtain

$$\frac{\partial P}{\partial x_\ell} = \sum_{i=1}^{N} A_1 \cdots A_{i-1} \left(\frac{\partial A_i}{\partial x_\ell} \right) A_{i+1} \cdots A_N.$$

This completes the induction. ■

Hyperbolic right-angled regular polygon: side-length–exterior-angle coordinates and geometric structure equations

For a hyperbolic polygon, the side lengths and interior angles must satisfy the structure equation

$$M_1 M_2 \cdots M_n = -I.$$

Define $F := M_1 M_2 \cdots M_n$. Then the matrix equation $F = -I$ is equivalent to four real equations: $F_{11} = -1,\ F_{12} = 0,\ F_{21} = 0,\ F_{22} = -1$. Since $F \in \mathrm{SL}(2, \mathbb{R})$, we have $\det(F) = 1$, and among these four real equations there is one constraint:

$$F_{11} F_{22} - F_{12} F_{21} = 1. \tag{4-1}$$

Thus, only three real equations serve as constraints.

Let the variable x represent any length l_i or angle θ_j. Taking the total differential of equation (4-1) yields:

$$\frac{\partial F_{11}}{\partial x} dx + \frac{\partial F_{22}}{\partial x} dx = 0,$$

which indicates that in the tangent space, the gradients ∇F_{11} and ∇F_{22} are linearly dependent. In the following, we will only consider $F_\delta,\ \delta \in \{(1,1), (1,2), (2,1)\}$.

We may consider an infinitesimal deformation near a given hyperbolic structure on the surface, which corresponds to taking the total differential of $F = -I$. From this, we obtain linear relations among the infinitesimal elements of each length l_i and angle θ_j. The space of all parameters is denoted by:

$$\mathcal{P}_{l,\theta} := \mathbb{R}^n \times \mathbb{R}^n \ni (l_i, \theta_j).$$

Near a point in $\mathcal{P}_{l,\theta}$, the total differential yields the linear relations:

$$dF_\delta = \sum_{i=1}^{n} \frac{\partial F_\delta}{\partial l_i} dl_i + \sum_{j=1}^{n} \frac{\partial F_\delta}{\partial \theta_j} d\theta_j = 0, \quad \delta \in \{(1,1), (1,2), (2,1)\}. \tag{4-2}$$

The subspace spanned by these relations corresponds to the tangent space of the hyperbolic structure equation $F = -I$ at that point.

Now, suppose our polygon is a right-angled regular n-gon, so all real parameters take the values $l_i = s,\ \theta_j = \pi/2$. The values of the transformation matrices and their partial derivatives are independent of the index i.

$$M_i\left(s,\frac{\pi}{2}\right)=M=M\left(s,\frac{\pi}{2}\right)=\frac{\sqrt{2}}{2}\begin{pmatrix}a & -a\\ a^{-1} & a^{-1}\end{pmatrix},$$

$$\left(\frac{\partial M_i}{\partial l_i}\right)\Big|_{(s,\frac{\pi}{2})}=M_l=\frac{\partial M}{\partial\theta}\Big|_{(s,\frac{\pi}{2})}=\frac{\sqrt{2}}{4}\begin{pmatrix}-a & -a\\ a^{-1} & -a^{-1}\end{pmatrix},$$

$$\left(\frac{\partial M_i}{\partial \theta_i}\right)\Big|_{(s,\frac{\pi}{2})}=M_\theta=\frac{\partial M}{\partial l}\Big|_{(s,\frac{\pi}{2})}=\frac{\sqrt{2}}{4}\begin{pmatrix}a & -a\\ -a^{-1} & -a^{-1}\end{pmatrix},$$

where:

$$a=\sqrt{2}\cos\frac{\pi}{n}+\sqrt{\cos\frac{2\pi}{n}}\quad(>1),\quad a^{-1}=\sqrt{2}\cos\frac{\pi}{n}-\sqrt{\cos\frac{2\pi}{n}}.$$

According to Lemma 4.2, the differential of each element can be computed using the Leibniz rule for products of several matrix-valued functions. Let the variable x_i be either l_i or θ_j:

$$\begin{aligned}\frac{\partial F}{\partial x_i}\Big|_{(s,\frac{\pi}{2})}&=\frac{\partial}{\partial x_i}\left(M_1M_2\cdots M_n\right)\Big|_{(s,\pi/2)}\\&=\sum_{i=1}^{n}M_1\cdots M_{i-1}\left(\frac{\partial M_i}{\partial x_i}\right)M_{i+1}\cdots M_n\Big|_{(s,\frac{\pi}{2})}\\&=M^{i-1}\cdot\left(\frac{\partial M_i}{\partial x_i}\right)\Big|_{(s,\frac{\pi}{2})}\cdot M^{n-i}\\&=M^{i-1}\cdot M_x\cdot M^{n-i}.\end{aligned}$$

For each matrix entry, we obtain three differential constraints:

$$\frac{\partial F_\delta}{\partial x_i}\Big|_{(s,\frac{\pi}{2})}=\left(\frac{\partial F}{\partial x_i}\Big|_{(s,\frac{\pi}{2})}\right)_\delta=\left(M^{i-1}\cdot M_x\cdot M^{n-i}\right)_\delta,\quad\delta\in\{(1,1),(1,2),(2,1)\}.\tag{4-3}$$

Theorem 4.5: Let $(P,\langle\cdot,\cdot\rangle)$ be a finite-dimensional real inner product space, let $V\subset P$ be a subspace, and let $s:P\to\mathbb{R}$ be a linear functional. Then

1. There exists a unique vector $\nabla s\in P$ such that

$$s(x)=\langle\nabla s,x\rangle,\quad\forall x\in P.$$

∇s is called the **gradient** of s in P (Riesz representation vector).

2. There exists a unique vector $\nabla(s|_V) \in V$ such that

$$s(v) = \langle \nabla(s|_V), v \rangle, \quad \forall v \in V.$$

$\nabla(s|_V)$ is called the **gradient** of $s|_V$ in V.

Let $\pi_V : P \to V$ be the orthogonal projection induced by $\langle \cdot, \cdot \rangle$. Then

$$\nabla(s|_V) = \pi_V(\nabla s).$$

In other words: The gradient of the restricted functional equals the orthogonal projection of the gradient of the original functional onto the subspace.

Proof: The orthogonal projection $\pi_V : P \to V$ is uniquely determined by the condition:

$$\langle \pi_V(x) - x, v \rangle = 0, \quad \forall v \in V.$$

Equivalently: $x - \pi_V(x) \in V^\perp$.

Next, we verify that $\pi_V(\nabla s)$ satisfies the representation property for $s|_V$.

Take any $v \in V$. By the property of orthogonal projection,

$$\nabla s = \pi_V(\nabla s) + \eta, \quad \eta \in V^\perp.$$

Then

$$s(v) = \langle \nabla s, v \rangle = \langle \pi_V(\nabla s) + \eta, v \rangle = \langle \pi_V(\nabla s), v \rangle + \langle \eta, v \rangle.$$

Since $\eta \in V^\perp$ and $v \in V$, we have $\langle \eta, v \rangle = 0$. Therefore

$$s(v) = \langle \pi_V(\nabla s), v \rangle, \quad \forall v \in V.$$

Finally, regarding uniqueness, the Riesz representation vector of $s|_V$ in V is unique, and $\pi_V(\nabla s) \in V$ satisfies this representation property, so $\nabla(s|_V) = \pi_V(\nabla s)$. This completes the proof. ■

Remark 4.1: In the above proposition, the definition of "gradient" depends on the given inner product $\langle \cdot, \cdot \rangle$ on P. If the inner product changes, both ∇s and $\nabla(s|_V)$ will change, but the relationship $\nabla(s|_V) = \pi_V(\nabla s)$ still holds for the orthogonal projection induced by the same inner product.

The π_V in the proposition must be the orthogonal projection (relative to the inner product defining the gradient). If an oblique projection is used, the conclusion generally does not hold, because an oblique projection cannot guarantee $\langle \eta, v \rangle = 0$ for all $v \in V$.

Coordinate representation (taking $P = \mathbb{R}^m$ with the standard inner product as an example): Suppose $s(x) = a^\mathsf{T} x$, then $\nabla s = a$. Let $Q \in \mathbb{R}^{m \times n}$ be a matrix whose

columns form an orthonormal basis of V (so $Q^{\mathsf{T}}Q = I_n$). Then

$$\pi_V(x) = QQ^{\mathsf{T}}x.$$

Hence

$$\nabla(s|_V) = \pi_V(a) = QQ^{\mathsf{T}}a.$$

Direct verification: for any $v = Qy \in V$,

$$s(v) = a^{\mathsf{T}}Qy = (Q^{\mathsf{T}}a)^{\mathsf{T}}y = (QQ^{\mathsf{T}}a)^{\mathsf{T}}Qy = \langle \pi_V(a), v \rangle.$$

Theorem 4.6: Let $(P, \langle \cdot, \cdot \rangle_P)$ be an m-dimensional real inner product space, and let $(W, \langle \cdot, \cdot \rangle_W)$ be a k-dimensional real inner product space. Let $J : P \to W$ be a linear map, and denote $V = \ker J \subset P$ as the null space of J. Denote $V^{\perp} = \{x \in P \mid \langle x, v \rangle_P = 0,\ \forall v \in V\}$ as the orthogonal complement of V in P with respect to the inner product $\langle \cdot, \cdot \rangle_P$.

Then

$$V^{\perp} = \{J^{\dagger}(w) \mid w \in W\}$$

where $J^{\dagger} : W \to P$ is the *adjoint map* of J with respect to the given inner products, defined by:

$$\langle J^{\dagger}(w), p \rangle_P = \langle w, J(p) \rangle_W, \quad \forall p \in P,\ \forall w \in W.$$

Equivalently, if we take orthonormal bases of P and W, represent J by a matrix $A \in \mathbb{R}^{k \times m}$, represent the inner product $\langle \cdot, \cdot \rangle_P$ by a symmetric positive definite matrix $M \in \mathbb{R}^{m \times m}$, and represent the inner product $\langle \cdot, \cdot \rangle_W$ by a symmetric positive definite matrix $N \in \mathbb{R}^{k \times k}$, then

$$V^{\perp} = \{M^{-1}A^{\mathsf{T}}Ny \mid y \in \mathbb{R}^k\}.$$

In particular, when $P = \mathbb{R}^m$ and $W = \mathbb{R}^k$ both have the standard inner product (i.e., $M = I_m$, $N = I_k$),

$$V^{\perp} = \{A^{\mathsf{T}}y \mid y \in \mathbb{R}^k\} = \mathrm{row}(A) = \mathrm{col}(A^{\mathsf{T}}).$$

Proof: Suppose the inner product on P is $\langle p, q \rangle_P = p^{\mathsf{T}}Mq$, with M symmetric positive definite. Suppose the inner product on W is $\langle w, z \rangle_W = w^{\mathsf{T}}Nz$, with N symmetric positive definite. Let the matrix representation of J under the standard bases be $A \in \mathbb{R}^{k \times m}$, i.e., $J(p) = Ap$.

The adjoint map $J^{\dagger} : W \to P$ is determined by the definition $\langle J^{\dagger}(w), p \rangle_P =$

$\langle w, J(p)\rangle_W$.

Let $J^\dagger(w) = Xw$, where $X \in \mathbb{R}^{m\times k}$ is to be determined. Then

$$\langle J^\dagger(w), p\rangle_P = (Xw)^\mathsf{T} Mp = w^\mathsf{T} X^\mathsf{T} Mp.$$

$$\langle w, J(p)\rangle_W = w^\mathsf{T} N(Ap) = w^\mathsf{T} NAp.$$

Since this holds for all $w \in \mathbb{R}^k$ and $p \in \mathbb{R}^m$, we have

$$X^\mathsf{T} M = NA \quad \Rightarrow \quad X^\mathsf{T} = NAM^{-1} \quad \Rightarrow \quad X = M^{-1}A^\mathsf{T} N.$$

Therefore

$$J^\dagger(w) = M^{-1}A^\mathsf{T} Nw, \quad \forall w \in \mathbb{R}^k.$$

Take any $w \in W$, and let $x = J^\dagger(w)$. For any $v \in V = \ker J$ (i.e., $Av = 0$), we have

$$\langle x, v\rangle_P = (M^{-1}A^\mathsf{T} Nw)^\mathsf{T} Mv = w^\mathsf{T} NAM^{-1} Mv = w^\mathsf{T} N(Av) = w^\mathsf{T} N \cdot 0 = 0.$$

Thus $x \in V^\perp$. Therefore $J^\dagger(W) \subseteq V^\perp$.

By the dimension formula:

$$\dim V = \dim\ker J = m - \operatorname{rank} J.$$

$$\dim V^\perp = m - \dim V = \operatorname{rank} J.$$

And $J^\dagger$ is the adjoint of J, so they have the same rank: $\operatorname{rank} J^\dagger = \operatorname{rank} J$. Hence $\dim J^\dagger(W) = \operatorname{rank} J^\dagger = \operatorname{rank} J = \dim V^\perp$.

Combining $J^\dagger(W) \subseteq V^\perp$ with equal dimensions yields

$$J^\dagger(W) = V^\perp.$$

Thus we obtain:

$$V^\perp = \{J^\dagger(w) \mid w \in W\} = \{M^{-1}A^\mathsf{T} Nw \mid w \in \mathbb{R}^k\}.$$

When $M = I_m$ and $N = I_k$,

$$J^\dagger(w) = A^\mathsf{T} w.$$

In this case, the column space of $A^\mathsf{T} \in \mathbb{R}^{m\times k}$ is precisely $\operatorname{col}(A^\mathsf{T}) = \operatorname{row}(A)$. Therefore

$$V^\perp = \operatorname{col}(A^\mathsf{T}) = \{A^\mathsf{T} y \mid y \in \mathbb{R}^k\}.$$

The orthogonal complement of the null space equals the row space. This completes the proof. ■

Theorem 4.7: Let P be a finite-dimensional real linear space, and let $V \subset P$ be a sub-

space. Let $\pi_V : P \to V$ be a (fixed, arbitrary) projection onto V, and let $\ker \pi_V$ be the kernel of the projection (i.e., the space of the projection direction). Let $\{s_1, \dots, s_k\} \subset P$ be a set of linearly independent vectors, and denote $S = \text{span}\{s_1, \dots, s_k\}$. Consider the projected set of vectors $\{\pi_V(s_1), \dots, \pi_V(s_k)\} \subset V$. Then we have the following conclusions:

1. The projected set of vectors is linearly dependent if and only if $S \cap \ker \pi_V \neq \{0\}$, i.e., the original space S has a nontrivial intersection with the kernel of the projection.

2. The dimension lost by the projection (i.e., the dimension compressed during the projection) is exactly equal to $\dim(S \cap \ker \pi_V)$. The dimension of the space spanned after projection is:

$$\dim \pi_V(S) = \dim S - \dim(S \cap \ker \pi_V).$$

Proof: Let $T : S \to V$ be the linear map obtained by restricting the projection map π_V to S, i.e., $T(s) = \pi_V(s)$ for any $s \in S$.

By the fundamental theorem of linear algebra (rank-nullity theorem):

$$\dim S = \dim \operatorname{Im} T + \dim \ker T.$$

Here, $\operatorname{Im} T = \pi_V(S)$ is the image space after projection, and $\ker T = S \cap \ker \pi_V$ is the kernel of the projection restricted to S.

Therefore:

$$\dim \pi_V(S) = \dim S - \dim(S \cap \ker \pi_V).$$

If $S \cap \ker \pi_V \neq \{0\}$, then $\dim(S \cap \ker \pi_V) \geq 1$, and hence

$$\dim \pi_V(S) \leq k - 1 < k = \dim S.$$

This means the k projected vectors cannot span a k-dimensional space, so they must be linearly dependent (since k linearly independent vectors would span a k-dimensional space).

Conversely, if the projected set of vectors is linearly dependent, then $\dim \pi_V(S) < k$. From the dimension formula we get

$$\dim(S \cap \ker \pi_V) = \dim S - \dim \pi_V(S) \geq 1,$$

hence $S \cap \ker \pi_V \neq \{0\}$.

This proves the equivalence:

$$\{\pi_V(s_1), \dots, \pi_V(s_k)\} \text{ is linearly dependent} \iff S \cap \ker \pi_V \neq \{0\}.$$

The dimension formula follows directly from the rank-nullity theorem:

$$\dim \pi_V(S) = \dim S - \dim(S \cap \ker \pi_V).$$

This is the formula for the dimension of the space spanned after projection. The lost dimension is defined as the difference between the dimension of the original space and the dimension of the image space after projection:

$$\text{Lost dimension} = \dim S - \dim \pi_V(S).$$

Substituting the dimension formula:

$$\text{Lost dimension} = \dim S - [\dim S - \dim(S \cap \ker \pi_V)] = \dim(S \cap \ker \pi_V).$$

Thus, the lost dimension is exactly equal to the dimension of the intersection of the original space S with the projection kernel $\ker \pi_V$. The compression originates from the directions lying in the projection kernel being completely "flattened."

■

Remark 4.2: The above proposition holds for any linear projection π_V (not necessarily orthogonal). As long as π_V is a linear map satisfying $\pi_V|_V = \mathrm{id}_V$, the kernel $\ker \pi_V$ is the space of the projection direction.

If π_V is an orthogonal projection, then $\ker \pi_V = V^\perp$. In this case, the proposition becomes:

$$\dim \pi_V(S) = \dim S - \dim(S \cap V^\perp).$$

The lost dimension equals the dimension of the intersection of S with the orthogonal complement of V.

4.4 Deformation of Hyperbolic Structure

If one considers the set of shortest geodesics that fill a hyperbolic structure, then the entire Teichmüller space deformation retracts onto this subspace. Moreover, the critical points of the systole function, viewed as a topological Morse function, lie in the Thurston spine, so the index of these critical points can be used to study the dimension and cell structure of the spine. Schmutz Schaller[72] showed that surfaces with such symmetries are precisely the critical points. In their search for minimal filling sets that decompose the surface, An et al.[2] computed cases for n from 5 to 8 and conjectured that the index is $n \cdot 2^{n-3} - (n+3)$. Our work uses a different method to obtain the hyperbolic structures; this construction is consistent and holds for all n. Using this method, we computed cases for n from 5 to 12, and the results agree with the conjecture.

Calculation method

If we require that, within the closed surface obtained from the dual decomposition, the four edges still constitute geodesics, each of which may vary in length, and that at each vertex the four interior angles sum to π, then we have $n \cdot 2^{n-1}$ real parameters for the edge lengths and $n \cdot 2^{n-2}$ real parameters for the angles. There are 2^n faces, each subject to three constraints, so the total dimension is

$$n \cdot 2^{n-1} + n \cdot 2^{n-2} - 3 \cdot 2^n = 3(n-4)2^{n-2} = 6g - 6 = \dim \mathcal{M}_g,$$

which provides an alternative parametrization of moduli space. This perspective can serve as a starting point for computing the index of the systole function. Denote the $n \cdot 2^{n-1}$ edge lengths by l_i and the $n \cdot 2^{n-2}$ angles by θ_j.

The systole function index of surface $M(n,-1)^* = Z(C_n, (D^1, S^0))^*$

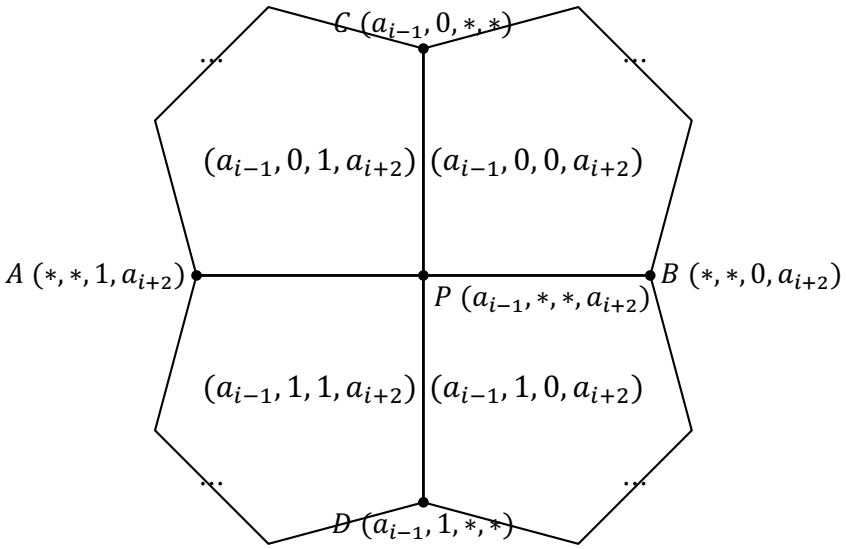

Figure 4-3 Local geometric configuration around a point P, showing its four adjacent points A, B, C, D, four incident edges , and four incident faces. For clarity, coordinates are displayed only for indices from $i-1$ to $i+2$. Due to the perigon 360° at P and the geodesic nature of its edges, adjacent faces meeting at P have supplementary dihedral angles, while opposite faces share the same angle.

Next, for the surface $M(n,-1)^* = Z(C_n, (D^1, S^0))^*$ with $n \geq 5$, we study the linear dependence relations, in the tangent space of Teichmüller space, among the gradients of the length functions corresponding to each systole on this surface.

First, we introduce the encoding rules for the set of objects. Given an integer $n \geq 5$, we use the symbol set $\{0, 1, *\}$ on a string of length n, and encode three types of objects as follows:

1. Face objects:

$$\mathfrak{F} = \mathbb{F}_2^n.$$

A face $f \in \mathfrak{F}$ is denoted as a binary vector $f = (a_1, \dots, a_n)$, where $a_i \in \{0, 1\}$. The total number of faces is $|\mathfrak{F}| = 2^n$.

2. Edge objects:

$$\mathfrak{E} = \mathbb{Z}/n \times \mathbb{F}_2^{n-1}.$$

An edge can be understood as a string with "exactly one position equal to $*$": for each $i \in \mathbb{Z}/n$, the edge (l, i) has the i-th position equal to $*$, and the remaining $n-1$ positions are $0/1$. The total number of edges is

$$|\mathfrak{E}| = n \cdot 2^{n-1}.$$

3. Point objects:

$$\mathfrak{P} = \mathbb{Z}/n \times \mathbb{F}_2^{n-2}.$$

A point can be understood as a string with "two adjacent positions equal to $*$": for each $i \in \mathbb{Z}/n$, the point (θ, i) has the i-th and $(i+1)$-th positions equal to $*$ (indices are cyclic), and the remaining $n-2$ positions are $0/1$. The total number of points is

$$|\mathfrak{P}| = n \cdot 2^{n-2}.$$

Linear algebra data: 2×2 fundamental matrices and local weights

Define the parameters

$$a = \sqrt{2}\cos\frac{\pi}{n} + \sqrt{\cos\frac{2\pi}{n}}, \qquad a^{-1} = \sqrt{2}\cos\frac{\pi}{n} - \sqrt{\cos\frac{2\pi}{n}},$$

and construct three 2×2 real matrices M, M_l, M_θ as following,

$$M = \frac{\sqrt{2}}{2}\begin{pmatrix} a & -a \\ a^{-1} & a^{-1} \end{pmatrix}, \quad M_l = \frac{\sqrt{2}}{4}\begin{pmatrix} -a & -a \\ a^{-1} & -a^{-1} \end{pmatrix}, \quad M_\theta = \frac{\sqrt{2}}{4}\begin{pmatrix} a & -a \\ -a^{-1} & -a^{-1} \end{pmatrix}.$$

For each position $i = 1, \dots, n$ and type $x \in \{l, \theta\}$, define

$$F_{(x,i)} := M^{i-1} M_x M^{n-i}.$$

Fix a set of entry extractions

$$\Delta = \{11, 12, 21\},$$

indicating that we extract the three entries $(1,1), (1,2), (2,1)$ from the 2×2 matrices.

Constructing the matrix V

Construct the matrix

$$V \in \mathbb{R}^{(3\cdot 2^n)\times(|\mathfrak{E}|+|\mathfrak{P}|)},$$

whose rows are indexed by $(f,\delta) \in \mathfrak{F} \times \Delta$ and columns by $\mathfrak{E} \cup \mathfrak{P}$.

Define the incidence function χ as follows: for an edge or a point element, $\chi(x,f) = 1$ if x is incident to face f, and 0 otherwise. The geometric notion of incidence is captured systematically using symbolic coordinates, with the precise conditions given below:

• An edge $e \in \mathfrak{E}$ is incident to a face f if and only if, after ignoring the position marked with $*$ in e, the remaining coordinates exactly match the corresponding $0/1$ entries of f.

• A point $p \in \mathfrak{P}$ is incident to a face f if and only if, after ignoring the two positions marked with $*$ in p, the remaining coordinates exactly match the corresponding $0/1$ entries of f.

Then define the matrix entries:

• If the column corresponds to an edge $e = (l,i,\cdot) \in \mathfrak{E}$, then

$$V\big((f,\delta),e\big) = \chi(e,f)\cdot\big(F_{(l,i)}\big)_\delta.$$

• If the column corresponds to a point $p = (\theta,i,\cdot) \in \mathfrak{P}$, then

$$V\big((f,\delta),p\big) = \chi(p,f)\cdot(-1)^{a_i+a_{i+1}}\cdot\big(F_{(\theta,i)}\big)_\delta.$$

Constructing the circle-constraint matrix S

Construct the matrix

$$S \in \mathbb{R}^{(|\mathfrak{E}|/4)\times(|\mathfrak{E}|+|\mathfrak{P}|)}.$$

Each row corresponds to a ”circle” (specially it is exactly all the systoles): fix a star position i, and fix the $0/1$ values of all $n-3$ positions except $i-1, i, i+1$; then let the binary values at positions $i-1$ and $i+1$ vary freely, yielding four edges

$$(0/1, *, 0/1)$$

(i.e., the three positions $i-1, i, i+1$ are respectively $0/1, *, 0/1$), which form the same circle. For the four edge columns corresponding to this circle, the entries are set to 1; all other edge columns are set to 0, and all point columns (corresponding to $\mathfrak{P}$) are identically 0. Thus each row contains exactly four 1’s, and the number of rows is

$$|\mathfrak{E}|/4 = n\cdot 2^{n-3}.$$

Final computation goal

Compute the dimension of the intersection of the row spaces of V and S. By vertically concatenating V and S, we obtain

$$A = \begin{pmatrix} V \\ S \end{pmatrix},$$

and compute its *numerical rank*, equivalently its *numerical nullity*

$$\text{nullity}(A) = \min(\#\text{rows}, \#\text{cols}) - \text{rank}(A) = \text{rank}(S) + \text{rank}(V) - \text{rank}(A),$$

where the rank is defined using a threshold criterion (tol) for the SVD: singular values $\sigma \leq$ tol are considered zero.

Calculation result

Table 4-1 Calculation result of nullity and rank

n	row(V)	row(S)	shape(A)	rank(A)	nullity	nullity$-n$
5	96	20	[116, 120]	108	8	3
6	192	48	[240, 288]	231	9	3
7	384	112	[496, 672]	486	10	3
8	768	256	[1024, 1536]	1013	11	3
9	1536	576	[2112, 3456]	2100	12	3
10	3072	1280	[4352, 7680]	4339	13	3
11	6144	2816	[8960, 16896]	8946	14	3
12	12288	6144	[18432, 36864]	18417	15	3

Singular Value Decomposition (SVD) provides a theoretically complete and numerically stable method for determining the rank of a matrix. For any matrix $A \in \mathbb{R}^{m\times n}$, its singular value decomposition can be written as $A = U\Sigma V^{\top}$, where U and V are orthogonal matrices, and Σ is a diagonal matrix whose diagonal entries $\sigma_1 \geq \sigma_2 \geq \cdots \geq \sigma_{\min(m,n)} \geq 0$ are called singular values. Fundamental results in linear algebra establish that the rank of a matrix equals the number of its non-zero singular values. This conclusion stems from the fact that the invertibility of U and V guarantees $\text{rank}(A) = \text{rank}(\Sigma)$, and the rank of the diagonal matrix Σ is precisely the number of its non-zero diagonal entries. Geometrically, singular values characterize the scaling factors of the linear transformation in each principal direction; the number of non-zero singular values is exactly the dimension of the transformed space, which is the rank of the matrix.

In numerical computing environments, due to rounding errors in floating-point arith-

metic, theoretically zero singular values manifest as extremely small non-zero values (typically on the order of machine precision $\epsilon_{\text{mach}} \approx 10^{-16}$). Therefore, we need to introduce threshold-based criteria to distinguish numerically non-zero singular values from those that are effectively zero. A commonly used threshold selection strategy is based on machine precision and matrix dimensions: an absolute threshold $\tau = \epsilon_{\text{mach}} \cdot \max(m, n) \cdot \sigma_1$, where σ_1 is the largest singular value. This choice is justified because the numerical error in SVD is of order $O(\epsilon_{\text{mach}}\|A\|)$. A more robust approach involves analyzing the distribution of the singular value spectrum to identify significant jumps in the ratio of consecutive singular values σ_i/σ_{i+1}—if there exists an r such that $\sigma_{r+1}/\sigma_1 \ll 1$ and $\sigma_r/\sigma_{r+1} \gg 1$, then the rank of the matrix can be determined as r. This gap-based singular value determination method effectively overcomes the uncertainties introduced by floating-point precision and provides numerically stable rank estimation.

CHAPTER 5 DEGENERACY SURFACES IN QUANTUM PHYSICS

5.1 Quantum Theory

Condensed matter physics studies the collective behavior of systems composed of a very large number of particles, such as electrons and ions in crystalline solids. A central objective is to understand the energy spectrum, quantum states, and elementary excitations of such systems. The basic mathematical language for this purpose is quantum mechanics, in which the physical state space is modeled by a Hilbert space and the dynamics are determined by a Hamiltonian operator[71].

The Hamiltonian, originating in classical mechanics and generalized in quantum theory, represents the total energy of a physical system. In quantum mechanics, the Hamiltonian $\hat{H}$ is an operator acting on a Hilbert space, and the time evolution of the system is governed by the Schrödinger equation

$$i\hbar\frac{\partial}{\partial t}|\psi\rangle = \hat{H}|\psi\rangle,$$

where $|\psi\rangle$ denotes the wave function, or more generally the quantum state, of the system. The Hamiltonian determines both the time evolution of the system and its allowed energy levels. In condensed matter systems, it typically contains the kinetic energies of electrons and ions together with their mutual interactions, including electron-electron, electron-ion, and ion-ion interactions[32,71].

5.1.1 Energy Bands

For crystalline solids, translational symmetry plays a fundamental role. The periodic structure of a crystal lattice implies that the single-particle Hamiltonian is invariant under lattice translations. Bloch's theorem states that, in a periodic potential, the wave function of an electron can be written in the form

$$\psi_{n,\mathbf{k}}(\mathbf{r}) = e^{i\mathbf{k}\cdot\mathbf{r}}u_{n,\mathbf{k}}(\mathbf{r}),$$

where $u_{n,\mathbf{k}}(\mathbf{r})$ has the same periodicity as the crystal lattice[5,15,49]. Here $\mathbf{k}$ is the crystal wavevector, which lives in reciprocal space and labels Bloch states.

Because of lattice periodicity, it is sufficient to study the system within the first Bril-

louin zone, which is a fundamental domain of the reciprocal lattice[5,49]. After Bloch decomposition, the Hamiltonian can be represented as a family of matrices $H(\mathbf{k})$, called Bloch Hamiltonians. For each $\mathbf{k}$, one solves the eigenvalue problem

$$H(\mathbf{k})|u_n(\mathbf{k})\rangle = E_n(\mathbf{k})|u_n(\mathbf{k})\rangle.$$

The eigenvalues $E_n(\mathbf{k})$, as functions of $\mathbf{k}$, form the *energy bands* of the system. Thus, the band structure describes how the electron energy varies with crystal momentum.

The separation between neighboring bands may open *band gaps*, which are crucial for distinguishing metals, semiconductors, and insulators. The electronic properties of a material are largely determined by the position of the Fermi level relative to the energy bands: if the Fermi level crosses a band, the system typically behaves as a metal, whereas if it lies inside a band gap, the system may behave as an insulator or a semiconductor[5,49]. Moreover, the dispersion relation $E_n(\mathbf{k})$ also determines important dynamical quantities. For example, its gradient gives the group velocity of a wave packet,

$$\mathbf{v}_n(\mathbf{k}) = \frac{1}{\hbar}\nabla_{\mathbf{k}} E_n(\mathbf{k}),$$

while its local curvature is related to the effective mass of quasiparticles[5,49].

In modern condensed matter theory, one is often interested not only in the eigenvalues $E_n(\mathbf{k})$, but also in the eigenstates $|u_n(\mathbf{k})\rangle$. These may carry geometric and topological information, such as Berry phases and topological invariants, which play an essential role in the study of topological materials[5,71]. In practice, the analysis of a crystalline system usually begins with the construction of an effective Hamiltonian in momentum space, and the solution of its eigenvalue problem yields the corresponding band structure.

5.1.2 Hermiticity and Pseudo-Hermitian Quantum Mechanics

When only finitely many bands are relevant, the effective Hamiltonian at each $\mathbf{k}$-point is represented by a finite-dimensional matrix. In conventional closed quantum systems, this matrix is required to be Hermitian:

$$H(\mathbf{k}) = H^{\dagger}(\mathbf{k}), \qquad H_{ij}(\mathbf{k}) = \overline{H_{ji}(\mathbf{k})}.$$

Hermiticity guarantees real expectation values of observables and unitary time evolution. In the finite-dimensional case, it also implies that the eigenvalues are real and that the eigenvectors can be chosen to form a complete orthonormal basis[32,71].

However, many realistic physical systems are effectively open and may exchange energy or particles with their environment. This naturally leads to non-Hermitian de-

scriptions, which arise, for instance, in optical and photonic systems with gain and loss, in dissipative systems, and in effective descriptions of resonances[12,57]. In general, a non-Hermitian Hamiltonian may have complex eigenvalues. Physically, the real part often describes energy or oscillation frequency, while the imaginary part is related to amplification, attenuation, or finite lifetime[36,57].

Unlike the Hermitian case, non-Hermitian Hamiltonians generally require one to distinguish between right and left eigenvectors:

$$H|\psi_n^R\rangle = E_n|\psi_n^R\rangle, \qquad H^\dagger|\psi_n^L\rangle = \overline{E_n}|\psi_n^L\rangle.$$

These vectors typically form a biorthogonal system rather than an orthonormal basis, and this biorthogonal structure is fundamental in non-Hermitian spectral theory[57,59]. Another characteristic feature of non-Hermitian systems is the existence of *exceptional points*, at which both eigenvalues and eigenvectors coalesce. At such points the Hamiltonian becomes non-diagonalizable and develops Jordan block structure, leading to phenomena with no Hermitian analogue[13,36].

A particularly important class of non-Hermitian Hamiltonians is provided by *pseudo-Hermitian* operators. A Hamiltonian H is called η-pseudo-Hermitian if there exists an invertible Hermitian operator η such that

$$\eta H \eta^{-1} = H^\dagger.$$

This means that H is Hermitian with respect to the modified inner product

$$\langle \psi, \phi \rangle_\eta := \langle \psi|\eta|\phi\rangle.$$

Pseudo-Hermiticity does not automatically imply that the whole spectrum is real; more generally, it implies a complex-conjugation symmetry of the spectrum, and under suitable additional conditions the spectrum may become entirely real[58-59]. This framework is closely related to $\mathcal{PT}$-symmetric quantum mechanics, where a non-Hermitian Hamiltonian invariant under the combined action of parity and time reversal may exhibit a wholly real spectrum in the unbroken phase, while complex-conjugate pairs of eigenvalues appear after symmetry breaking[12,59].

In non-Hermitian band theory, several new phenomena arise that have no direct counterpart in ordinary Hermitian systems. One of the most notable is the *non-Hermitian skin effect*, in which a macroscopic number of eigenstates become exponentially localized near the boundary under open boundary conditions. This reveals a striking sensitivity of non-Hermitian spectra to boundary conditions and motivates the use of generalized Brillouin

zones and non-Bloch band theory[13,77].

For the particular choice

$$\eta = \mathrm{diag}(-1, 1, 1),$$

the modified inner product is indefinite, with signature $(-,+,+)$. This is exactly the signature of the Minkowski metric in $2+1$-dimensional spacetime, so the geometry induced by η is naturally analogous to that of $2+1$-dimensional Minkowski space. Hence, the underlying space is an indefinite inner-product space rather than a standard Hilbert space.

5.2 Ruled Surfaces

5.2.1 Classification and Properties of Ruled Surfaces

Definition 5.1: A surface formed by the movement of a straight line along a curve in 3-dimensional Euclidean space is called a **ruled surface**. A parametric vector representation of a ruled surface can be written in the following form:

$$\mathbf{r}(u, v) = \mathbf{c}(u) + v \cdot \mathbf{l}(u)$$

both $\mathbf{c}(u)$ and $\mathbf{l}(u)$ should be differentiable and $\mathbf{l}(u) \neq \mathbf{0}$ for any u.

Straight lines belonging to a ruled surface are called rectilinear generatrixes or rectilinear generators or rulings. A curve intersecting all rulings of the surface is called a directrix curve or a director curve or a directing curve.

Definition 5.2 (tangent developable surface): A **tangent developable surface** is a particular kind of developable surface obtained from a curve $\mathbf{c}$ in Euclidean space $\mathbb{R}^3$ and swept out by its tangent lines $\mathbf{c}'(u)$ as $\mathbf{l}(u)$. That means any tangent developable surface is described by a parametric representation:

$$\mathbf{r}(u, v) = \mathbf{c}(u) + \mathbf{c}'(u) \cdot v$$

Example 5.1: As an example, consider the tangent developable surface with a helix as its directing curve $\mathbf{c}(u)$. Figure 5-1 shows its image. The parametric equation for the helix is:

$$\begin{cases} x = a\cos u \\ y = a\sin u \\ z = \dfrac{h}{2\pi}u \end{cases}$$

The parameter a is the constant radius of the circular component of the helix, defining

the distance from the helix to its central axis, the z-axis in this case. The parameter h represents the pitch of the helix, which is the linear distance the helix advances along the z-axis in one full revolution.

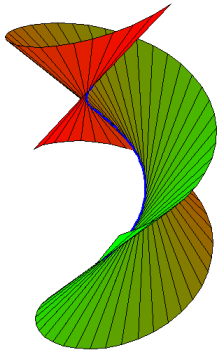

Figure 5-1 The tangent developable of a helix, cited from Wikipedia: Tangent developable surface

Definition 5.3 (developable surface): The **developable surface** is a surface in 3-dimensional Euclidean space with **zero** Gaussian curvature.

Theorem 5.1 (Euler 1772): Any tangent developable surface is a developable surface. And that every developable surface is of one of generalized cones and the cylinders and tangent developable surface.

5.2.2 Ruledness of Discriminant Surfaces

Prototype: General cubic polynomial

First of all, we will investigate the discriminant surface of a generic degree-3 polynomial. The equation is $f(\lambda) = \lambda^3 + x\lambda^2 + y\lambda + z = 0$, where x, y, z are paramaters. $f(\lambda) = 0$ has a zero with multiplicity at least 2, iff $(f, f') \neq 1$. The discriminant can be calculated from the resultant of f and f',

$$\Delta(x, y, z) = x^2y^2 - 4x^3z - 4y^3 + 18xyz - 27z^2.$$

Now we will show that the discriminant surface $\Delta = 0$ is a ruled surface. Suppose t is the common root of f and f', then

$$\begin{cases} t^3 + xt^2 + yt + z = 0 \\ 3t^2 + 2xt + y = 0 \end{cases} \tag{5-1}$$

regard t as a new paramater, y and z can be expressed by x and t:

$$\begin{cases} y = -3t^2 - 2xt \\ z = 2t^3 + xt^2 \end{cases} \tag{5-2}$$

Since the discriminant surface can be paramaterized in the following form,

$$\begin{bmatrix} x \\ y \\ z \end{bmatrix} = \begin{bmatrix} 0 \\ -3t^2 \\ 2t^3 \end{bmatrix} + x \begin{bmatrix} 1 \\ -2t \\ t^2 \end{bmatrix}, \tag{5-3}$$

this form suggests that the surface is a ruled surface.

If $f(\lambda)$ has a zero t with multiplicity 3. f can be written as $f(\lambda) = (\lambda - t)^3 = \lambda^3 - 3t\lambda^2 + 3t^2\lambda - t^3$. We have correspondence of coefficients

$$\begin{cases} x = -3t \\ y = 3t^2 \\ z = -t^3 \end{cases} \tag{5-4}$$

This parameterized curve is a caspidal edge on the discriminant surface.

Proposition 5.1: The discriminant surface of the generic cubic polynomial is a tangent developable surface.

Proof: Let $\gamma(t)$ be a parameterized smooth curve described as above triple multiplicity curve, $\gamma(t) = (-3t, 3t^2, -t^3)$. Then the tangent developable surface defined by γ is parameterized by the following map

$$(t, s) \mapsto \gamma(t) + s\gamma'(t).$$

Taking this coefficients in the cubic polynomial we can obtain the decomposition

$$f(\lambda) = \lambda^3 - (3t + 3s)\lambda^2 + (3t^2 + 6ts)\lambda - (t^3 + 3t^3 s) = (\lambda - t)^2(\lambda - (t + 3s)).$$

This suggests that the tangent developable surface given by $(t, s) \mapsto \gamma(t) + s\gamma'(t)$ is just the discriminant surface. ■

Corollary 5.1: The discriminant surface of generic cubic polynomial is a developable surface.

5.2.3 Three Energy Band Systems and Examples

Four swallowtails (sw4):

The characteristic polynomial of matrix

$$\begin{bmatrix} 1 & f_1 & f_2 \\ -f_1 & -1 & f_3 \\ -f_2 & f_3 & -1 \end{bmatrix}$$

is $g(\lambda) = \lambda^3 + \lambda^2 + (f_1^2 + f_2^2 - f_3^2 - 1)\lambda + (f_1^2 + f_2^2 + f_3^2 + 2f_1f_2f_3 - 1)$. The discriminant of $g(\lambda) = 0$ is $\Delta = 4f_1^4 - 4f_1^6 + 8f_1^2f_2^2 - 12f_1^4f_2^2 + 4f_2^4 - 12f_1^2f_2^4 - 4f_2^6 + 64f_1f_2f_3 - 72f_1^3f_2f_3 - 72f_1f_2^3f_3 + 64f_3^2 - 80f_1^2f_3^2 + 12f_1^4f_3^2 - 80f_2^2f_3^2 - 84f_1^2f_2^2f_3^2 + 12f_2^4f_3^2 - 144f_1f_2f_3^3 - 32f_3^4 - 12f_1^2f_3^4 - 12f_2^2f_3^4 + 4f_3^6$.

If $g(\lambda)$ have multiple roots at t, then $(\lambda - t)|(g, g')$. Using the result from Example 1, We have correspondence of coefficients

$$\begin{cases} x = 1 \\ y = -3t^2 - 2xt = f_1^2 + f_2^2 - f_3^2 - 1 \\ z = 2t^3 + xt^2 = f_1^2 + f_2^2 + f_3^2 + 2f_1f_2f_3 - 1 \end{cases} \tag{5-5}$$

Eliminating this system of equations, with t and f_3 as parameters, we can simplify and obtain the following results:

$$\begin{cases} f_1^2 + f_2^2 = f_3^2 - 3t^2 - 2t + 1 \\ f_1f_2 = \dfrac{t(t+1)^2}{f_3} - f_3 \end{cases} \tag{5-6}$$

Calculate the squares of sum and difference of f_1 and f_2, finally obtain the following factorizations:

$$\begin{cases} (f_1 + f_2)^2 = \dfrac{f_3^3 - 2f_3^2 - (3t^2 + 2t - 1)f_3 + 2t(t+1)^2}{f_3} \\ \qquad\qquad = \dfrac{(f_3 + 2t)(f_3 - t - 1)^2}{f_3} \\ (f_1 - f_2)^2 = \dfrac{f_3^3 + 2f_3^2 - (3t^2 + 2t - 1)f_3 - 2t(t+1)^2}{f_3} \\ \qquad\qquad = \dfrac{(f_3 - 2t)(f_3 + t + 1)^2}{f_3} \end{cases} \tag{5-7}$$

Let $2\sin^2\theta \cdot f_3 = f_3 + 2t$ (It shows that $t = -\frac{1}{2}f_3\cos 2\theta$). However, we will discuss two extra cases where the equation may not hold.

One case is $f_3 = 0$, (5-7) implies that $t = 0$ or $t = -1$. We only consider $t = -1$, since the $t = 0$ case is contained in the next main case. $t = -1$ leads to $f_1 = f_2 = 0$.

The other case is the quadratic terms on both sides of one equation of (5-7) are zero,

which shows that the left can be negative. Consider

$$f_1 + f_2 = f_3 - t - 1 = 0$$

in (5-7), then

$$4f_1^2(t+1) = (-t+1)\cdot 4(t+1)^2 \tag{5-8}$$

Thus, $(t+1)(f_1^2 + t^2 - 1) = 0$. When $t + 1 = 0$, it has been discussed above. A parametrization of f_1, f_2 and f_3 can be

$$\begin{cases} f_1 = \cos\psi \\ f_2 = -\cos\psi \\ f_3 = 1 + \sin\psi \end{cases} \tag{5-9}$$

In the same way, consider

$$f_1 - f_2 = f_3 + t + 1 = 0$$

in (5-7), then

$$\begin{cases} f_1 = \cos\psi \\ f_2 = \cos\psi \\ f_3 = -1 - \sin\psi \end{cases} \tag{5-10}$$

For general case,

$$\begin{cases} (f_1 + f_2)^2 = 2\sin^2\theta(f_3 - t - 1)^2 \\ (f_1 - f_2)^2 = 2\cos^2\theta(f_3 + t + 1)^2 \end{cases} \tag{5-11}$$

There are four cases for $f_1 + f_2$ and $f_1 - f_2$ as for the signs. For case 1,

$$\begin{cases} f_1 + f_2 = \sqrt{2}\sin\theta(f_3 - t - 1) \\ f_1 - f_2 = \sqrt{2}\cos\theta(f_3 + t + 1) \end{cases} \tag{5-12}$$

we obtain

$$\begin{aligned} f_1 &= \frac{\sqrt{2}}{2}\sin\theta(f_3 - t - 1) + \frac{\sqrt{2}}{2}\cos\theta(f_3 + t + 1) \\ &= \frac{\sqrt{2}}{2}(\sin\theta + \cos\theta)f_3 + \frac{\sqrt{2}}{2}(\cos\theta - \sin\theta)(t+1) \\ &= \sin(\theta + \frac{\pi}{4})f_3 + \cos(\theta + \frac{\pi}{4})(t+1) \\ &= \sin(\theta + \frac{\pi}{4})f_3 + \cos(\theta + \frac{\pi}{4})(-\frac{1}{2}\cos 2\theta f_3 + 1) \\ &= (\sin(\theta + \frac{\pi}{4}) - \frac{1}{2}\cos(\theta + \frac{\pi}{4})\cos 2\theta)f_3 + \cos(\theta + \frac{\pi}{4}) \end{aligned}$$

$$= (\sin(\theta + \frac{\pi}{4}) - \cos^2(\theta + \frac{\pi}{4})\sin(\theta + \frac{\pi}{4}))f_3 + \cos(\theta + \frac{\pi}{4})$$
$$= \sin^3(\theta + \frac{\pi}{4})f_3 + \cos(\theta + \frac{\pi}{4})$$

Replace $\theta + \frac{\pi}{4}$ by φ, then

$$f_1 = \sin^3\varphi f_3 + \cos\varphi \tag{5-13}$$

For f_2,

$$\begin{aligned} f_2 &= \frac{\sqrt{2}}{2}\sin\theta(f_3 - t - 1) - \frac{\sqrt{2}}{2}\cos\theta(f_3 + t + 1) \\ &= \frac{\sqrt{2}}{2}(\sin\theta - \cos\theta)f_3 - \frac{\sqrt{2}}{2}(\cos\theta + \sin\theta)(t + 1) \\ &= -\cos(\theta + \frac{\pi}{4})f_3 - \sin(\theta + \frac{\pi}{4})(t + 1) \\ &= -\cos\varphi f_3 - \sin\varphi(-\frac{1}{2}\sin 2\varphi f_3 + 1) \\ &= (-\cos\varphi + \sin^2\varphi\cos\varphi)f_3 - \sin\varphi \\ &= -\cos^3\varphi f_3 - \sin\varphi \end{aligned} \tag{5-14}$$

Thus, for case 1,

$$\begin{cases} f_1 = \sin^3\varphi f_3 + \cos\varphi \\ f_2 = -\cos^3\varphi f_3 - \sin\varphi \end{cases} \tag{5-15}$$

Remark 5.1: For the other cases, they can change the solutions to f_1, f_2 by the following two methods: (1) change the signs of both f_1 and f_2; (2) exchange the results of f_1 and f_2.

Remark 5.2: Since the discriminant surface can be paramaterized in the form

$$\begin{bmatrix} f_1 \\ f_2 \\ f_3 \end{bmatrix} = \begin{bmatrix} \cos\varphi \\ -\sin\varphi \\ 0 \end{bmatrix} + f_3 \begin{bmatrix} \sin^3\varphi \\ -\cos^3\varphi \\ 1 \end{bmatrix}, \tag{5-16}$$

it is a ruled surface.

Stratification Structure Analysis

In a three-band system with three control parameters, the degeneracy set may form geometric objects of different dimensions in parameter space, such as surfaces, isolated lines, intersection lines, caspidal edges, or isolated points. A key distinction is whether the degeneracy is non-defective or exceptional. In a non-defective degeneracy, the eigenvalues become degenerate while the corresponding eigenstates remain linearly independent,

so the Hamiltonian is still diagonalizable. In contrast, at an exceptional degeneracy, both the eigenvalues and the eigenstates coalesce, and the Hamiltonian becomes defective. Accordingly, a nodal line (NL) is an ordinary line degeneracy with independent eigenstates, while an exceptional line (EL) and an exceptional surface (ES) consist of defective degeneracies. A non-defective intersection line (NIL) refers to an intersection line of degeneracy manifolds where the eigenstates remain linearly independent. Finally, a meeting point (MP) is a special point where different degeneracy structures meet or reconnect, and its local spectral properties depend on the specific model.

Table 5-1 Types of degeneracies in a three-band system with three parameters.

Abbreviation	Name	Eigenvalues	Eigenstates
ES	exceptional surface	coalescing	coalescing
NIL	non-defective intersection line	degenerate	linearly independent
NL	nodal line	degenerate	linearly independent
EL	exceptional line	coalescing	coalescing
MP	meeting point	multiple degeneracies meet	model-dependent

According to prototype, the EL parts consist of 3 multiplicity. We suppose the 3 multiply root is t, hence $x = -3t = 1$. And we have already set $2t = -f_3\cos(2\theta) = -f_3\sin(2\varphi)$, so $f_3 = \dfrac{2}{3\sin(2\varphi)}$.

$$f_1 = \frac{2\sin^3\varphi}{3\sin(2\varphi)} + \cos\varphi = \frac{1}{3\cos\varphi} + \frac{2}{3}\cos\varphi$$
$$f_2 = -\frac{2\cos^3\varphi}{3\sin(2\varphi)} - \sin\varphi = -\frac{1}{3\sin\varphi} - \frac{2}{3}\sin\varphi$$

Therefore, the EL parts can be described as parameter curves:

$$\begin{cases} f_1 = \dfrac{1}{3\cos\varphi} + \dfrac{2}{3}\cos\varphi \\ f_2 = -\dfrac{1}{3\sin\varphi} - \dfrac{2}{3}\sin\varphi \\ f_3 = \dfrac{2}{3\sin 2\varphi} \end{cases} \tag{5-17}$$

Actually, this curve is naturally divided into four parts at $\varphi = 0, \frac{\pi}{2}, \pi, \frac{3}{4}\pi$, since the denominator is 0. And the minimum absolution of f_3 is reached by $\varphi = \frac{\pi}{4}, \frac{3}{4}\pi, \frac{5}{4}\pi, \frac{7}{4}\pi$. These 4 points are

$$(\frac{2}{3}\sqrt{2}, -\frac{2}{3}\sqrt{2}, \frac{2}{3}),\ (-\frac{2}{3}\sqrt{2}, \frac{2}{3}\sqrt{2}, -\frac{2}{3}),\ (\frac{2}{3}\sqrt{2}, \frac{2}{3}\sqrt{2}, -\frac{2}{3}),\ (-\frac{2}{3}\sqrt{2}, -\frac{2}{3}\sqrt{2}, -\frac{2}{3}),$$

which contribute to 4 MPs.

Eigenstates of ES and EL, the 2-multiply real root is We know in these parts, there is a good parametrization in φ and f_3. We have assumed that $t = -\frac{1}{2}f_3 \sin 2\varphi$ is a at least 2-multiply root. The other root is $-1 + f_3 \sin 2\varphi$. So the eigenvalues of the Hamiltonian matrix are

$$-\frac{1}{2}f_3 \sin 2\varphi,\ -\frac{1}{2}f_3 \sin 2\varphi,\ -1 + f_3 \sin 2\varphi,$$

and their corresponding eigenstates are

$$\begin{bmatrix} 1 \\ -\cos\varphi \\ \sin\varphi \end{bmatrix}, \begin{bmatrix} -4f_3\cos(2\varphi) \\ 4\sin\varphi + f_3(-5\cos\varphi + \cos(3\varphi)) \\ -4\cos\varphi + f_3(5\sin\varphi + \sin(3\varphi)) \end{bmatrix}$$

It is easy to observe on the region ES, the 2 multiple roots has only 1 corresponding eigenvector.

When $-\frac{1}{2}f_3 \sin 2\varphi = -1 + f_3 \sin 2\varphi$ i.e. $f_3 = \frac{2}{3\sin(2\varphi)}$ all roots merge into a 3 multiple root as we have shown. In this case, the 3 multiple root is $-\frac{1}{3}$. Considering the eigenstates, there are two situations on ELs and MPs regions. If $\varphi \notin \{0, \frac{\pi}{2}, \pi, \frac{3}{4}\pi, \frac{\pi}{4}, \frac{3}{4}\pi, \frac{5}{4}\pi, \frac{7}{4}\pi\} + 2k\pi,\ k \in \mathbb{Z}$, i.e. in the region ELs, then the eigenvalue $-\frac{1}{3}$ have just 1 corresponding eigenvector

$$\begin{bmatrix} 1 \\ -\cos\varphi \\ \sin\varphi \end{bmatrix}.$$

If $\varphi \in \{\frac{\pi}{4}, \frac{3}{4}\pi, \frac{5}{4}\pi, \frac{7}{4}\pi\} + 2k\pi,\ k \in \mathbb{Z}$, i.e. at the 4 MPs, then the eigenvalue $-\frac{1}{3}$ have 2 different corresponding eigenvectors,

$$\begin{bmatrix} -1/\sqrt{2} \\ 1 \\ 0 \end{bmatrix}, \begin{bmatrix} 1/\sqrt{2} \\ 0 \\ 1 \end{bmatrix}.$$

Theorem 5.2: The discriminant surface sw4 is a tangent developable surface.

Proof: EL part in (5-17) is exactly the corresponding curve $\gamma(\varphi)$ of tangent developable surface sw4. We can verify that $\Delta(\gamma(\varphi) + s\gamma'(\varphi)) = 0$. ■

We have a line l_φ in 3D space with coordinates (f_1, f_2, f_3), parameterized by $t = f_3$

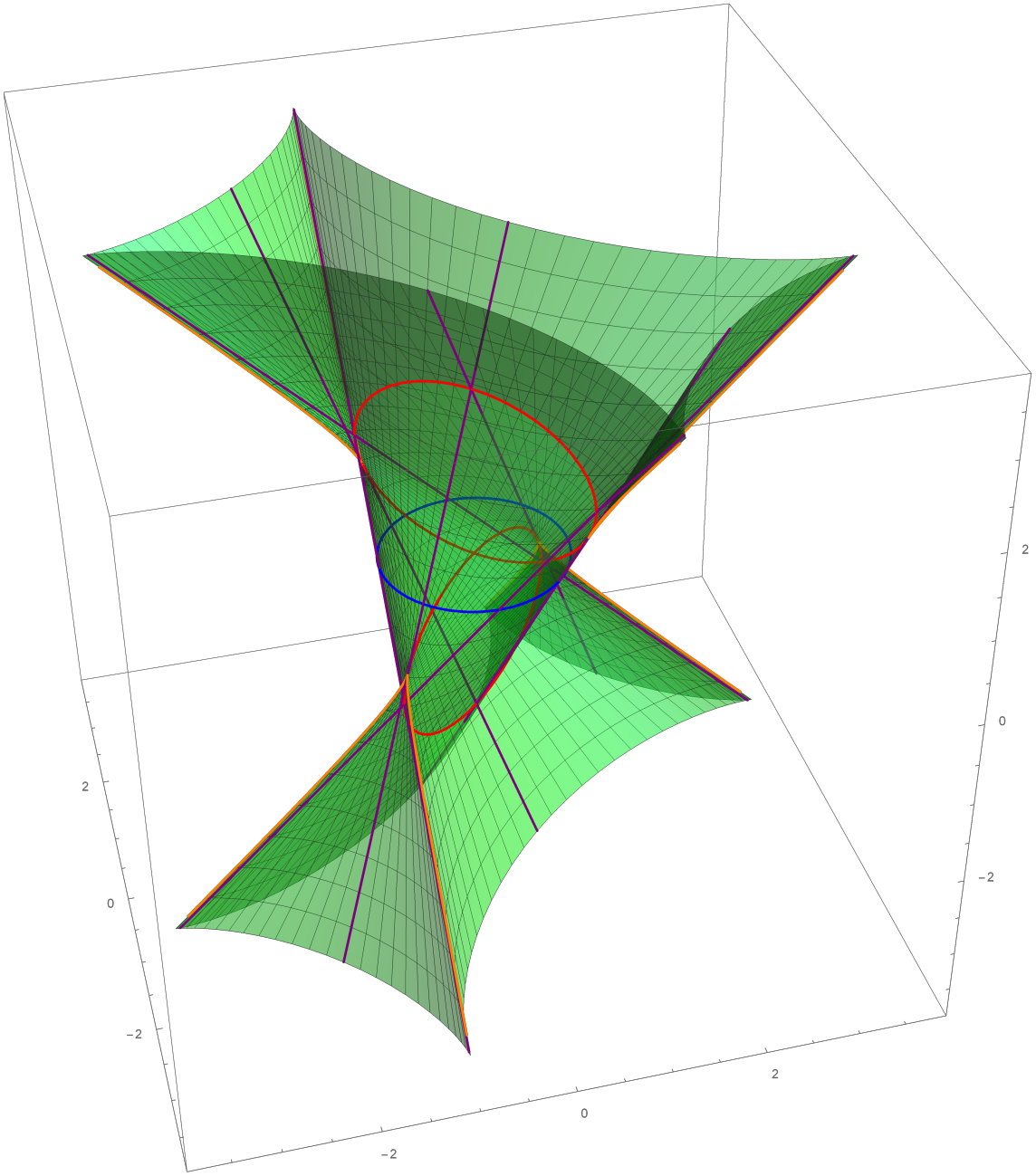

Figure 5-2 This figure illustrates a ruled algebraic surface with four swallowtail singularities and three ellipses.

and fixed φ:

$$f_1 = \cos\varphi + t\sin^3\varphi, \quad f_2 = -\sin\varphi - t\cos^3\varphi, \quad f_3 = t.$$

As φ varies, the family of such lines forms a ruled surface Σ. We want the tangent plane T_φ to Σ along the line l_φ.

Proposition 5.2: The tangent plane T_φ to the surface Σ along the line l_φ is given by the equation

$$-\cos\varphi\, f_1 + \sin\varphi\, f_2 + \sin\varphi\cos\varphi\, f_3 + 1 = 0,$$

or

$$f_3 = \frac{f_1}{\sin\varphi} - \frac{f_2}{\cos\varphi} - \frac{1}{\sin\varphi\,\cos\varphi}$$

Proof: The surface Σ is parametrized by (φ, t) as:

$$\mathbf{R}(\varphi,t) = \begin{pmatrix} \cos\varphi + t\sin^3\varphi \\ -\sin\varphi - t\cos^3\varphi \\ t \end{pmatrix}.$$

The two tangent vectors are:

$$\mathbf{R}_\varphi = \frac{\partial\mathbf{R}}{\partial\varphi} = \begin{pmatrix} -\sin\varphi + 3t\sin^2\varphi\cos\varphi \\ -\cos\varphi + 3t\cos^2\varphi\sin\varphi \\ 0 \end{pmatrix},$$

$$\mathbf{R}_t = \frac{\partial\mathbf{R}}{\partial t} = \begin{pmatrix} \sin^3\varphi \\ -\cos^3\varphi \\ 1 \end{pmatrix}.$$

The normal vector $\mathbf{n} = \mathbf{R}_\varphi \times \mathbf{R}_t$ is computed as follows. Let

$$A = -\sin\varphi + 3t\sin^2\varphi\cos\varphi, \quad B = -\cos\varphi + 3t\cos^2\varphi\sin\varphi.$$

Then

$$\mathbf{n} = \begin{pmatrix} B \\ -A \\ -A\cos^3\varphi - B\sin^3\varphi \end{pmatrix} = \begin{pmatrix} -\cos\varphi + 3t\cos^2\varphi\sin\varphi \\ \sin\varphi - 3t\sin^2\varphi\cos\varphi \\ \sin\varphi\cos\varphi - 3t\sin^2\varphi\cos^2\varphi \end{pmatrix}.$$

The tangent plane at $\mathbf{R}(\varphi,t)$ is:

$$\mathbf{n}\cdot(\mathbf{F} - \mathbf{R}(\varphi,t)) = 0,$$

where $\mathbf{F} = (F_1, F_2, F_3)$ is a point on the plane.

This surface is developable (the tangent plane is constant along each generator l_φ), so we can find the plane by taking $t = 0$:

At $t = 0$, $\mathbf{R}(\varphi, 0) = (\cos\varphi, -\sin\varphi, 0)$, $\mathbf{n} = (-\cos\varphi, \sin\varphi, \sin\varphi\cos\varphi)$.

The plane equation becomes:

$$-\cos\varphi(F_1 - \cos\varphi) + \sin\varphi(F_2 + \sin\varphi) + \sin\varphi\cos\varphi(F_3 - 0) = 0.$$

Simplify:

$$-\cos\varphi F_1 + \cos^2\varphi + \sin\varphi F_2 + \sin^2\varphi + \sin\varphi\cos\varphi F_3 = 0,$$

$$-\cos\varphi F_1 + \sin\varphi F_2 + \sin\varphi\cos\varphi F_3 + 1 = 0.$$

Renaming (F_1, F_2, F_3) back to (f_1, f_2, f_3) yields the result. One may verify that for any t, the points of l_φ satisfy this equation, confirming the plane contains the line. Thus

$$-\cos\varphi\, f_1 + \sin\varphi\, f_2 + \sin\varphi\cos\varphi\, f_3 + 1 = 0$$

is the equation of the tangent plane T_φ along the generator l_φ. ■

Substituting the equation of the tangent plane into the discriminant surface and then factoring, we isolate the double factor representing a straight line. The remaining part of the intersection of the plane and the surface is a quartic plane curve. Therefore, there is also a family of quartic curves on the discriminant surface, with the following equation.

$$\begin{aligned}
&\Delta(\tan\varphi\, f_2 + \sin\varphi\, f_3 + \sec\varphi\,, f_2, f_3) \\
&= -\frac{1}{8}\sec^6\varphi\left(f_2 + f_3\cos^3\varphi + \sin\varphi\right)^2 \\
&\times\Big[32\left(1 + 4f_2^2 + f_2^4\right) + 12\left(15 + 4f_2^2\right)f_3^2 - 10f_3^4 + 24f_2f_3\left(20 + 3f_3^2\right)\cos\varphi \\
&+ \left(-64f_2^2 + 176f_3^2 - 15f_3^4\right)\cos 2\varphi + 4f_2f_3\left(-8 - 16f_2^2 + f_3^2\right)\cos 3\varphi \\
&- 2f_3^2\left(2 + 24f_2^2 + 3f_3^2\right)\cos 4\varphi - 12f_2f_3^3\cos 5\varphi - f_3^4\cos 6\varphi \\
&+ 64f_2\left(2 + 2f_2^2 + 3f_3^2\right)\sin\varphi + 32f_3\left(3 + 9f_2^2 + 2f_3^2\right)\sin 2\varphi + 192f_2f_3^2\sin 3\varphi + 32f_3^3\sin 4\varphi\Big]
\end{aligned}$$

5.2.4 Ruledness Theorem under the Affine Diagonal Condition

Theorem 5.3 (Ruledness): The generic part of discriminant surface of characteristic polynomial of matrix

$$H = \begin{bmatrix} g_1(f_1,f_2,f_3) & f_1 & f_2 \\ -f_1 & g_2(f_1,f_2,f_3) & f_3 \\ -f_2 & f_3 & g_3(f_1,f_2,f_3) \end{bmatrix}$$

is ruled, where g_1, g_2, g_3 are linear functions of parameters f_1, f_2, f_3, i.e. $g_i = a_{i,1}f_1 + a_{i,2}f_2 + a_{i,3}f_3 + b_i$. Furthermore, the discriminant surface of H is tangent developable and the associated directing curve is the curve of three multiplicity.

Theorem 5.4: When g_1, g_2, g_3 are constants numbers, the ruledness theorem is right in this special case.

Proof: Without loss of generality, we may assume $g_1 + g_2 + g_3 = 0$. Let g_1, g_2, g_3 be $-2b$, $b-k$, $b+k$, respectively. Here, b and k are variables. Thus, the characteristic polynomial is $g(\lambda) = \lambda^3 + (-3b^2 + f_1^2 + f_2^2 - (f_3^2 + k^2))\lambda + 2b^3 - b(f_1^2 + f_2^2) - 2b(f_3^2 + k^2) - k(f_1^2 - f_2^2) + 2f_1f_2f_3$. It leads that

$$\begin{cases} f_1^2 + f_2^2 = 3b^2 - 3t^2 + (f_3^2 + k^2) \\ k(f_1^2 - f_2^2) = -b^3 + 3bt^2 - 2t^3 - 3b(f_3^2 + k^2) + 2f_1f_2f_3, \end{cases} \tag{5-18}$$

where t is the repeated root in the characteristic polynomial. Thus, let f_3 be $k\sinh\eta$, then for $k > 0$ (for $k = 0$, it has been discussed as sw4),

$$\begin{cases} 2k(\cosh\frac{\eta}{2}f_1 - \sinh\frac{\eta}{2}f_2)^2 = (k\cosh\eta - (b-t))^2(k\cosh\eta - (b+2t)) \\ 2k(\sinh\frac{\eta}{2}f_1 + \cosh\frac{\eta}{2}f_2)^2 = (k\cosh\eta + (b-t))^2(k\cosh\eta + (b+2t)) \end{cases} \tag{5-19}$$

Consider special cases. when $\cosh\frac{\eta}{2}f_1 - \sinh\frac{\eta}{2}f_2 = k\cosh\eta - (b-t) = 0$, we have

$$2k((\tanh^2\frac{\eta}{2} + 1)\cosh\frac{\eta}{2}f_2)^2 = 4k^2\cosh^2\eta(3b - k\cosh\eta). \tag{5-20}$$

Then,

$$f_2^2 = (3b - k\cosh\eta)\cdot(k + k\cosh\eta). \tag{5-21}$$

It implies that

$$\begin{cases} f_1 = \pm\sqrt{(3b - k\cosh\eta)\cdot(-k + k\cosh\eta)} \\ f_2 = \pm\sqrt{(3b - k\cosh\eta)\cdot(k + k\cosh\eta)} \\ f_3 = k\sinh\eta, \end{cases} \tag{5-22}$$

where $3b \geqslant k$ and $f_1f_2f_3 \geqslant 0$.

In the same way, when when $\sinh\frac{\eta}{2}f_1+\cosh\frac{\eta}{2}f_2=k\cosh\eta+(b-t)=0$, we have

$$2k((\tanh^2\frac{\eta}{2}+1)\cosh\frac{\eta}{2}f_1)^2=4k^2\cosh^2\eta(-3b-k\cosh\eta). \tag{5-23}$$

Then,

$$f_1^2=(-3b-k\cosh\eta)\cdot(k+k\cosh\eta). \tag{5-24}$$

It implies that

$$\begin{cases} f_2=\pm\sqrt{(-3b-k\cosh\eta)\cdot(-k+k\cosh\eta)} \\ f_1=\pm\sqrt{(-3b-k\cosh\eta)\cdot(k+k\cosh\eta)} \\ f_3=k\sinh\eta, \end{cases} \tag{5-25}$$

where $-3b\geqslant k$ and $f_1f_2f_3\leqslant 0$.

For general cases, let $k\cosh\eta-(b+2t)$ be $2k\cosh\eta\cdot\sin^2\theta$, then $t=\frac{1}{2}(k\cosh\eta\cos(2\theta)-b)$. Thus,

$$\begin{cases} \cosh\frac{\eta}{2}f_1-\sinh\frac{\eta}{2}f_2=(k\cosh\eta-(b-t))\sqrt{\cosh\eta}\cdot\sin\theta \\ \sinh\frac{\eta}{2}f_1+\cosh\frac{\eta}{2}f_2=(k\cosh\eta+(b-t))\sqrt{\cosh\eta}\cdot\cos\theta \end{cases} \tag{5-26}$$

Thus, we give equations on f_1, f_2 and f_3 as follows.

$$\begin{cases} f_1=k\sqrt{\cosh\eta}(\sin\theta\cosh\frac{\eta}{2}+\cos\theta\sinh\frac{\eta}{2})-\frac{3b-k\cosh\eta\cos(2\theta)}{2\sqrt{\cosh\eta}}(\sin\theta\cosh\frac{\eta}{2}-\cos\theta\sinh\frac{\eta}{2}) \\ f_2=k\sqrt{\cosh\eta}(\cos\theta\cosh\frac{\eta}{2}-\sin\theta\sinh\frac{\eta}{2})+\frac{3b-k\cosh\eta\cos(2\theta)}{2\sqrt{\cosh\eta}}(\cos\theta\cosh\frac{\eta}{2}+\sin\theta\sinh\frac{\eta}{2}) \\ f_3=k\sinh\eta \end{cases} \tag{5-27}$$

Let $\frac{\cosh\frac{\eta}{2}}{\sqrt{\cosh\eta}}=\cos\alpha$ and $\frac{\sinh\frac{\eta}{2}}{\sqrt{\cosh\eta}}=\sin\alpha$, then

$$\begin{cases} f_1=k\sec(2\alpha)\sin(\theta+\alpha)-\frac{3b-k\sec(2\alpha)\cos(2\theta)}{2}\sin(\theta-\alpha) \\ f_2=k\sec(2\alpha)\cos(\theta+\alpha)+\frac{3b-k\sec(2\alpha)\cos(2\theta)}{2}\cos(\theta-\alpha) \\ f_3=k\tan(2\alpha) \end{cases} \tag{5-28}$$

Let θ be $\theta+\alpha$, then

$$\begin{cases} f_1=k\sec(2\alpha)\sin(\theta+2\alpha)-\frac{3b-k\sec(2\alpha)\cos(2\theta+2\alpha)}{2}\sin\theta \\ f_2=k\sec(2\alpha)\cos(\theta+2\alpha)+\frac{3b-k\sec(2\alpha)\cos(2\theta+2\alpha)}{2}\cos\theta \\ f_3=k\tan(2\alpha) \end{cases} \tag{5-29}$$

From the trigonometric addition formulas，we obtain

$$\begin{cases} f_1 = k\sin\theta + f_3\cos\theta - \dfrac{3b - k\cos(2\theta) + f_3\sin(2\theta)}{2}\sin\theta \\ f_2 = k\cos\theta - f_3\sin\theta + \dfrac{3b - k\cos(2\theta) + f_3\sin(2\theta)}{2}\cos\theta \\ f_3 = f_3 \end{cases} \tag{5-30}$$

Rearranging, we obtain

$$\begin{cases} f_1 = \dfrac{3b}{2} + \dfrac{k\sin\theta}{2}(2 + \cos(2\theta)) + f_3\cos^3\theta \\ f_2 = \dfrac{3b}{2} + \dfrac{k\cos\theta}{2}(2 - \cos(2\theta)) - f_3\sin^3\theta \\ f_3 = f_3 \end{cases} \tag{5-31}$$

Note that for $k < 0$,

$$\begin{cases} -2k(\sinh\dfrac{\eta}{2}f_1 + \cosh\dfrac{\eta}{2}f_2)^2 = (-k\cosh\eta - (b-t))^2(-k\cosh\eta - (b+2t)) \\ -2k(\cosh\dfrac{\eta}{2}f_1 - \sinh\dfrac{\eta}{2}f_2)^2 = (-k\cosh\eta + (b-t))^2(-k\cosh\eta + (b+2t)) \end{cases} \tag{5-32}$$

Thus, for general cases, it is equivalent to the case $k > 0$. For special cases, $k\cosh\eta$ changes its sign, it leads that

$$\begin{cases} f_1 = \pm\sqrt{(-3b + k\cosh\eta)\cdot(k - k\cosh\eta)} \\ f_2 = \pm\sqrt{(-3b + k\cosh\eta)\cdot(-k - k\cosh\eta)} \\ f_3 = k\sinh\eta, \end{cases} \tag{5-33}$$

where $-3b \geqslant -k$ and $f_1 f_2 f_3 \geqslant 0$ and that

$$\begin{cases} f_2 = \pm\sqrt{(3b + k\cosh\eta)\cdot(k - k\cosh\eta)} \\ f_1 = \pm\sqrt{(3b + k\cosh\eta)\cdot(-k - k\cosh\eta)} \\ f_3 = k\sinh\eta, \end{cases} \tag{5-34}$$

where $3b \geqslant -k$ and $f_1 f_2 f_3 \leqslant 0$.

Define the sign function

$$\mathrm{sign}(x) = \begin{cases} 1 & \text{if } x > 0, \\ 0 & \text{if } x = 0, \\ -1 & \text{if } x < 0, \end{cases}$$

then we have

$$\begin{cases} f_{\frac{3-\mathrm{sign}(kb)}{2}} = \pm\,\mathrm{sign}(b)\sqrt{\dfrac{\mathrm{sign}(kb)\cdot 3b - k\cosh\eta}{k + k\cosh\eta}}\cdot k\sinh\eta \\ f_{\frac{3+\mathrm{sign}(kb)}{2}} = \pm\sqrt{(k + k\cosh\eta)(\mathrm{sign}(kb)\cdot 3b - k\cosh\eta)} \\ f_3 = k\sinh\eta \end{cases} \tag{5-35}$$

for $k, b \neq 0$ and $|k| \leqslant 3|b|$.

Note that for special cases and for distinct b and k, the curve always can be represented by one of the above equations.

When $f_3 = 0$, $f_{\frac{3-\mathrm{sign}(kb)}{2}} = 0$ and $f_{\frac{3+\mathrm{sign}(kb)}{2}} = \pm\sqrt{2k(\mathrm{sign}(kb)\cdot 3b - k)}$

■

After settling the case where the Hamiltonian matrix has constant diagonal entries, we can now tackle the more general situation with linear functions on the diagonal using the method of variation of constants.

Proof of Theorem 5.3: Notice in formula (A) that each component f_i can be expressed as a linear combination of k and b with trigonometric coefficients, namely

$$\begin{bmatrix} f_1 \\ f_2 \\ f_3 \end{bmatrix} = \begin{bmatrix} \frac{1}{4}\sec(2\alpha)\big(3\sin(\theta+\alpha) + \sin(3\theta-\alpha)\big) & -\frac{3}{2}\sin(\theta-\alpha) \\ \frac{1}{4}\sec(2\alpha)\big(3\cos(\theta+\alpha) - \cos(3\theta-\alpha)\big) & \frac{3}{2}\cos(\theta-\alpha) \\ \tan(2\alpha) & 0 \end{bmatrix} \begin{bmatrix} k \\ b \end{bmatrix}. \tag{5-36}$$

Denote the above 3×2 matrix of trigonometric functions by A.

We now introduce a variation of k, b that also contains a linear part in f_1, f_2, f_3:

$$\begin{cases} k = c_{11}f_1 + c_{12}f_2 + c_{13}f_3 + c_k, \\ b = c_{21}f_1 + c_{22}f_2 + c_{23}f_3 + c_b, \end{cases} \quad \text{or equivalently} \quad \begin{bmatrix} k \\ b \end{bmatrix} = C\begin{bmatrix} f_1 \\ f_2 \\ f_3 \end{bmatrix} + \begin{bmatrix} c_k \\ c_b \end{bmatrix},$$

where

$$C = \begin{bmatrix} c_{11} & c_{12} & c_{13} \\ c_{21} & c_{22} & c_{23} \end{bmatrix}.$$

The Hamiltonian is given in the form

$$H = \begin{bmatrix} g_1(f_1, f_2, f_3) & f_1 & f_2 \\ -f_1 & g_2(f_1, f_2, f_3) & f_3 \\ -f_2 & f_3 & g_3(f_1, f_2, f_3) \end{bmatrix}.$$

Since adding a constant multiple of the identity to H does not alter the geometry of its degeneracy surfaces, we may subtract $\left(\frac{g_1 + g_2 + g_3}{3}\right) \cdot I$ to make the trace zero. Setting the trace to zero forces new diagonal entries g_i' satisfying $g_1' + g_2' + g_3' = 0$. A convenient choice satisfying this condition is

$$g_1' = -2b, \qquad g_2' = b - k, \qquad g_3' = b + k.$$

Each g_i is originally an affine function of f_1, f_2, f_3, say

$$g_i = a_{i1} f_1 + a_{i2} f_2 + a_{i3} f_3 + b_i.$$

From the relations $g_1' = -2b,\ g_2' = b - k,\ g_3' = b + k$ together with the expression of k, b in terms of f_1, f_2, f_3, we can determine the coefficients $c_{ij},\ c_k,\ c_b$.

$$c_{11} = \frac{a_{31} - a_{21}}{2}, \quad c_{12} = \frac{a_{32} - a_{22}}{2}, \quad c_{13} = \frac{a_{33} - a_{23}}{2},$$
$$c_{21} = -\frac{1}{2}\left(a_{11} - \frac{a_{11} + a_{21} + a_{31}}{3}\right),$$
$$c_{22} = -\frac{1}{2}\left(a_{12} - \frac{a_{12} + a_{22} + a_{32}}{3}\right),$$
$$c_{23} = -\frac{1}{2}\left(a_{13} - \frac{a_{13} + a_{23} + a_{33}}{3}\right),$$
$$c_k = \frac{b_3 - b_2}{2}, \quad c_b = -\frac{1}{2}\left(b_1 - \frac{b_1 + b_2 + b_3}{3}\right).$$

Substituting the expression of k, b into (A) gives

$$\begin{bmatrix} f_1 \\ f_2 \\ f_3 \end{bmatrix} = A\left(C \begin{bmatrix} f_1 \\ f_2 \\ f_3 \end{bmatrix} + \begin{bmatrix} c_k \\ c_b \end{bmatrix}\right) = AC \begin{bmatrix} f_1 \\ f_2 \\ f_3 \end{bmatrix} + A \begin{bmatrix} c_k \\ c_b \end{bmatrix}.$$

Solving this linear system yields

$$\begin{bmatrix} f_1 \\ f_2 \\ f_3 \end{bmatrix} = (I - AC)^{-1} A \begin{bmatrix} c_k \\ c_b \end{bmatrix}.$$

Using the matrix identity $(I - AC)^{-1}A = A(I - CA)^{-1}$ (valid when the inverses

exist), the right-hand side can be rewritten as

$$A\,(I - CA)^{-1}\begin{bmatrix} c_k \\ c_b \end{bmatrix},$$

which involves inverting only the 2×2 matrix $I - CA$ and thereby simplifies the computation. ■

5.3 Conics on the Sextic Surface

Enumerative geometry is characterized by its fundamental question: "How many" geometric objects of a specific type satisfy given conditions? Any valid answer must be a natural number.

Theorem 5.5 (27 Lines on a Smooth Cubic Surface): Let S be a smooth cubic surface in the complex projective space $\mathbb{P}^3$. The surface S contains exactly 27 distinct lines. Each of these lines intersects exactly 10 of the others. The configuration of these 27 lines is independent of the specific smooth cubic surface S; it is determined up to isomorphism by the following incidence relations: 30 points where three lines meet (trihedral points); 45 planes, each containing exactly three of the lines (trihedral planes).

Theorem 5.6 (3264 Conics Tangent to Five Conics): Let C_1, C_2, C_3, C_4, C_5 be five smooth conics in general position in the complex projective plane $\mathbb{P}^2$. The number of distinct smooth conics in $\mathbb{P}^2$ that are tangent to all five given conics is precisely 3264.

Remark 5.3: The restriction condition "general position" is a technical condition meaning the conics are chosen to avoid degenerate situations where the number of tangent conics would be infinite or where the intersection calculation would be incorrect due to non-transversality. And tangent means the conic meets the given conic at a point with intersection multiplicity at least 2.

Remark 5.4: Historical context: This result corrects an earlier, naive calculation by J. Steiner (1848), who argued that since the condition of tangency to a conic is of degree 6, the number of solutions should be $6^5 = 7776$. The correct number, **3264**, accounts for the contribution of degenerate conics (like double lines) in a compactified moduli space of conics, a resolution achieved in the 19th century by geometers including Chasles, de Jonquières, and Zeuthen.

From the example above, we can see that degeneracy is a crucial factor when counting conics. The properties of smooth conics and degenerate conics are often fundamentally different and must be treated separately. In the sextic algebraic surface we are study-

ing, since it is a ruled surface, it contains infinitely many lines. Moreover, two intersecting lines can form a plane, and the pair of intersecting lines in that plane constitutes a degenerate conic. Consequently, on our discriminant surface, there are infinitely many degenerate conics, but smooth conics are extremely rare, in a special cases, we can find three.

Proposition 5.3: For sw4 surface give by the discriminant of characteristic polynomial of matrix

$$\begin{bmatrix} 1 & f_1 & f_2 \\ -f_1 & -1 & f_3 \\ -f_2 & f_3 & -1 \end{bmatrix},$$

there are at least 3 smooth conics on it.

Proof: There are three ellipses on the surface parametrized by:

$$\begin{cases} f_1 = \cos\psi \\ f_2 = -\cos\psi \\ f_3 = 1 + \sin\psi \end{cases} \qquad \begin{cases} f_1 = \cos\psi \\ f_2 = \cos\psi \\ f_3 = -1 - \sin\psi \end{cases} \qquad \begin{cases} f_1 = \cos\varphi \\ f_2 = \sin\varphi \\ f_3 = 0 \end{cases}$$

Among these, the first two are oblate ellipses, while the third is a perfect circle. ■

5.4 Generalizations and Future Work

In this chapter, we have explored the geometric properties of the discriminant surface associated with a family of Hamiltonian matrices. We established that under the affine diagonal condition, the generic part of the discriminant surface is ruled and tangent developable, with the directing curve corresponding to points of triple multiplicity. Additionally, we identified specific families of conics on the surface, including infinitely many degenerate conics formed by intersecting lines and at least three smooth conics in special cases.

Quantization of surfaces generally refers to transforming the classical geometry and symplectic structure of the moduli space of surfaces into noncommutative algebraic structures and operator representations through quantization methods, thereby constructing the corresponding Hilbert spaces and quantum invariants. In this process, the combinatorial structure of the surface provides a foundation for coordinatization and discretization, while algebraic tools such as quantum groups and representation theory are used to characterize its quantum symmetries, particularly the representation of the mapping class group on the quantum state space.

Non-Hermitian quantum topology studies topological structures in open, dissipative, gain-loss, or nonreciprocal quantum systems where the Hamiltonian is no longer Hermitian. Core issues include the classification of complex spectra via point and line gaps, Berry phases and quantum geometry defined with biorthogonal eigenstates, exceptional points and their branch-point topology, the non-Hermitian skin effect and the resulting breakdown and reconstruction of bulk-boundary correspondence, as well as many-body non-Hermitian topology and topological responses in stochastic/Lindblad dynamics. From the perspective of mathematical physics, it connects to K-theory, homotopy classification, spectral theory of non-normal operators, complex analytic geometry, singularity theory, and non-Bloch band theory. Experimentally, relevant platforms include photonic lattices, cold atoms, electrical circuits, and mechanical/acoustic metamaterials. A key recent trend is to treat non-Hermiticity itself as a source of topology—rather than merely a perturbation of Hermitian topology—focusing in particular on unified frameworks linking exceptional points, the skin effect, and point-gap topology, together with their experimental controllability.

CONCLUSION

The core innovations of this dissertation are as follows:

（1）We investigate the relationship between the closed geodesic system and the homology groups of the real moment-angle complex surfaces $Z(C_n,(D^1,S^0))$. By restricting the Hurewicz map to the free abelian group generated by the systoles (shortest closed geodesics), we construct a standard basis for the kernel of this map. The vectors in this basis are in one-to-one correspondence with the nonempty independent sets of the cycle graph C_n.

（2）Using combinatorial enumeration methods, we derive explicit formulas for the ranks of the kernel and the image of the Hurewicz map. These formulas are precisely expressed in terms of the Lucas numbers $L(n)$. Furthermore, by analyzing orbit counts under the action of cyclic groups, we obtain number-theoretic identities involving the Möbius function, the Euler totient function, and the Lucas numbers.

（3）We extend the problem of studying the homological relations of closed geodesics on closed surfaces to the broader context of regular maps. For the regular embeddings of the hypercube graph Q_n , we perform computations for even n up to 18 and propose a new conjecture regarding the rank of the closed geodesic homology.

（4）We reveal a connection between the Morse index of the systole function and the combinatorial structure of the surface. Endowing the surface with the standard hyperbolic metric, we compute the Morse index of the systole function for $n = 5$ to 13.

（5）We study the geometric structures that arise as critical surfaces in non-Hermitian quantum mechanics. We prove that, under an affine parameter condition, these surfaces are algebraic ruled surfaces equipped with a flat metric.

Future directions for further research in this area include the following:

（1）One question arising from Chapter 2 is whether the cokernel group contains torsion. In principle, one can write down the edges corresponding to each homology class by using the stable decomposition theorem, then compare them directly with the edges represented by geodesics, and finally compute the rank via the Smith normal form algorithm. It is also natural to ask whether the subgroup generated by these systolic geodesics has any homotopy-theoretic significance. After suspension, the systoles become spheres, and it would be worth understanding how this phenomenon can be incorporated into the

language and framework of homotopy theory.

（2）Another direction is to generalize the notion of independent sets in the context of polyhedral products. In particular, one may ask: what should the analogue of geodesics be in the case of complex moment-angle complexes?

（3）It is also natural to ask whether there exist suitable analogues of Fenchel–Nielsen coordinates in our setting. Although maximal independent sets cut the surface into certain basic pieces, they do not yield a canonical pants decomposition. Moreover, if one forcibly decomposes the surface into pairs of pants, the existing cell structure is inevitably destroyed. It would therefore be desirable to find a system of coordinates on Teichmüller space that is more natural for our setting and uses fewer parameters than the current description in terms of the edge lengths and angles of each piece.

（4）More generally, our current work only studies the shortest geodesics and their length functions. In fact, one may consider geodesics of arbitrary length, that is, the full length spectrum. Because of the nature of hyperbolic geometry, the multiplicity of geodesics of a given length is unbounded as the length increases. This suggests introducing a filtration by geodesic length and studying how the size of the kernel of the Hurewicz map changes as the length bound grows.

（5）There are also some intriguing numerical coincidences. The genus of the surface $Z(C_n, (D^1, S^0))$ studied here coincides with the genus of the thickened surface associated with an embedding of the cube graph Q_{n-3} in three-dimensional space. It is natural to ask whether there is any deeper connection between them. Likewise, the regular embeddings corresponding to the N-S solutions $M(n+1,-1)$ and $M(n,1)$ for the cube graph Q_{n-3} have the same genus. Is there a natural way to relate them? What is the distance between these two points in Teichmüller space? Is there a natural path connecting them? If such a path exists, do the surfaces along it possess any special geometric properties? Finally, how are the geodesic systems on these surfaces related to the geodesic system on the surface studied in this thesis?

（6）We can study the symmetric groups of the surfaces and the action of the tangent space of Teichmüller space. This may provide a new perspective on the relationship between the geometry of the surface and its combinatorial structure.

APPENDIX A HYPERBOLIC GEOMETRY TRIGONOMETRY

Choice of Hyperbolic Geometry Model

The hyperbolic plane (curvature -1) has several classical models: the Poincaré disk, the upper half-plane, the hyperboloid model, and the Klein model. When deriving trigonometric formulas, the **hyperboloid model** is the most concise because it transforms geometric problems into linear algebra problems. References can be found in[39,74], and there are numerous textbooks that prove these theorems using other models, such as[18,27,38].

Next, the hyperbolic plane is realized as one sheet of a two-sheeted hyperboloid in three-dimensional Minkowski space.

Consider the Lorentzian inner product on $\mathbb{R}^{2,1}$ (Minkowski space):

$$\langle x, y\rangle_L = -x_0y_0 + x_1y_1 + x_2y_2. \tag{A-1}$$

The hyperbolic plane $\mathbb{H}^2$ is defined as the upper sheet of the hyperboloid, or understood as a sphere with radius equal to the imaginary unit i:

$$\mathbb{H}^2 = \{x \in \mathbb{R}^{2,1} : \langle x, x\rangle_L = -1,\ x_0 > 0\}. \tag{A-2}$$

The characteristic of this model is that geodesics are simple and geometrically intuitive: Geodesics are the intersections of the hyperboloid with two-dimensional planes passing through the origin (i.e., hyperbolas or straight lines). This description is very direct in its analogy to "great circles" in spherical geometry: great circles on a sphere are intersections of the sphere with planes through the sphere's center; geodesics on the hyperboloid are intersections of the hyperboloid with timelike or lightlike planes through the origin.

The isometry group of the hyperboloid is the branch of the Lorentz group $\mathrm{O}(2,1)$ that preserves time orientation, $\mathrm{SO}^+(2,1)$. The hyperbolic distance formula can be directly given by the Minkowski inner product:

Lemma A.1 (Distance Formula): For any $u, v \in \mathbb{H}^2$,

$$\boxed{\cosh d(u,v) = -\langle u, v\rangle_L}. \tag{A-3}$$

Remark A.1: This perfectly mirrors the distance formula in spherical geometry:

$\cos d(u,v) = \langle u, v\rangle,\ \forall u, v \in S^2$, where the inner product is the Euclidean inner product.

Definition A.1 (Tangent Space and Angle): The tangent space at a point $A \in \mathbb{H}^2$ is

$$T_A\mathbb{H}^2 = \{w : \langle w, A\rangle_L = 0\}. \tag{A-4}$$

The angle between two geodesics at A is defined as the angle between their tangent vectors in the Riemannian metric induced on this tangent space. Note that in the hyperboloid model, when drawing two intersecting geodesics (hyperbolas), the hyperbolic angle at their intersection is defined by the Minkowski metric and does not coincide with the visual angle defined by the Euclidean metric in three-dimensional Euclidean space.

Law of Cosines for Sides (SSS)

Theorem A.1 (Law of Cosines for Sides): In a hyperbolic triangle $\triangle ABC$, let $a = d(B,C)$, $b = d(C,A)$, $c = d(A,B)$, and $\alpha = \angle A$. Then

$$\boxed{\cosh a = \cosh b \cosh c - \sinh b \sinh c \cos\alpha.} \tag{SSS}$$

Proof: Using $O(2,1)$ isometries, place the triangle in a standard position:

(1)First, set $A = (1, 0, 0)$.

(2)Place B in the plane $x_2 = 0$. From $d(A,B) = c$ and the distance formula (A-3), we can take

$$B = (\cosh c,\ \sinh c,\ 0).$$

(3)Place C at an angle α from AB. From $d(A,C) = b$ and rotational symmetry, we can take

$$C = (\cosh b,\ \sinh b\cos\alpha,\ \sinh b \sin\alpha).$$

Verification: $\langle A, A\rangle_L = \langle B, B\rangle_L = \langle C, C\rangle_L = -1$, and $\langle A, B\rangle_L = -\cosh c$, $\langle A, C\rangle_L = -\cosh b$. From the distance formula (A-3):

$$\cosh a = -\langle B, C\rangle_L. \tag{A-5}$$

Compute the inner product:

$$\begin{aligned}\langle B, C\rangle_L &= -(\cosh c)(\cosh b) + (\sinh c)(\sinh b\cos\alpha) + 0\cdot(\sinh b\sin\alpha)\\ &= -\cosh b\cosh c + \sinh b\sinh c\cos\alpha.\end{aligned} \tag{A-6}$$

Therefore,

$$\cosh a = -\langle B, C\rangle_L = \cosh b\cosh c - \sinh b\sinh c\cos\alpha. \tag{A-7}$$

Cyclic permutation yields the other two formulas. ■

Law of Sines

Theorem A.2 (Law of Sines): In a hyperbolic triangle $\triangle ABC$,

$$\boxed{\frac{\sin\alpha}{\sinh a} = \frac{\sin\beta}{\sinh b} = \frac{\sin\gamma}{\sinh c}}. \qquad \text{(Sine)}$$

Proof: Let $A, B, C \in \mathbb{H}^2 \subset \mathbb{R}^{2,1}$ be the vertices of the hyperbolic triangle, satisfying $\langle A, A\rangle = \langle B, B\rangle = \langle C, C\rangle = -1$. Denote the side lengths as $a = d(B, C)$, $b = d(C, A)$, $c = d(A, B)$, and the opposite angles as $\alpha = \angle A$, $\beta = \angle B$, $\gamma = \angle C$.

In $\mathbb{R}^{2,1}$, define the generalized cross product $X \times Y$ as the unique vector satisfying:

- $\langle X \times Y, X\rangle = \langle X \times Y, Y\rangle = 0$,
- $\langle X \times Y, X \times Y\rangle = \sinh^2 d(X, Y)$,

Define the scalar triple product

$$\Delta = \det(A, B, C) = \langle A, B \times C\rangle,$$

where the determinant is computed with respect to an orthonormal basis.

Using determinant identities, Δ^2 can be computed:

$$\Delta^2 = \det\begin{pmatrix} \langle A, A\rangle & \langle A, B\rangle & \langle A, C\rangle \\ \langle B, A\rangle & \langle B, B\rangle & \langle B, C\rangle \\ \langle C, A\rangle & \langle C, B\rangle & \langle C, C\rangle \end{pmatrix}.$$

Substitute $\langle A, A\rangle = \langle B, B\rangle = \langle C, C\rangle = -1$, $\langle A, B\rangle = -\cosh c$, $\langle A, C\rangle = -\cosh b$, $\langle B, C\rangle = -\cosh a$. Factor out a negative sign from each row (three rows give a factor $(-1)^3 = -1$):

$$\Delta^2 = -\det\begin{pmatrix} 1 & \cosh c & \cosh b \\ \cosh c & 1 & \cosh a \\ \cosh b & \cosh a & 1 \end{pmatrix}.$$

This determinant can be simplified to

$$\det = 1 + 2\cosh a \cosh b \cosh c - \cosh^2 a - \cosh^2 b - \cosh^2 c = \sinh^2 b \, \sinh^2 c \, \sin^2 \alpha.$$

(The last equality can be verified using the hyperbolic law of cosines $\cosh a = \cosh b \cosh c - \sinh b \sinh c \cos\alpha$.) Therefore,

$$\Delta^2 = \sinh^2 b \, \sinh^2 c \, \sin^2 \alpha,$$

i.e.,

$$|\Delta| = \sinh b \ \sinh c \ \sin \alpha.$$

Taking a specific coordinate representation also verifies the above formula. For example, set

$$A = \begin{pmatrix} 1 \\ 0 \\ 0 \end{pmatrix}, \quad B = \begin{pmatrix} \cosh c \\ \sinh c \\ 0 \end{pmatrix}, \quad C = \begin{pmatrix} \cosh b \\ \sinh b \cos \alpha \\ \sinh b \sin \alpha \end{pmatrix},$$

and compute $\det(A, B, C)$ directly to obtain

$$\Delta = \sinh b \ \sinh c \ \sin \alpha.$$

Since the determinant is antisymmetric, its absolute value remains unchanged under cyclic permutation of vertices:

$$|\langle A, B \times C \rangle| = |\langle B, C \times A \rangle| = |\langle C, A \times B \rangle|.$$

Compute the other two expressions: $|\langle B, C \times A \rangle| = \sinh c \ \sinh a \ \sin \beta$ and $|\langle C, A \times B \rangle| = \sinh a \ \sinh b \ \sin \gamma$. Thus, we obtain:

$$\sinh b \ \sinh c \ \sin \alpha = \sinh c \ \sinh a \ \sin \beta = \sinh a \ \sinh b \ \sin \gamma.$$

Dividing all three expressions by $\sinh a \ \sinh b \ \sinh c$ yields

$$\frac{\sin \alpha}{\sinh a} = \frac{\sin \beta}{\sinh b} = \frac{\sin \gamma}{\sinh c}.$$

■

Law of Cosines for Angles (AAA)

Theorem A.3 (Law of Cosines for Angles): In a hyperbolic triangle $\triangle ABC$,

$$\boxed{\cos \alpha = -\cos \beta \cos \gamma + \sin \beta \sin \gamma \cosh a}. \qquad \text{(AAA)}$$

Proof: The following uses the polar triangle duality method to directly transform the law of cosines for sides into the law of cosines for angles.

For triangle ABC, define: n_a as the unit normal vector to side BC (also called the polar vector of the side), n_b as the unit normal vector to side CA, and n_c as the unit normal vector to side AB. Treat these normal vectors as points $A^* = n_a$, $B^* = n_b$, $C^* = n_c$, called the polar triangle $A^*B^*C^*$ of the original triangle. Although these points lie on the de Sitter surface, they algebraically serve as dual objects, where lengths and angles

naturally become complex, interchanging the relationships between sides and angles.

The angles of the original triangle correspond to the sides of the polar triangle. Specifically, the angle A at vertex A equals the angle between the normal vectors n_b and n_c, i.e., $\langle n_b, n_c \rangle_L = \cos A$. If B^* and C^* are treated as points, their hyperbolic distance satisfies $\cosh(B^*C^*) = -\langle n_b, n_c \rangle_L = -\cos A$. Using the identity $\cosh(i(\pi - A)) = \cos(\pi - A) = -\cos A$, we obtain:

$$B^*C^* = i(\pi - A), \quad C^*A^* = i(\pi - B), \quad A^*B^* = i(\pi - C). \tag{D1}$$

On the other hand, the sides of the original triangle correspond to the angles of the polar triangle. Consider the angle $\angle C^*$ at vertex C^* of the polar triangle. Its relationship with the original side $c = |AB|$ is $\cos(\angle C^*) = -\cosh c$. Since $\cos(\pi - ic) = -\cos(ic) = -\cosh c$, we have:

$$\angle C^* = \pi - ic, \quad \angle A^* = \pi - ia, \quad \angle B^* = \pi - ib. \tag{D2}$$

Now, apply the law of cosines for sides to the polar triangle $A^*B^*C^*$:

$$\cosh(A^*B^*) = \cosh(B^*C^*)\cosh(C^*A^*) - \sinh(B^*C^*)\sinh(C^*A^*)\cos(\angle C^*). \quad (*)$$

Substitute the dual relationships term by term. First, from (D1), the left-hand side is $\cosh(A^*B^*) = \cosh(i(\pi - C)) = \cos(\pi - C) = -\cos C$. In the first term on the right, $\cosh(B^*C^*) = \cosh(i(\pi - A)) = \cos(\pi - A) = -\cos A$, and similarly $\cosh(C^*A^*) = -\cos B$, so their product is $\cos A \cos B$. In the second term on the right, $\sinh(B^*C^*) = \sinh(i(\pi - A)) = i\sin(\pi - A) = i\sin A$, and similarly $\sinh(C^*A^*) = i\sin B$, while $\cos(\angle C^*) = \cos(\pi - ic) = -\cosh c$. After simplification, this yields the law of cosines for angles:

$$\cos C = -\cos A \cos B + \sin A \sin B \cosh c. \tag{HAL}$$

Similarly, by cyclic permutation, the corresponding formulas for angles A and B can be obtained. ■

Special Case: Right Triangles

Corollary A.1 (Hyperbolic Pythagorean Theorem): If $\gamma = \pi/2$, then

$$\boxed{\cosh c = \cosh a \cosh b}. \tag{A-8}$$

Proof: Set $\gamma = \pi/2$ in the law of cosines for sides (SSS) to obtain $\cosh c = \cosh a \cosh b - \sinh a \sinh b \cdot 0 = \cosh a \cosh b$. ■

Corollary A.2 (Trigonometric Functions for Acute Angles): In a right triangle with $\gamma = \pi/2$,

$$\boxed{\sin\alpha = \frac{\sinh a}{\sinh c}, \qquad \sin\beta = \frac{\sinh b}{\sinh c}}. \tag{A-9}$$

Proof: Directly obtained from the law of sines (Sine) with $\sin\gamma = 1$. ■

Corollary A.3 (Tangent Relationships):

$$\boxed{\cos\alpha = \tanh b \coth c, \qquad \cos\beta = \tanh a \coth c}. \tag{A-10}$$

Proof: Obtained by combining the law of cosines for sides (SSS) and the Pythagorean theorem and eliminating terms. ■

Comparison Table of Three Types of Geometry

Table A-1 Comparison of trigonometric formulas in hyperbolic, spherical, and Euclidean geometry

Theorem	**Hyperbolic ($K = -1$)**	**Spherical ($K = 1$)**	**Euclidean ($K = 0$)**
Law of cosines (sides)	$\cosh a = \cosh b \cosh c - \sinh b \sinh c \cos\alpha$	$\cos a = \cos b \cos c + \sin b \sin c \cos\alpha$	$a^2 = b^2 + c^2 - 2bc\cos\alpha$
Law of sines	$\frac{\sin\alpha}{\sinh a} = \frac{\sin\beta}{\sinh b} = \frac{\sin\gamma}{\sinh c}$	$\frac{\sin\alpha}{\sin a} = \frac{\sin\beta}{\sin b} = \frac{\sin\gamma}{\sin c}$	$\frac{\sin\alpha}{a} = \frac{\sin\beta}{b} = \frac{\sin\gamma}{c}$
Law of cosines (angles)	$\cos\alpha = -\cos\beta\cos\gamma + \sin\beta\sin\gamma\cosh a$	$\cos\alpha = -\cos\beta\cos\gamma + \sin\beta\sin\gamma\cos a$	$\alpha + \beta + \gamma = \pi$
Pythagorean theorem	$\cosh c = \cosh a \cosh b$	$\cos c = \cos a \cos b$	$c^2 = a^2 + b^2$

APPENDIX B ALGORITHM AND COMPUTATIONAL IMPLEMENTATION

B.1 Recursive construction and rendering of the decorated planar diagram for the dual map of the hypercube graph embedding

We now describe the recursive construction of the decorated planar diagram $\mathcal{D}_n$. The construction is based on a family of axis-aligned rectangular loops generated recursively from a basic square. For each integer $n \geq 4$, let $\mathcal{F}_n$ denote the family of closed rectangular loops produced at level n. Let RectVertexSet be the set of all rectangle vertices appearing in $\mathcal{F}_n$. Among all intersections of horizontal and vertical segments in $\mathcal{F}_n$, we distinguish two types: the set NodeSet of midpoint-type intersections, and the set CrossingSet of all remaining non-corner intersections. The final rendered planar diagram is denoted by $\mathcal{D}_n$.

For clarity, the construction of $\mathcal{D}_n$ is divided into three stages. First, Algorithm B-1 recursively generates the rectangular loop family $\mathcal{F}_n$ from the initial square at level $n = 4$ by horizontal translation, vertical scaling, and quarter-turn rotation. Next, Algorithm B-2 extracts all horizontal and vertical segments in $\mathcal{F}_n$ and classifies their intersections into rectangle corners, nodes, and ordinary crossings. Finally, Algorithm B-4 renders the planar diagram by drawing the rectangular skeleton, assigning the prescribed local decorations to distinguished points, and adding the auxiliary axis-centered marks.

In this way, the recursive procedure first constructs the global rectangular framework $\mathcal{F}_n$, then identifies its distinguished intersection sets, and finally converts this geometric-combinatorial data into the decorated planar diagram $\mathcal{D}_n$. The global shape of $\mathcal{D}_n$ is therefore determined recursively, whereas its local structure is encoded by the corner, node, and crossing rules used in the rendering stage.

B.2 Homological redundancy calculation in the dual maps of hypercube graph embeddings

```
1 import itertools
2 import numpy as np
3
```

Algorithm B-1 Recursive construction of the rectangular loop family $\mathcal{F}_n$

Data: integer $n \geq 4$, base half-side length $a > 0$
Result: a family $\mathcal{F}_n$ of closed axis-aligned rectangular loops

Function `Build`(n, a)
  if $n = 4$ **then**
    return the square centered at the origin with vertices $(-a,-a), (a,-a), (a,a), (-a,a)$ and then returning to $(-a,-a)$;
  else
    $\mathcal{F}_{n-1} \leftarrow$ `Build`$(n-1, a)$;
    $\delta \leftarrow 2^{n-4}a$;
    initialize $\mathcal{U} \leftarrow \emptyset$;
    foreach $C \in \mathcal{F}_{n-1}$ **do**
      add `Translate`$(C, (-\delta, 0))$ and `Translate`$(C, (\delta, 0))$ to $\mathcal{U}$;
    end
    foreach $C \in \mathcal{U}$ **do**
      replace every point $(x, y) \in C$ by $(x, 2y)$;
    end
    initialize $\mathcal{V} \leftarrow \emptyset$;
    foreach $C \in \mathcal{U}$ **do**
      add `Rotate90`(C) to $\mathcal{V}$; // $(x, y) \mapsto (-y, x)$
    end
    return $\mathcal{U} \cup \mathcal{V}$;
  end

```python
class GeodesicAnalyzer:
    def __init__(self, m):
        self.m = m
        self.num_edges = m * (1 << (m-1))  # m * 2^(m-1)
        self.d2 = self.build_d2_sparse()

    def edge_index(self, i, bits):
        """Calculate edge index, i is the position of *, bits
           is the binary combination of other positions"""
        return i * (1 << (self.m-1)) + bits

    def build_d2_sparse(self):
        """Construct sparse matrix for d2 boundary operator,
           each row corresponds to boundary edges of a face"""
        d2 = []
        for surface in itertools.product([0, 1], repeat=self.m)
           :
            row = []
```

Algorithm B-2 Intersection classification in the rectangular loop family

Data: rectangular loop family $\mathcal{F}_n$
Result: RectVertexSet, NodeSet, and CrossingSet
extract all horizontal segments into $\mathcal{H}$ and all vertical segments into $\mathcal{V}$;
initialize RectVertexSet $\leftarrow \emptyset$;
initialize NodeSet $\leftarrow \emptyset$ and CrossingSet $\leftarrow \emptyset$;
foreach *loop* $C \in \mathcal{F}_n$ **do**
    add all vertices of C, except the repeated final point, to RectVertexSet;
end
foreach *vertical segment* $(x_v, y_1, y_2) \in \mathcal{V}$ **do**
    foreach *horizontal segment* $(y_h, x_1, x_2) \in \mathcal{H}$ **do**
        if $x_v \in [x_1, x_2]$ *and* $y_h \in [y_1, y_2]$ **then**
            let $p = (x_v, y_h)$;
            if p *is simultaneously an endpoint of the horizontal segment and an endpoint of the vertical segment* **then**
                continue ; // rectangle corner
            else if $x_v = \frac{x_1 + x_2}{2}$ *and* $y_h = \frac{y_1 + y_2}{2}$ **then**
                add p to NodeSet;
            else
                add p to CrossingSet;
            end
        end
    end
end
remove duplicate points from all three sets and sort them lexicographically;

Algorithm B-3 Local decoration rules

Data: point type and local orientation
Result: drawing instruction around the point
Procedure *Corner decoration at a point* p *with orientation in* {LU, RU, LD, RD}
    draw a white square neighborhood centered at p;
    draw three concentric quarter-circular arcs of radii $1, 2, 3$;
    use the color pattern red–black–red according to the corner orientation;
Procedure *Node decoration at a point* p
    draw a white square neighborhood centered at p;
    draw four red quarter-circular arcs around the local block;
    draw one horizontal black segment and one vertical black segment crossing at p;
    draw a blue solid dot at p;
Procedure *Crossing decoration at a point* p
    draw a white square neighborhood centered at p;
    declare the horizontal branch to pass over the vertical branch;
    draw a central horizontal black segment through p;
    draw two short vertical black stubs above and below p;
    draw two parallel red horizontal segments and four short red vertical side stubs;

Algorithm B-4 Rendering of the decorated planar diagram $\mathcal{D}_n$

Data: integer $n \geq 4$, base half-side length a, optional output path
Result: decorated planar diagram $\mathcal{D}_n$

$\mathcal{F}_n \leftarrow$ Algorithm B-1 applied to (n, a);
compute RectVertexSet, NodeSet, and CrossingSet by Algorithm B-2;
extract from each loop its bounding rectangle and determine the orientation of each corner;
compute the line width

$$w_n = \max\{0.30,\ 2.4 \cdot 0.65^{\,n-5}\};$$

compute the auxiliary coordinate set

$$\mathcal{Y}_n = \{\pm 4(2k+1) : 0 \leq k \leq 2^{\,n-4} - 1\};$$

initialize a square canvas with equal aspect ratio and no visible axes;
determine a square viewing window containing all rectangles, decorations, and auxiliary points;

```
// Step 1: draw the rectangular skeleton
```

foreach *bounding rectangle* $(x_{\min}, x_{\max}, y_{\min}, y_{\max})$ **do**
  draw the outer red rectangle $(x_{\min} - 1, x_{\max} + 1, y_{\min} - 1, y_{\max} + 1)$;
  if $x_{\min} + 1 < x_{\max} - 1$ *and* $y_{\min} + 1 < y_{\max} - 1$ **then**
    draw the inner red rectangle $(x_{\min} + 1, x_{\max} - 1, y_{\min} + 1, y_{\max} - 1)$;
  end
  draw the middle black rectangle $(x_{\min}, x_{\max}, y_{\min}, y_{\max})$;
end

```
// Step 2: decorate all special points
```

foreach *corner point* p **do**
  apply the corner decoration rule of Algorithm B-3;
end
foreach $p \in$ CrossingSet **do**
  apply the crossing decoration rule of Algorithm B-3;
end
foreach $p \in$ NodeSet **do**
  apply the node decoration rule of Algorithm B-3;
end

```
// Step 3: add axis-centered auxiliary marks
```

foreach $t \in \mathcal{Y}_n$ **do**
  draw a short vertical black segment from $(0, t-1)$ to $(0, t+1)$;
  draw a short horizontal black segment from $(t-1, 0)$ to $(t+1, 0)$;
  draw larger blue dots at $(0, t)$ and $(t, 0)$;
  draw smaller blue dots at $(0, t \pm 1)$ and $(t \pm 1, 0)$;
end
if *an output path is specified* **then**
  save the rendered figure in PDF format;
end

```
            for i in range(self.m):
                # Generate edge: change the i-th bit of surface to *
                edge_bits = 0
                for pos in range(self.m):
                    if pos != i:
                        edge_bits = (edge_bits << 1) | surface[pos]
                row.append(self.edge_index(i, edge_bits))
            d2.append(row)
        return d2

    def generate_geodesics(self):
        """Generate all geodesics, each geodesic consists of four edges"""
        cycles = []
        m = self.m
        for i in range(m):
            left = (i - 1) % m
            right = (i + 1) % m
            free_pos = [pos for pos in range(m) if pos not in {i, left, right}]
            num_free = len(free_pos)
            for bits in range(1 << num_free):
                # Set bits for free positions
                base = {}
                for idx, pos in enumerate(free_pos):
                    base[pos] = (bits >> (num_free - 1 - idx)) & 1
                # Generate four edges, corresponding to four combinations of left and right positions
                cycle = []
                for lv, rv in itertools.product([0, 1], repeat=2):
                    edge_bits = 0
                    for pos in range(m):
                        if pos == i:
                            continue  # Position of *
```

```
                    if pos == left:
                        bit = lv
                    elif pos == right:
                        bit = rv
                    else:
                        bit = base[pos]
                    edge_bits = (edge_bits << 1) | bit
                edge_idx = self.edge_index(i, edge_bits)
                cycle.append(edge_idx)
            cycles.append(cycle)
        return cycles

    def sparse_gf2_rank(self, matrix):
        """Compute rank of sparse matrix over GF(2)"""
        rows = [set(row) for row in matrix]
        pivot_cols = {}
        rank = 0

        for r in range(len(rows)):
            row = rows[r].copy()
            # Find pivot column
            while row:
                pivot = min(row)
                if pivot in pivot_cols:
                    row ^= pivot_cols[pivot]
                else:
                    pivot_cols[pivot] = row
                    rank += 1
                    break
        return rank

    def curve_homology_rank(self, cycles):
        """Compute homology rank of cycle list in H1"""
        # Convert d2 to set form
        d2_rows = [set(row) for row in self.d2]
        B_rank = self.sparse_gf2_rank(d2_rows)

        # Convert cycles to set form
```

```
        S_rows = [set(cycle) for cycle in cycles]
        S_rank = self.sparse_gf2_rank(S_rows)

        # Compute rank of S + B
        combined = S_rows + d2_rows
        S_plus_B_rank = self.sparse_gf2_rank(combined)

        # Compute dimension of intersection
        intersection_dim = S_rank + B_rank - S_plus_B_rank

        # Return homology rank
        return S_rank - intersection_dim

if __name__ == "__main__":
    for m in range(3,22):
        print(f"\nAnalyzing for m={m}")
        g=1+(m-4)*2**(m-3)
        print(f"Genus: {g}")
        print(f"Homology H1: {2*g}")
        analyzer = GeodesicAnalyzer(m)
        geodesics = analyzer.generate_geodesics()
        print(f"Generated geodesic cycles: {len(geodesics)}")
        rank = analyzer.curve_homology_rank(geodesics)
        print(f"Homology rank of geodesics: {rank}")
```

B.3 Homological redundancy calculation in the original maps of hypercube graph embeddings in even dimension

```
import numpy as np
from itertools import product
from scipy.sparse import lil_matrix, csc_matrix, hstack,
   save_npz, load_npz
from multiprocessing import Pool, cpu_count
import os
import tempfile

def generate_edges(n):
    """Optimized edge generator, memory efficient"""
```

```
    pattern = [0, 1]
    for i in range(n):
        for bits in product(pattern, repeat=n-1):
            yield tuple(bits[:i] + ('*',) + bits[i:])

def generate_faces(n):
    """Optimized face generator, generates in batches"""
    for i in range(n):
        j = (i + 1) % n
        for bits in product([0, 1], repeat=n-2):
            base = []
            bit_iter = iter(bits)
            for pos in range(n):
                if pos == i or pos == j:
                    base.append(None)
                else:
                    base.append(next(bit_iter))

            edge1 = base.copy(); edge1[i] = '*'; edge1[j] = 0
            edge2 = base.copy(); edge2[i] = 0;   edge2[j] = '*'
            edge3 = base.copy(); edge3[i] = '*'; edge3[j] = 1
            edge4 = base.copy(); edge4[i] = 1;   edge4[j] = '*'

            yield [tuple(edge1), tuple(edge2), tuple(edge3),
               tuple(edge4)]

def generate_circles(n):
    """Optimized circle generator, generates in batches"""
    k = n // 2
    for i in range(k):
        j = (i + k) % n
        for bits in product([0, 1], repeat=n-2):
            base = []
            bit_iter = iter(bits)
            for pos in range(n):
                if pos == i or pos == j:
                    base.append(None)
                else:
```

```
                    base.append(next(bit_iter))

            edge1 = base.copy(); edge1[i] = '*'; edge1[j] = 0
            edge2 = base.copy(); edge2[i] = 0;   edge2[j] = '*'
            edge3 = base.copy(); edge3[i] = '*'; edge3[j] = 1
            edge4 = base.copy(); edge4[i] = 1;   edge4[j] = '*'

            yield [tuple(edge1), tuple(edge2), tuple(edge3),
               tuple(edge4)]

def gf2_sparse_rank(matrix):
    """Optimized rank calculation function, without
       parallelization"""
    rows, cols = matrix.shape
    sparse_rows = []

    # Convert to row set representation
    for i in range(rows):
        row = matrix.getrow(i).toarray().flatten()
        sparse_rows.append({j for j in range(cols) if row[j]})

    pivot_cols = {}  # Store pivot columns
    rank = 0

    # Main elimination process
    for r in range(len(sparse_rows)):
        row = sparse_rows[r].copy()
        while row:
            pivot = min(row)
            if pivot in pivot_cols:
                row ^= pivot_cols[pivot]
            else:
                pivot_cols[pivot] = row
                rank += 1
                break
    return rank

def compute_homology(k_values):
```

```
194     print("k\tn\trank(B)\tH1\trank(S)\tB∩S dim")
195     print("-----------------------------------")
196
197     for k in k_values:
198         n = 2 * k
199
200         # 1. Generate edges and create index mapping
201         edge_index = {}
202         for idx, edge in enumerate(generate_edges(n)):
203             edge_index[edge] = idx
204         num_edges = len(edge_index)
205
206         # 2. Pre-calculate matrix sizes using theoretical
               values
207         num_faces = n * 2**(n-2)
208         num_circles = k * 2**(n-2)
209
210         # 3. Use temporary directory to store sparse matrices
211         with tempfile.TemporaryDirectory() as temp_dir:
212             B_path = os.path.join(temp_dir, 'B_matrix.npz')
213             S_path = os.path.join(temp_dir, 'S_matrix.npz')
214
215             # 4. Construct B matrix and save
216             B_matrix = lil_matrix((num_edges, num_faces), dtype
                   =np.int8)
217             for j, face in enumerate(generate_faces(n)):
218                 for edge in face:
219                     if edge in edge_index:
220                         B_matrix[edge_index[edge], j] = 1
221             B_matrix = B_matrix.tocsc()
222             save_npz(B_path, B_matrix)
223
224             # 5. Construct S matrix and save
225             S_matrix = lil_matrix((num_edges, num_circles),
                   dtype=np.int8)
226             for j, circle in enumerate(generate_circles(n)):
227                 for edge in circle:
228                     if edge in edge_index:
```

```
                        S_matrix[edge_index[edge], j] = 1
            S_matrix = S_matrix.tocsc()
            save_npz(S_path, S_matrix)

            # 6. Load matrices from file
            B_matrix = load_npz(B_path)
            S_matrix = load_npz(S_path)

            # 7. Calculate ranks using theoretical values
            rank_B = n * 2**(n-2) - 1
            rank_S = k * 2**(n-2)

            # 8. Calculate rank of combined matrix (no batching)
            combined = hstack([B_matrix, S_matrix], format='csc')
            rank_combined = gf2_sparse_rank(combined)

            # 9. Calculate intersection dimension (ensure non-negative)
            intersection_dim = max(0, rank_B + rank_S - rank_combined)

            # Theoretical value
            H1 = 2 * (1 + (n - 4) * 2**(n-3))

            print(f"{k}\t{n}\t{rank_B}\t{H1}\t{rank_S}\t{intersection_dim}")

if __name__ == '__main__':
    # Test from k=2 to k=8
    compute_homology(range(1, 8))
```

REFERENCES

[1] AKROUT H. Singularités topologiques des systoles généralisées[J]. Topology, 2003, 42(2): 291-308.

[2] AN N, IHRINGER F, IRMER I. Small genus, small index critical points of the systole function[EB/OL]. 2025. https://arxiv.org/abs/2504.17316. arXiv: 2504.17316 [math.GT].

[3] APPEL K, HAKEN W. Every planar map is four colorable. Part I: Discharging[J]. Illinois Journal of Mathematics, 1977.

[4] APPEL K, HAKEN W, KOCH J. Every planar map is four colorable. Part II: Reducibility[J]. Illinois Journal of Mathematics, 1977.

[5] ASHCROFT N W, MERMIN N D. Solid State Physics[M]. Holt, Rinehart, 1976.

[6] ATARIHUANA Y, GARCÍA J, HIDALGO R A, et al. Dessins d'enfants and some holomorphic structures on the Loch Ness Monster[J]. The Quarterly Journal of Mathematics, 2022, 73(1): 349-369.

[7] BAHRI A, BENDERSKY M, COHEN F R. Polyhedral products and features of their homotopy theory[J]. Handbook of homotopy theory, 2020: 103-144.

[8] BAHRI A, BENDERSKY M, COHEN F R, et al. Decompositions of the polyhedral product functor with applications to moment-angle complexes and related spaces[J]. Proceedings of the National Academy of Sciences, 2009, 106(30): 12241-12244.

[9] BAHRI A, BENDERSKY M, COHEN F R, et al. The polyhedral product functor: a method of decomposition for moment-angle complexes, arrangements and related spaces[J]. Advances in Mathematics, 2010, 225(3): 1634-1668.

[10] BASKAKOV I V. Cohomology of K-powers of spaces and the combinatorics of simplicial divisions[J]. Russian Mathematical Surveys, 2002, 57(5): 989-990.

[11] BEINEKE L W, HARARY F. The genus of the n-cube[J/OL]. Canadian J. Math., 1965, 17: 494-496. https://doi.org/10.4153/CJM-1965-048-6. DOI: 10.4153/CJM-1965-048-6.

[12] BENDER C M, BOETTCHER S. Real Spectra in Non-Hermitian Hamiltonians Having PT Symmetry[J]. Physical Review Letters, 1998, 80(24): 5243-5246. DOI: 10.1103/PhysRevLett.80.5243.

[13] BERGHOLTZ E J, BUDICH J C, KUNST F K. Exceptional Topology of Non-Hermitian Systems[J]. Reviews of Modern Physics, 2021, 93: 015005. DOI: 10.1103/RevModPhys.93.015005.

[14] BIGGS N. Automorphisms of imbedded graphs[J]. Journal of Combinatorial Theory, Series B, 1971, 11(2): 132-138.

[15] BLOCH F. Über die Quantenmechanik der Elektronen in Kristallgittern[J]. Zeitschrift für Physik, 1929, 52: 555-600. DOI: 10.1007/BF01339455.

[16] BOSIO F, MEERSSEMAN L. Real quadrics in C n, complex manifolds and convex polytopes[J]. Acta Math, 2006.

[17] BUCHSTABER V M, PANOV T E. Torus actions, combinatorial topology, and homological algebra[J]. Russian Mathematical Surveys, 2000, 55(5): 825-921.

[18] BUSER P. Geometry and spectra of compact Riemann surfaces[M]. Springer Science & Business Media, 2010.

[19] CATALANO D A, CONDER M D, DU S F, et al. Classification of regular embeddings of n-dimensional cubes[J]. Journal of Algebraic Combinatorics, 2011, 33(2): 215-238.

[20] CATALANO D A, NEDELA R. A characterization of regular embeddings of n-dimensional cubes[J]. Discrete mathematics, 2010, 310(17-18): 2364-2371.

[21] COXETER H S M. Regular polytopes[M]. Courier Corporation, 1973.

[22] COXETER H. Regular skew polyhedra in three and four dimension, and their topological analogues[J]. Proceedings of the London Mathematical Society, 1938, 2(1): 33-62.

[23] DAS S. Genus of the hypercube graph and real moment-angle complexes[J/OL]. Topology Appl., 2019, 258: 415-424. https://doi.org/10.1016/j.topol.2019.03.009. DOI: 10.1016/j.topol.2019.03.009.

[24] De MEDRANO S L, VERJOVSKY A. A new family of complex, compact, non-symplectic manifolds[J]. Boletim da Sociedade Brasileira de Matemática-Bulletin/Brazilian Mathematical Society, 1997, 28(2): 253-269.

[25] DENHAM G, SUCIU A I. Moment-angle complexes, monomial ideals and Massey products[J]. Pure and Applied Mathematics Quarterly, 2007, 3(1): 25-60.

[26] DU S F, KWAK J H, NEDELA R. Classification of regular embeddings of hypercubes of odd dimension[J]. Discrete mathematics, 2007, 307(1): 119-124.

[27] FENCHEL W. Elementary geometry in hyperbolic space[M]. Walter de Gruyter, 1989.

[28] FRANZ M. Koszul duality and equivariant cohomology for tori[J]. International Mathematics Research Notices, 2003, 2003(42): 2255-2303.

[29] FRANZ M. Koszul duality and equivariant cohomology[J]. Documenta Mathematica, 2006, 11: 243-259.

[30] FRANZ M. The integral cohomology of toric manifolds[J]. Proceedings of the Steklov Institute of Mathematics, 2006, 252(1): 53-62.

[31] GIRONDO E, GONZÁLEZ-DIEZ G. Introduction to compact Riemann surfaces and dessins d'enfants[M]. Cambridge University Press, 2012.

[32] GRIFFITHS D J, SCHROETER D F. Introduction to Quantum Mechanics[M]. 3rd ed. Cambridge University Press, 2018.

[33] GROSS J L, TUCKER T W. Topological Graph Theory[M]. Wiley-Interscience, 1987.

[34] GUILLOT P. An elementary approach to dessins d'enfants and the Grothendieck–Teichmüller group[J]. L'enseignement Mathématique, 2015, 60(3): 293-375.

[35] HEAWOOD P J. Map-colour theorem[J/OL]. Proc. London Math. Soc. (2), 1949, 51: 161-175. https://doi.org/10.1112/plms/s2-51.3.161. DOI: 10.1112/plms/s2-51.3.161.

[36] HEISS W D. The Physics of Exceptional Points[J]. Journal of Physics A: Mathematical and Theoretical, 2012, 45(44): 444016. DOI: 10.1088/1751-8113/45/44/444016.

[37] HOCHSTER M. Cohen-Macaulay rings, combinatorics, and simplicial complexes, in" Ring Theory II"[J]. Lect. Notes in Pure Appl. Math., 1977(26): 171-223.

[38] IMAYOSHI Y, TANIGUCHI M. An introduction to Teichmüller spaces[M]. Springer Science & Business Media, 2012.

[39] IVERSEN B. Hyperbolic geometry[M]. Cambridge University Press, 1992.

[40] JAMES I M. Reduced product spaces[J]. Annals of Mathematics, 1955, 62(1): 170-197.

[41] JAMES L D, JONES G A. Regular orientable imbeddings of complete graphs[J]. Journal of Combinatorial Theory, Series B, 1985, 39(3): 353-367.

[42] JONES G, SINGERMAN D. Belyi Functions, Hypermaps and Galois Groups.[J]. Bulletin of the London Mathematical Society, 1996, 28(6).

[43] JONES G A. Maps on surfaces and Galois groups[J]. Mathematica Slovaca, 1997, 47(1): 1-33.

[44] JONES G A. Bipartite graph embeddings, Riemann surfaces and Galois groups[J]. Discrete Mathematics, 2015, 338(10): 1801-1813.

[45] JONES G A, SINGERMAN D. Theory of maps on orientable surfaces[J]. Proceedings of the London Mathematical Society, 1978, 3(2): 273-307.

[46] JONES G A, WOLFART J. Dessins d'enfants on Riemann surfaces[M]. Springer, 2016.

[47] KEMPE A B. On the Geographical Problem of the Four Colours[J/OL]. Amer. J. Math., 1879, 2(3): 193-200. https://doi.org/10.2307/2369235. DOI: 10.2307/2369235.

[48] KEPLER J. Mysterium cosmographicum (1596)[J]. English translation: The secret of the universe, transl. AM Duncan, Abaris, New York, 1981.

[49] KITTEL C. Introduction to Solid State Physics[M]. 8th ed. Wiley, 2004.

[50] KLINGENBERG W. Lectures on closed geodesics[M]. Springer Science & Business Media, 1978.

[51] KURATOWSKI K. Sur le problème des courbes gauches en Topologie[J]. Fundamenta Mathematicae, 1930.

[52] KWON Y S. New regular embeddings of n-cubes Qn[J]. Journal of Graph Theory, 2004, 46(4): 297-312.

[53] KWON Y S, NEDELA R. Non-existence of nonorientable regular embeddings of n-dimensional cubes[J]. Discrete mathematics, 2007, 307(3-5): 511-516.

[54] MILNOR J. The construction FK[M]. Princeton, 1956.

[55] MIRZAKHANI M. Growth of the number of simple closed geodesies on hyperbolic surfaces[J]. Annals of Mathematics, 2008, 168(1): 97-125.

[56] MOHAR B, THOMASSEN C. Graphs on Surfaces[M]. Johns Hopkins University Press, 2001.

[57] MOISEYEV N. Non-Hermitian Quantum Mechanics[M]. Cambridge University Press, 2011. DOI: 10.1017/CBO9780511976186.

[58] MOSTAFAZADEH A. Is Pseudo-Hermitian Quantum Mechanics an Indefinite-Metric Quantum Theory?[J]. Czechoslovak Journal of Physics, 2003, 53(11): 1079-1084. DOI: 10.1023/B:CJOP.0000010537.23790.8C.

[59] MOSTAFAZADEH A. Pseudo-Hermitian Representation of Quantum Mechanics[J]. International Journal of Geometric Methods in Modern Physics, 2010, 7(7): 1191-1306.

[60] NEDELA R, ŠKOVIERA M. Which generalized Petersen graphs are Cayley graphs?[J]. Journal of Graph Theory, 1995, 19(1): 1-11.

[61] NEDELA R, ŠKOVIERA M. Regular maps from voltage assignments and exponent groups[J]. European Journal of Combinatorics, 1997, 18(7): 807-823.

[62] PANOV T E. Cohomology of face rings, and torus actions[J]. London Mathematical Society Lecture Note Series, 2008, 347: 165.

[63] PORTER G J. The homotopy groups of wedges of suspensions[J]. American Journal of Mathematics, 1966, 88(3): 655-663.

[64] PORTER G J. Higher products[J]. Transactions of the American Mathematical Society, 1970, 148(2): 315-345.

[65] AL-RAISI A. Equivariance, module structure, branched covers, strickland maps and cohomology related to the polyhedral product functor[M]. University of Rochester, 2014.

[66] RATCLIFFE J G. Foundations of hyperbolic manifolds[M]. Springer, 2006.

[67] RINGEL G. Über drei kombinatorische Probleme am n-dimensionalen Würfel und Würfelgitter[J/OL]. Abh. Math. Sem. Univ. Hamburg, 1955, 20: 10-19. https://doi.org/10.1007/BF02960735. DOI: 10.1007/BF02960735.

[68] RINGEL G. Map Color Theorem[M]. Springer, 1974.

[69] ROBERTSON N, SANDERS D P, SEYMOUR P D, et al. The Four Colour Theorem[J]. Journal of Combinatorial Theory, Series B, 1997.

[70] ROBERTSON N, SEYMOUR P D. Graph minors. I. Excluding a forest[J]. Journal of Combinatorial Theory, Series B, 1983.

[71] SAKURAI J J, NAPOLITANO J. Modern Quantum Mechanics[M]. 2nd ed. Cambridge University Press, 2017.

[72] SCHALLER P S. Systoles and topological Morse functions for Riemann surfaces[J]. Journal of Differential Geometry, 1999, 52(3): 407-452.

[73] SIRÁN J. How symmetric can maps on surfaces be?[J]. Surveys in Combinatorics 2013, 2013, 409.

[74] THURSTON W P. The geometry and topology of three-manifolds: With a preface by Steven P. Kerckhoff[M]. American Mathematical Society, 2022.

[75] WILSON S. Families of regular graphs in regular maps[J]. Journal of Combinatorial Theory, Series B, 2002, 85(2): 269-289.

[76] XU J. A classification of regular embeddings of hypercubes Q_{2m} with m odd[J]. Science in China Series A: Mathematics, 2007, 50(12): 1673-1679.

[77] YAO S, WANG Z. Edge States and Topological Invariants of Non-Hermitian Systems[J]. Physical Review Letters, 2018, 121(8): 086803. DOI: 10.1103/PhysRevLett.121.086803.

ACKNOWLEDGEMENTS

The results presented in Chapter 5 of this thesis were obtained in collaboration with Dr. Zhiwang Yu, a senior colleague in our research group.

I wish to express my sincere gratitude to my supervisor, Professor Yifei Zhu, for his meticulous guidance. Not only have I gained substantial knowledge under his supervision, but I have also greatly benefited from his approach to work and his way of thinking. His mentorship and exemplary conduct will benefit me throughout my life.

I am also thankful to my fellow group members for their warm help and support. They have offered me invaluable assistance whenever I encountered difficulties, and I have greatly benefited from our discussions.

Finally, I would like to thank my family for their unwavering support and encouragement throughout my academic journey. Without their support, I could not have completed this thesis.